University of
Stavanger

Faculty of Science and Technology

MASTER'S THESIS

Study program/Specialization: Petroleum Geosciences Engineering	Spring, 2019 Open
Writer: Vlad Mihai Rotar	(Writer's signature)

Faculty supervisor:
Nestor Cardozo, University of Stavanger

External supervisor(s):
Surender Manral, Schlumberger SIS
Lothar Schulte, Schlumberger SIS

Title of thesis:
Reservoir Modeling and Uncertainty Estimation: A Comparison Between Stochastic and Deterministic Inversion.

Credits (ECTS): 30

Keywords: Stochastic Inversion Deterministic Inversion 3D Facies Modeling Uncertainty Analysis Oseberg South	Pages: 104 Stavanger, 29th June 2019

Reservoir Modeling and Uncertainty Estimation: A Comparison Between Stochastic and Deterministic Inversion.

by

Vlad Mihai Rotar

MSc Thesis

Presented to the Faculty of Science and Technology
The University of Stavanger

The University of Stavanger
June 2019

Acknowledgements

This Master thesis is submitted in completion of the MSc in Petroleum Geoscience Engineering at the University of Stavanger.

I would like to thank my supervisors Lothar Schulte, Nestor Cardozo and Surender Manral for the continuous support and guidance throughout this thesis.

I would like to thank Equinor ASA and the Oseberg Sør license for providing the dataset and to Schlumberger for providing the software Petrel.

Finally, I would like to thank my family for their support and encouragement during this Master program.

Disclaimer

The views expressed in this paper are the views of the authors and do not necessarily reflect the views of Equinor and the Oseberg Sør license.

Reservoir Modeling and Uncertainty Estimation: A Comparison Between Stochastic and Deterministic Inversion.

Vlad Mihai Rotar

The University of Stavanger, 2019

Supervisors: Nestor Cardozo, Surender Manral, and Lothar Schulte

Abstract

This study compares the uncertainty estimation based on both deterministic and stochastic inversion with the Gauss Simulation technique applied to modelling the distribution of limestone facies in a sand-shale reservoir. The final goal is to understand and quantify the benefit of using stochastic inversion in facies modeling and uncertainty estimation. The study area is the Oseberg South Field which is a producing oil field in the northern North Sea. This study focusses on the reservoir level in the Middle Jurassic Brent Group.

Because of the missing high frequencies deterministic inversion provides a smooth average of the impedance which cannot reliably model the thin layers of limestone in the reservoir. Facies modeling based on deterministic inversion is superior to well-based stochastic modeling only in the case of thick layers that lie within seismic resolution.

Stochastic inversion adds value by capturing the property distribution uncertainty which is show-cased by the facies modelling. Stochastic inversion is superior to deterministic inversion because possible limestone layers of thickness below seismic resolution are addressed. Furthermore, stochastic inversion provides multiple equiprobable results thus allowing for a more reliable uncertainty estimation of the reservoir facies.

Because there are no published studies in the Oseberg South field, incorporating seismic inversion within the geomodelling workflow the results of this thesis could lead to a better decision making for future well placement.

Table of Contents

List of tables

List of Figures

1 Introduction

Stochastic models are valuable tools for characterizing hydrocarbon reservoirs. Information about the distribution of properties such as facies, porosity and permeability within the reservoir is essential in order to reduce the uncertainty associated with both exploration and production phases thus leading to a better decision-making (Sabeti, 2017).

The incorporation of deterministic inversion in the geomodelling workflow has become a standard procedure because it allows potentially to lower the uncertainty of the reservoir property distribution that correlate with the acoustic impedance (facies, porosity etc.) away from the well locations and thus provide more reliable models compared to simple stochastic or deterministic modelling. The uncertainty of the property distribution can be captured through geostatistical means.

Stochastic inversion delivers multiple alternative impedance cubes of higher resolution compared to deterministic inversion while honoring the seismic data. Consequently, it offers an alternative approach to capture the uncertainty in the property distribution because it allows addressing the impact of the limitation in seismic resolution on the modelled reservoir property. This study compares the uncertainty estimation based on stochastic inversion with the Gauss simulation technique applied to facies modelling. Its final goal is to showcase the superiority of facies modelling based on stochastic inversion in handling thin facies zones beyond seismic resolution.

1.1 Objectives and motivation

The objective of this Master thesis is to compare uncertainty estimation based on both deterministic and stochastic inversion with the Gauss Simulation technique applied to modelling of the distribution of limestone facies in a sand-shale reservoir. The final goal is to understand and quantify the benefit of using stochastic inversion in facies modeling and uncertainty estimation.

1.2 Study Area

The study area is the Oseberg South Field which is a producing oil field on the eastern flank of the Viking Graben in the northern North Sea (**Figure 1.1**). This study will focus on the reservoir level represented by the Middle Jurassic Brent Group. The most prolific reservoir interval is represented by the Ness Formation which consists coals, shales, siltstones and very fine to medium grained sandstones (Løseth et al., 2009, NPD, 2018a). There is also significant hydrocarbon accumulation in the overlying deposits of the Heather Formation.

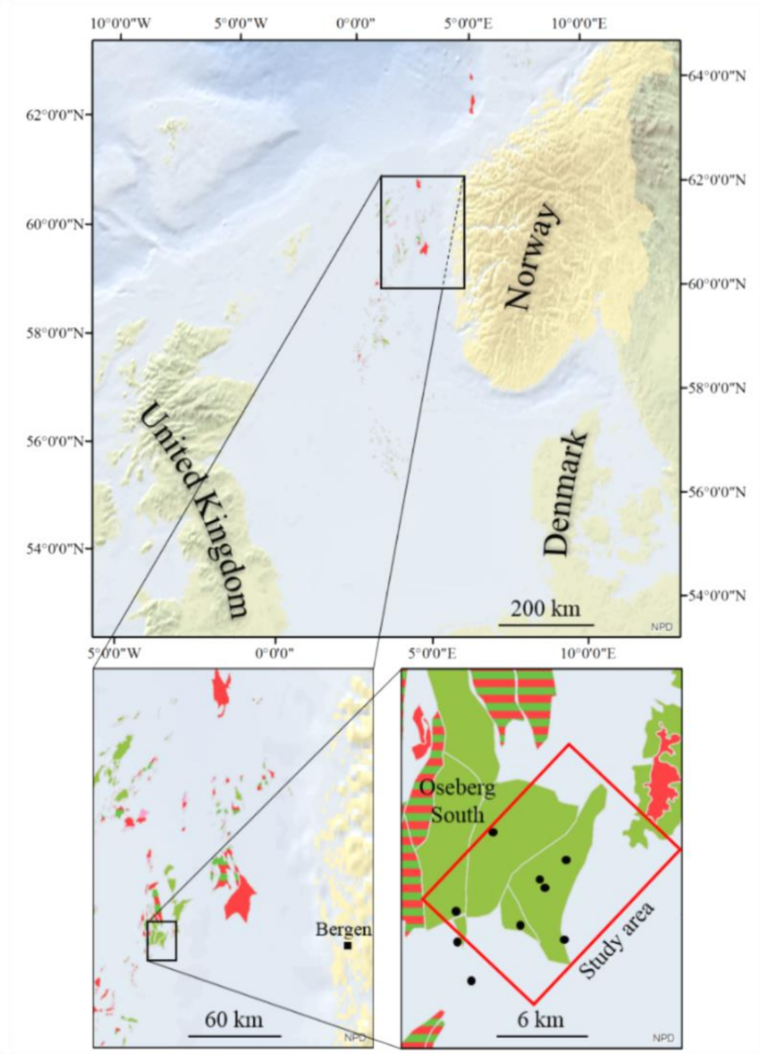

Figure 1.1: Location of the Oseberg South Field, study area (red square), available wells (black dots), and nearby fields (oil fields are in green and gas fields in red) (Frette., 2018 modified after NPD, 2018b)

1.3 Previous Work

Currently, there are no published studies covering the Oseberg South field which incorporate seismic inversion within the geomodelling workflow. However, similar studies have been conducted for other fields. Robinson (2001) compared the recursive inversion with stochastic inversion and performed porosity modeling based on both methods (**Figure 1.2**). The study concluded that stochastic inversion increased the vertical resolution suitable for reservoir characterization.

Francis (2006a, 2006b) compared the use of deterministic inversion with stochastic inversion for 3D facies modeling of the Straton Field a gas field in the NW Gulf Coast Basin, Gulf of Mexico (**Figure 1.3).** He concluded that stochastic inversion is more reliable than deterministic inversion when modeling thin layered beds.

Moyen and Doyen (2009) showcased the use of stochastic inversion for uncertainty estimation. They also developed a workflow for analyzing reservoir connectivity to asses uncertainty for existing or planned wells (**Figure 1.4**).

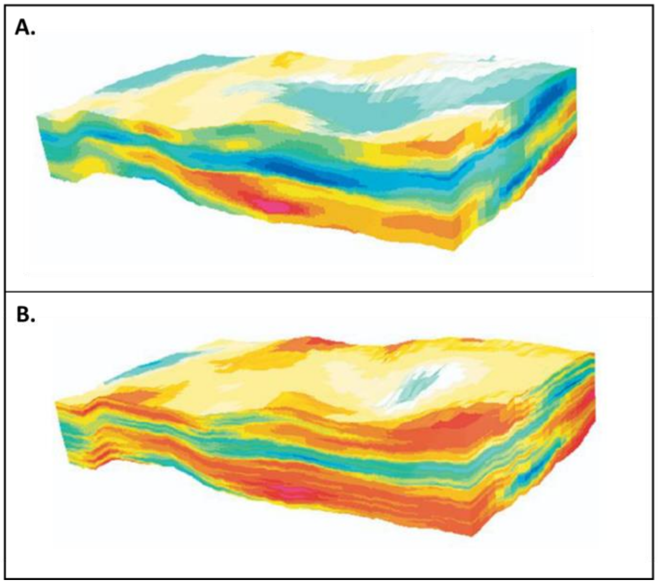

Figure 1.2 A) Recursive inversion result. B) Stochastic inversion result Note the increase in vertical resolution provided by stochastic inversion in comparison to the recursive inversion.

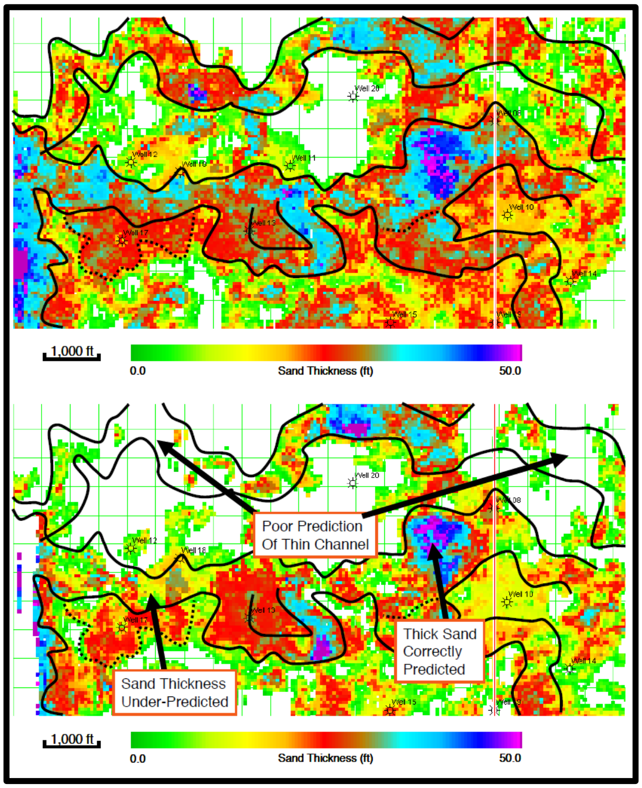

Figure 1.3: Upper display shows sand thickness map for a P50 sand probability from 100 stochastic seismic inversion realizations. Note thin channel running east-west across northern area of map. Lower display shows sand thickness for same interval estimated using deterministic inversion. Note overall less sand with poor prediction of thin channel.

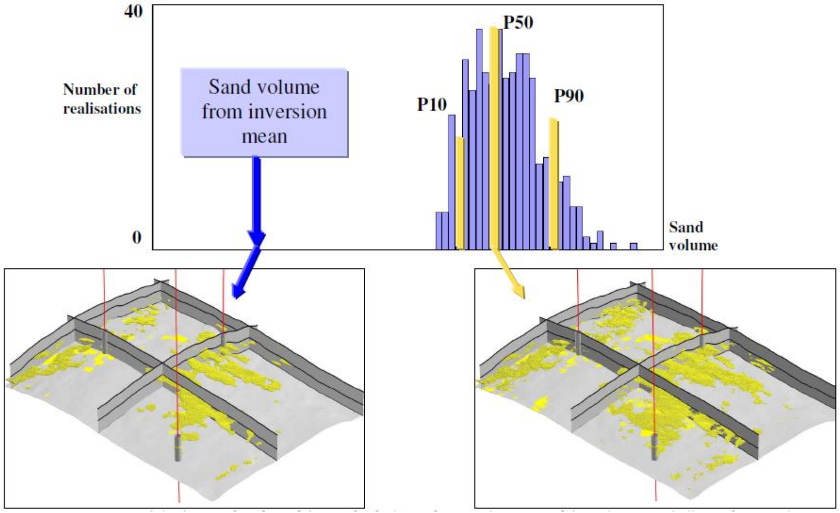

Figure 1.4: Comparison of the facies cubes derived from individual impedance realizations and from the mean of all impedance realizations(considered as an analogue to a deterministic inversion). Top: histogram of the total sand volume constructed from 500 facies realizations. Bottom: facies cube derived from the mean of all impedance realizations (left) and from one impedance realization (right). Sand volume from deterministic inversion is significantly smaller than from any realization and the geometry of the sand bodies is very different.

2 Geology of the area

This chapter summarizes the geology of the study area. Section 2.1 gives a brief description of the main tectonic events in the study area while Section 2.2 briefly describes the reservoir interval.

2.1 Structural evolution

The Oseberg-Brage area is located on the eastern flank of the Viking Graben (**Figure 2.1** and Figure 2.2). The structural framework of the Oseberg-Brage area developed during two main extensional episodes: Permian-Triassic and Middle Jurassic-Early Cretaceous (Eynon, 1981; Badley et al., 1984 ,1988; Giltner 1987; Gabrielsen et al. 1990; Stewart et al. 1992; Yielding et al 1992, Steel 1993; Færseth, 1996; Ravnås and Bondevik, 1997; Færseth and Ravnås, 1998) . These rifting events resulted into N-S and NE-SW trending normal faults creating eastern oriented half-graben structures (**Figure 2.2a**).

The Permo-Triassic extension phase affected the whole northern North Sea. Rifting occurring from the Eastern Shetland Platform in the west to the eastern edge represented by the Øygarden Fault Complex (Færseth, 1996). According to Vialli (1988) and Færseth et al. (1995a), the highest fault activity associated to the Permo-Triassic extension occurred in the eastern part of the North Sea basin, bellow the western part of the Horda Platform creating full graben features flanked by tilted half grabens. The Brage East Fault separates the full-graben structure in the east from the western Jurassic half-graben (Færseth, 1996) (**Figure 2.2b**).

The Middle Triassic to Middle Jurassic post-rift sequence represents a regional subsidence phase caused by thermal cooling (Badley et al. 1988, Steel and Ryseth, 1990). In turn the post rift subsidence caused the rotation of the basin towards the rift axis. The Statfjord Formation and the Dunlin Gp present a westward thickening, varying from 40m along the eastern edge to more than 500m close to the graben axis indicating syn-depositional differential subsidence during the Early Jurassic (Steel and Ryseth, 1990).

The thermal and fault-related subsidence continued in the Middle Jurassic documented by the increase in thickness of the Brent Gp. (Steel and Ryseth, 1990, Færseth and Ravnås, 1998). The thickness is also controlled by the incipient faulting marking the transition to the main-rift phase (Færseth and Ravnås, 1998).

As opposed to the Permo-Triassic rifting phase which occurred widely, the Upper -Jurassic extension was more localized mainly concentrated along the axis of the Viking and Sogn Grabens (Færseth, 1996) (**Figure 2.1)**. Most of the faults formed during the Permo-Triassic rifting were reactivated during the Jurassic extension. The early rifting is marked by the deposition of Heather Formation (Færseth and Ravnås, 1998).

The footwall of the Permo-Triassic Barge East Fault is transected by the opposite dipping Brage Fault forming the Brage Horst which separates the Permo-Triassic full graben in the east from the Jurassic half grabens (Færseth, 1996). The increasing activity of the Brage Fault lead to the decoupling of the Oseberg Fault Block from the Horda Platform (Færseth and Ravnås, 1998). The eastward thickening of the Draupne Formation during the Callovian and the Late Oxfordian-earliest Kimmeridgian marks the maximum footwall uplift at ca 60°30´N (Færseth and Ravnås, 1998) (**Figure 2.1**).

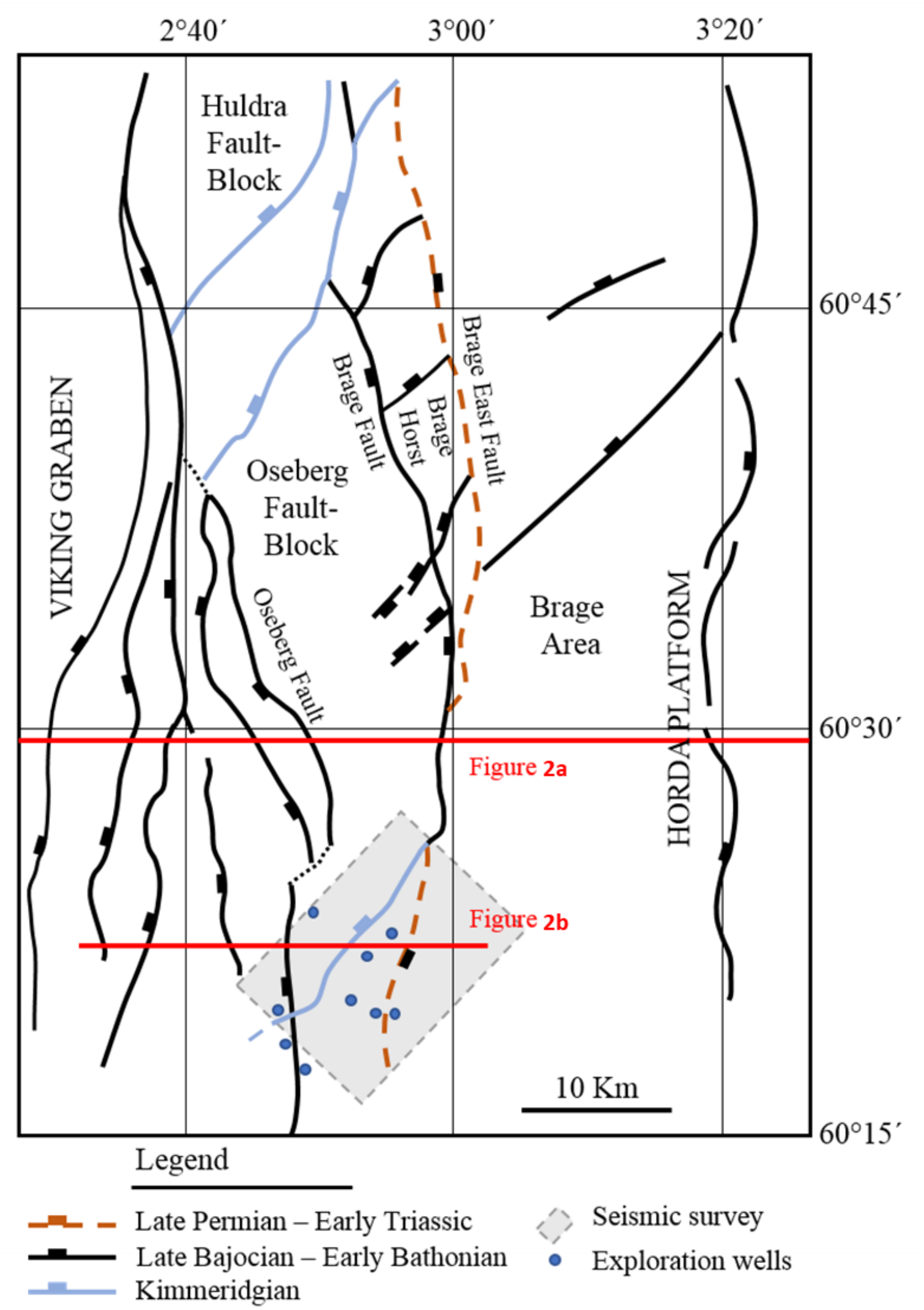

Figure 2.1: Structural map of the Oseberg-Brage area indicating the timing of fault initiation of the major normal faults (Færseth and Ravnås, 1998). Available exploration wells, seismic coverage area, and the location of the cross-sections in Figure 2.2 are highlighted in the map. Frette, (2018) modified after Ravnås and Bondevik, (1997); Færseth and Ravnås, (1998).

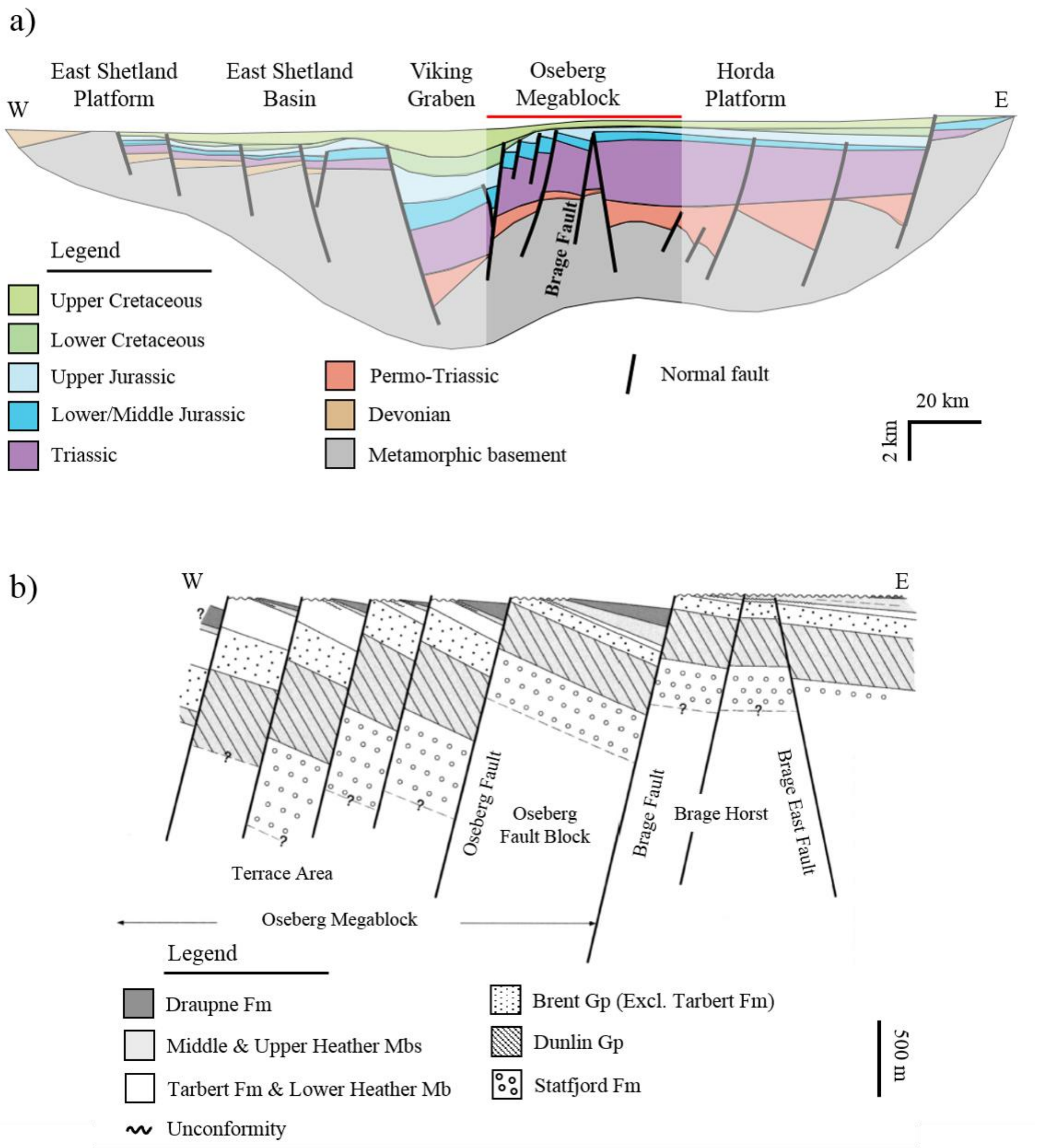

Figure 2.2: a) Cross-section showing Jurassic and Permo-Triassic major fault-blocks with related faults across the central segment of the northern North Sea at the end of the Cretaceous time (Færseth, 1996). The red line (and the bright area beneath) represents the area within the structural map in Figure 2.1. b) Schematic cross-section showing the strata deposited during the Jurassic (Færseth and Ravnås, 1998). Frette, (2018) modified after Færseth, (1996) and Færseth and Ravnås, (1998), respectively. See Figure 2.1 for location of the cross-sections.

2.2 Reservoir interval

The main reservoir interval within the Oseberg South field is represented by the Brent Group which is a prolific hydrocarbon reservoir in both British and Norwegian sectors of the northern North Sea. Lithostratigraphically The Brent Group is divided in five units: Oseberg, Rannoch, Etive, Ness and Tarbert (**Figure 2.3**) (Graue et al. 1987; Johnsen et al., 1995).

The Oseberg Formation was deposited during the late Toarcian to Aalenian lowstand caused by the uplift on the Horda Platform (Hansen et al. 1992; Ravnås et al. 1997). It consists of moderate to poorly sorted, coarse grained sandstone deposited in a series of discrete lobes triggered by the tectonic movements (Johnsen et al., 1995).

Rannoch and Etive Formations deposited as a result of the late Aalenian to early Bajocian transgression which lead to the progradation of Brent delta. The Rannoch Formation consists of mudrocks which grade up into fine sandstones deposited in a lower to middle shoreface or lower delta front environment. The Etive Formation consists of coarse grained, poorly sorted sandstones which represent upper shoreface/foreshore deposits (Johnsen et al., 1995).

The Ness Formation is the most lithologically variable unit of the Brent Group with varying thickness from 20 to more than 100m (Richards, 1992). The Ness Formation can be divided into a Lower, Middle and Upper section (Johnsen et al., 1995). The Lower Ness Unit consist of lagoonal siltstone, lagoonal shoal, beach and washover sandstones and coal seams. The Middle Unit is composed of siltstones and sands deposited in a high energy lagoon. The Upper Unit consist of sandy channel fills with thickness ranges from 10m to 15m interpreted by Livera (1989) as upper delta plain deposits (Richards, 1992).

The Tarbert Formation is missing in some fault blocks due to the erosion by the Callovian and Kimmeridgian/base Cretaceous unconformities (Johnsen et al., 1995). It primarily consists of shoreline sandstones and lower delta plain heterolithics deposited during the retreat of the Brent Delta (Ravnås et al. 1997).

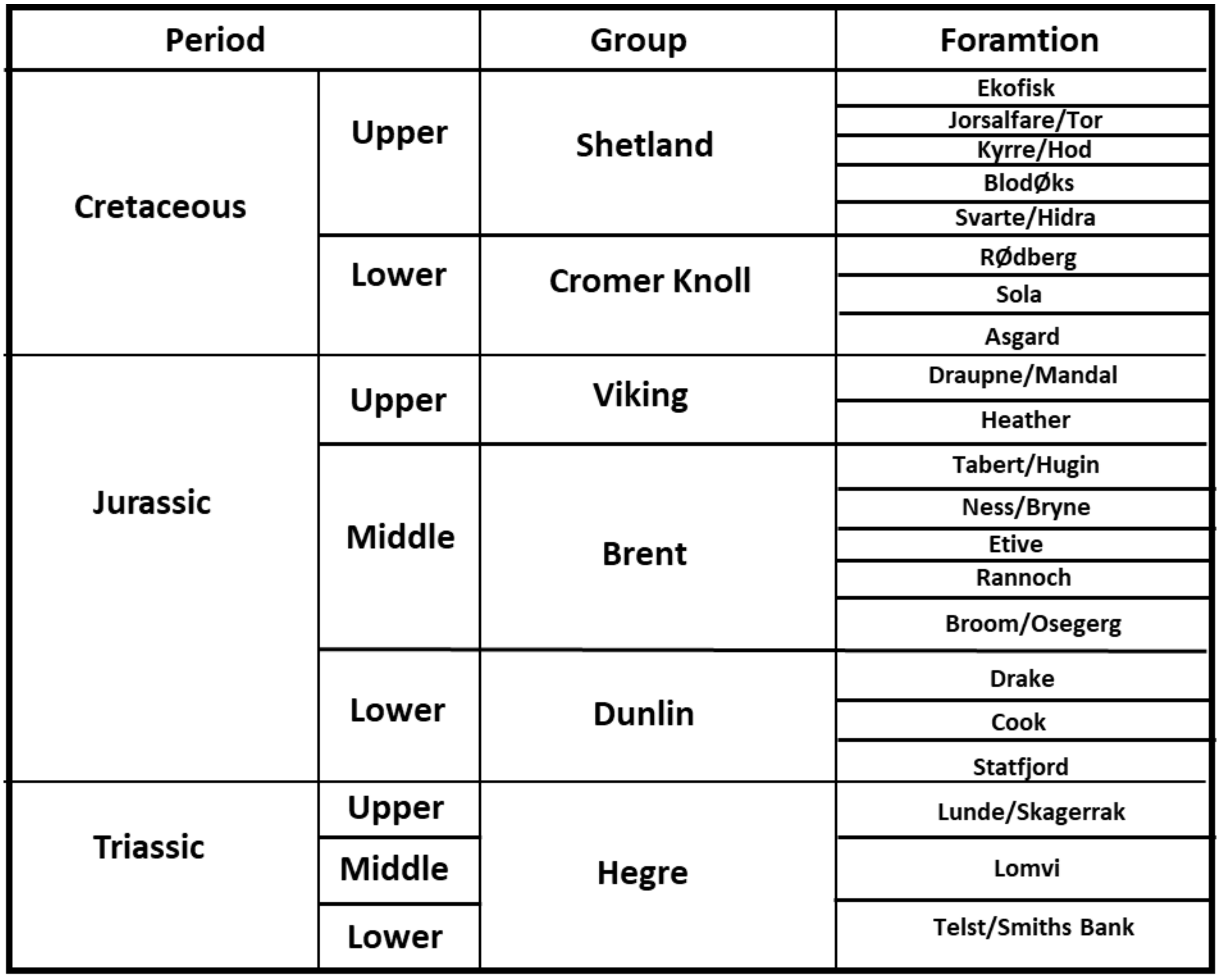

Period		Group	Foramtion
Cretaceous	Upper	Shetland	Ekofisk
			Jorsalfare/Tor
			Kyrre/Hod
			BlodØks
			Svarte/Hidra
	Lower	Cromer Knoll	RØdberg
			Sola
			Asgard
Jurassic	Upper	Viking	Draupne/Mandal
			Heather
	Middle	Brent	Tabert/Hugin
			Ness/Bryne
			Etive
			Rannoch
			Broom/Osegerg
	Lower	Dunlin	Drake
			Cook
			Statfjord
Triassic	Upper	Hegre	Lunde/Skagerrak
	Middle		Lomvi
	Lower		Telst/Smiths Bank

Figure 2.3: The main elements of Mesozoic stratigraphy of the North Sea Viking Graben and Central Graben. Modified after (Pedersen et al. 2006)

3 Theory

In this chapter the theory and concepts used in this thesis will be briefly summarized. Section 3.1 defines the wavelet and describes its use. Section 3.2, 3.3 and 3.4 introduce the principle of seismic inversion and then discuss the inversion methods used in this study. Finally, section 3.5 explains the calculation of the facies models discussed in this study.

3.1 Wavelet

By combining an infinite set of the sine function with the correct relative amplitude and phase the seismic wavelet is obtained (Sim and Bacon, 2014). The wavelet is defined by its amplitude and phase spectrum. The amplitude spectrum describes the amplitude variation of the sine waves with frequency while the phase describes the relative shift of the sine wave at each frequency (**Figure 3.1a and c)**Typically, the wavelet is needed for the synthetic trace calculation or seismic inversion.

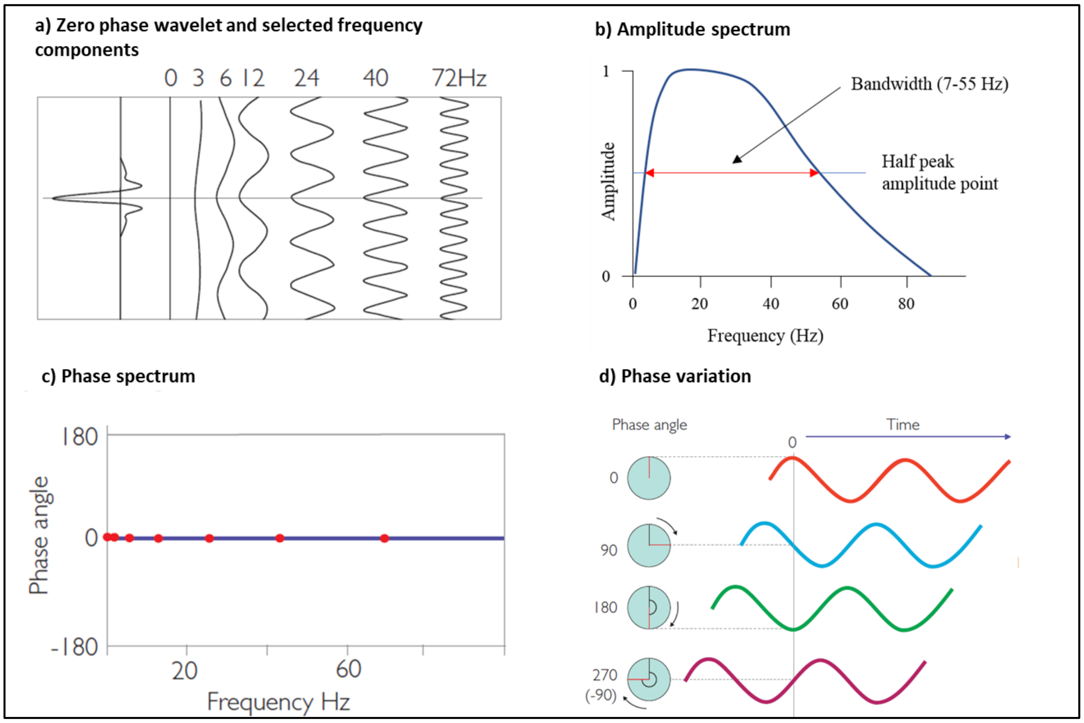

Figure 3.1: Elements of seismic wavelet; a) Sinusoidal frequency components, b)Amplitude spectrum of a wavelet, ,c)phase spectrum d) Four waveforms with the same frequency but different phase. Modified after Simm and White, (2002).

A seismic well tie is needed for correctly identifying the seismic horizons to pick with the help of the synthetic trace (White and Simm, 2003). There are several wavelet extraction methods available such as: analytical, statistical, and deterministic. Those wavelets that give a good match with the seismic via the synthetic can be applied for inversion. However, it has been observed that wavelets giving a similar good seismic match may give different inversion results.

3.1.1 Analytical method

Analytical wavelets are idealized wavelets and are commonly used for synthetic trace calculation when the exact wavelet is unknown. Some examples are shown in **Figure 3.2**.

The Butterworth wavelet is defined by a lower and an upper cutoff frequency. In addition, based on the amplitude spectrum of the wavelet the slopes from the amplitudes at the cut-off frequencies down to zero need to be defined. The wavelet is characterized by several small sidelobes (Sim and Bacon, 2014).

The Ricker wavelet (Ricker, 1940) is defined by a single central frequency and has only two small sidelobes. This type of wavelet offers limited control over the amplitude spectrum thus Hosken (1988) advised against using Ricker wavelets.

Lastly, the Ormsby wavelet is defined by four corner frequencies: low-cut, lowpass, high-pass and high-cut. Similar to the Butterworth wavelet it has several small sidelobes.

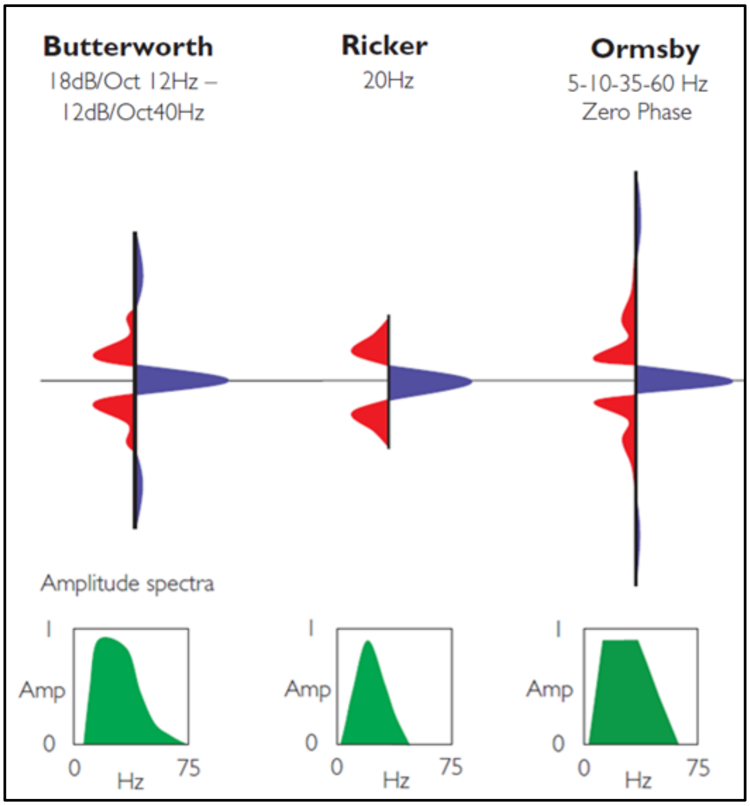

Figure 3.2 Example of analytical wavelets modified after Simm and Bacon, (2014).

3.1.2 Statistical wavelets

The statistical method transforms the tapered autocorrelation of the input seismic traces typically selected from an area around the well location into the frequency domain. Their spectra are averaged and back-transformed into the time domain. Note that the autocorrelation function has a zero-phase spectrum and consequently the statistical wavelets are zero-phase and therefore symmetrical around the peak amplitude (**Figure 3.3**).

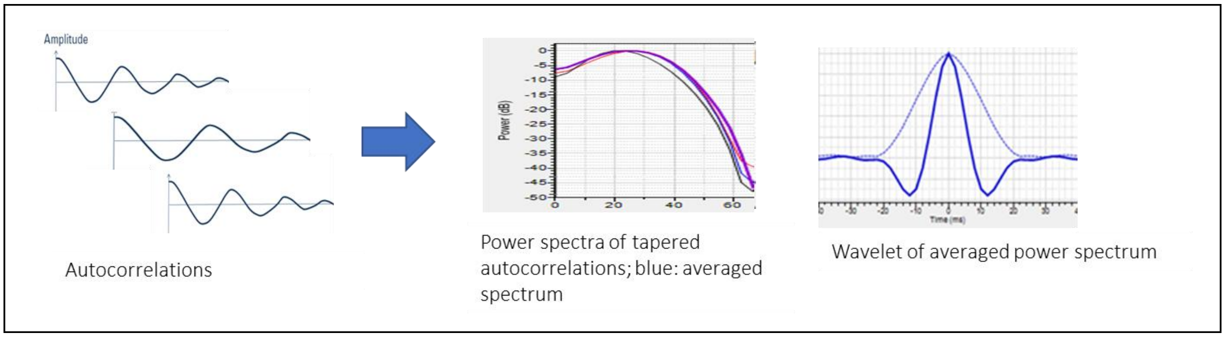

Autocorrelations

Power spectra of tapered autocorrelations; blue: averaged spectrum

Wavelet of averaged power spectrum

Figure 3.3: General workflow describing a statistical wavelet. Modified after Petrel Quantitative Interpretation, (2015).

3.1.3 Deterministic wavelets

The deterministic wavelet is extracted from the seismic trace with the help of the reflectivity generally derived from the sonic and density log. Next to the amplitude information, this wavelet contains a non-zero phase spectrum. Since in most cases seismic data is not exactly zero-phase the synthetic trace based on the deterministic wavelet often matches the seismic trace better than one based on a zero-phase wavelet.

3.1.3.1 Isis wavelet extracted in the frequency domain

A number of wavelets of different lengths and different delays are defined. The synthetic trace is calculated for each wavelet and transformed into the frequency domain. Using the least-square method the wavelet that shows a minimum difference with the seismic spectrum is selected.

3.1.3.2 Extended White wavelet

The wavelet calculated by the Extended White method is derived from the cross-correlation between the seismic trace and the reflectivity calculated from the well log impedance and the autocorrelation of the reflectivity (White, 1980).

According to the convolution model the seismic trace s is given in the time domain t by the convolution of the reflectivity Rc with the wavelet W plus noise N:

$$S(t) = W(t)^* \, Rc\,(t) + N \tag{1}$$

It follows for the wavelet W:

$$W(t) = Rc\,(t) \text{ x } S(t) \,/\, Rc\,(t) \text{ x } Rc\,(t) + N(t) \tag{2}$$

Or

$$W(t) = Rc\,(t) \text{ x } W(t) \text{ x } Rc\,(t) \,/\, Rc\,(t) \text{ x } Rc\,(t) + N(t) \tag{3}$$

Here the symbol ‘x’ stands for correlation.

Converting equation 3 into the frequency domain we get:

$$w(f) = \frac{Crs(f)}{Crr(f)+N} \tag{4}$$

where $w(f)$ is the wavelet, $Crs(f)$ is the cross correlation of the reflectivity and the seismic trace in the frequency domain, Crr(f) is the autocorrelation of the reflectivity in the frequency domain and N is the white noise factor.

It follows from equation 3 that the wavelet contains both, amplitude and phase information: the reflectivity is comparable with ‘white noise’ and has a zero-phase spectrum.

3.2 Seismic Inversion

Post-stack seismic inversion can be defined as the process of deriving the acoustic impedance from the seismic data. Variations in acoustic impedance computed from the seismic volume can be related to reservoir properties, such as porosity and lithofacies thus making the inverted data suitable for reservoir characterization (Shiv et. al., 2000).

The principle of seismic inversion can be explained as the reverse of the convolution model (**Figure 3.4)**. As stated in section 3.1.3.2 the seismic trace is a result of the convolution between the reflectivity coefficient (Rc) and the wavelet (W). Seismic inversion starts from the seismic trace, removes the imprint of the wavelet from it and converts the results to impedance. An example of seismic inversion is the relative acoustic impedance model which has a similar amplitude spectrum than the input seismic reflecting the band-limit of the seismic data. The alternative way of seismic inversion is the modelling approach which starts from an estimation of the acoustic impedance. The acoustic impedance is modified until the synthetic derived from the data matches the seismic **(Figure 3.4).**

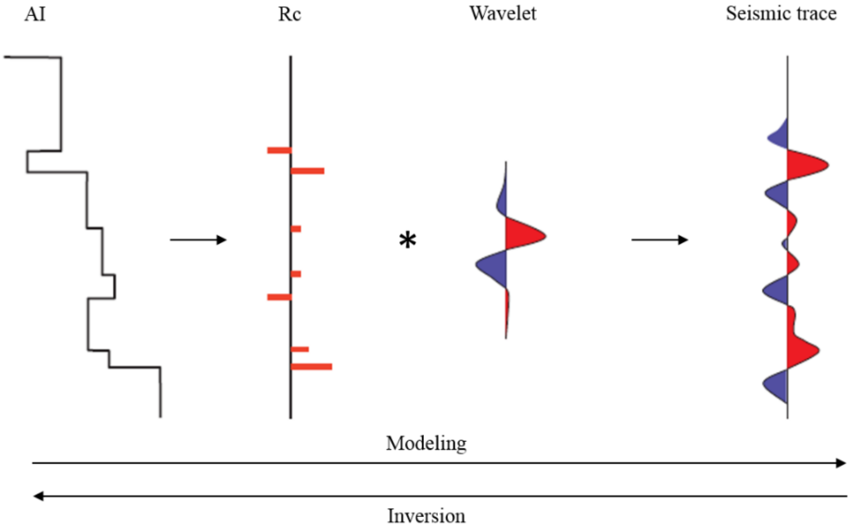

Figure 3.4: Process of forward modeling (left to right) versus seismic inversion (right to left). Frette (2018), modified after Simm and Bacon, (2014).

Seismic inversion can be divided into two main types: deterministic inversion and stochastic (geostatistical) inversion (Simm and Bacon, 2014). Deterministic inversion is commonly used in the industry. It relies on optimization techniques to minimize the error between the synthetic trace coming from the modelled impedance and the seismic resulting in a best-estimate model (Francis 2006a, Azevedo 2018). There are several different approaches to deterministic inversion such as recursive inversion, sparse spike inversion and model-based inversion which are described by Russel (1988). However, only the model-based inversion will be further discussed as it is the method used in this study.

While deterministic inversion delivers the best-estimate result of the invers problem, stochastic inversion addresses the variability of the inverse solutions. Therefore, stochastic inversion does not provide a single result but multiple realization all of them honoring both well data and seismic data (Simm and Bacon, 2014). There are different approaches towards stochastic inversion such as the Bayesian method (Buland and Omre 2003; Gunning and Glinksy 2004) or methods based on the perturbation of the model parameter space in a stochastic manner (Azevedo, 2018).

3.3 Model-based inversion

The model-based inversion is based on an iterative forward modeling and a comparison procedure (Veeken and Da Silva, 2004; Simm and Bacon, 2014). **Figure 3.5** shows the general workflow for the model-based inversion. The seismic horizons are used to guide the log data in order to create a starting model also known as low frequency model (LFM). Then a trace of the LFM is taken together with the wavelet extracted from the seismic in order to create the synthetic trace. This synthetic trace is compared with the actual seismic trace at the same location and the mismatch is measured. The impedance trace is updated, and the procedure continued until the mismatch between the synthetic trace and the seismic trace is minimized. Then the process starts again with the next trace coming from the LFM (Simm and Bacon, 2014).

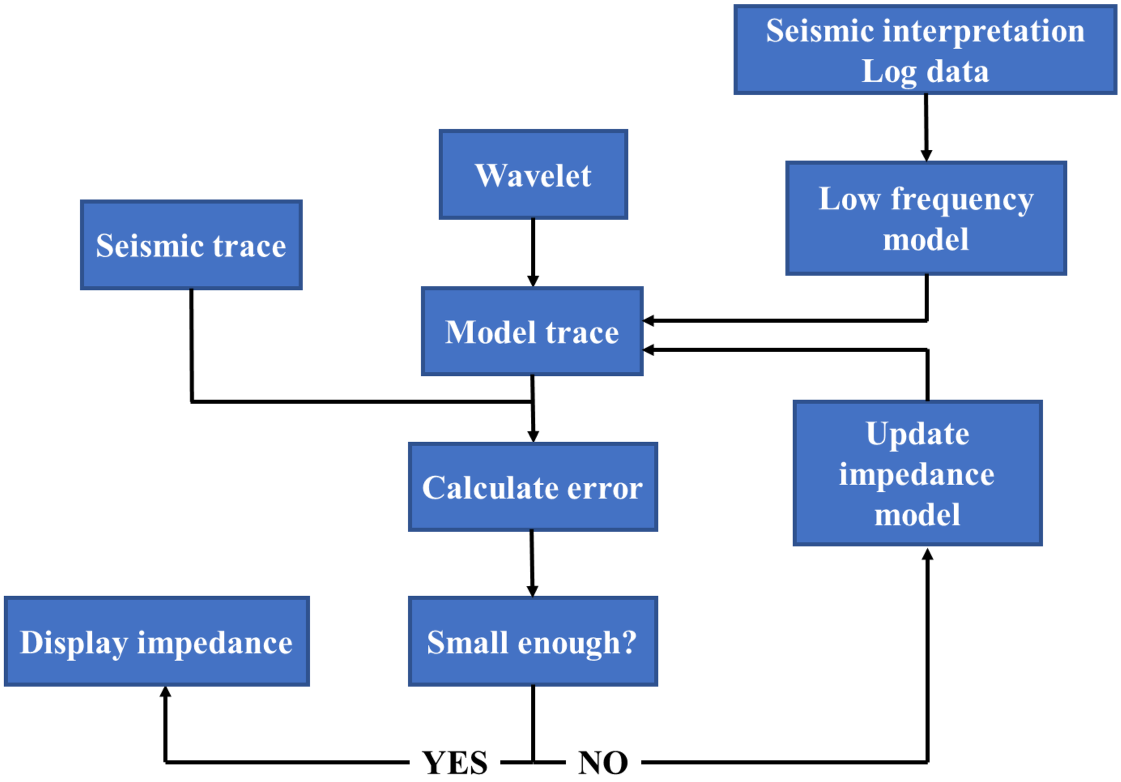

Figure 3.5 Model-based inversion flow-chart. An initial impedance (low frequency) model, based on log data and guided by the seismic horizons and the extracted wavelet serves as an input to create the model trace. If the misfit between the model trace and the seismic trace is small enough the impedance model is displayed or else the model is updated. Modified after Simm and Bacon, (2014).

Several implementations of the deterministic inversion operate by trying to minimize a function that measures various quantities such as the misfit with the respect to the seismic, the smoothness of the model or the number of reflectors. This function is called the cost function or the objective or penalty function.

The deterministic inversion used in this study iteratively updates the elastic parameters of the subsurface model until the objective function is minimized (Petrel Quantitative Interpretation, 2015). It is a global optimization, meaning that the cost function is optimized for the entire dataset with no subdivision This feature is important because inversion techniques using global optimization can use a complex objective function with many local minima corresponding to realistic statistical models for subsurface prediction from seismic data.

The global optimization ensures that the subsurface model does not become trapped at a model corresponding to one of the many local minima, but that the final optimum model corresponds with the global minimum. **Figure 3.6** illustrates this concept.

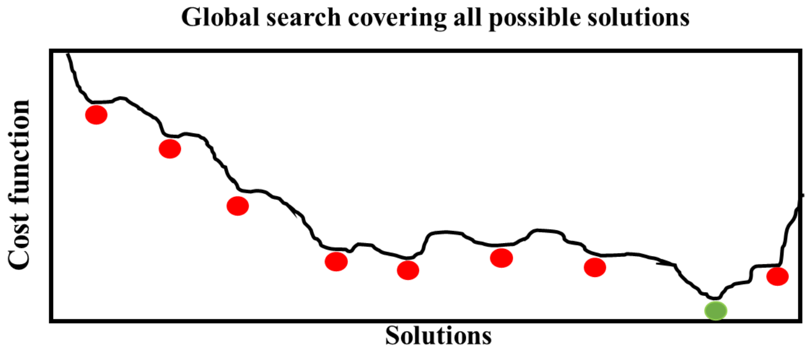

Figure 3.6: Conceptual representation of the global optimization process. Modified after Petrel Quantitative Interpretation, (2015).

The cost function for the Petrel deterministic inversion contains these terms:

- Penalty for differences between the seismic data and synthetic seismic determined from the estimated property model by convolutional forward modeling;
- Penalty for horizontal variations in the estimated property model;
- Penalty for deviation of the estimated property model from the low frequency model;
- Penalty for the presence of significant reflectors. Significant reflectors are places in the estimated property model where the reflection coefficient exceeds a predefined threshold.
- Penalty for vertical changes in properties between the significant reflectors.

Expressed as a formula, the objective function is shown in **Table 3.1:**

Term	Interpretation
E= $f(SNR) \times \sum (Si - di)^2$	Penalty for not fitting the seismic
$+ f({}^{1}/_{R\alpha}) \times \sum C_i (P_i - P_{i\pm1})^2$	Penalty for horizontal variation
$+ f({}^{1}/_{R\sigma}) \times \sum C_i (P_i - P_{LFM})^2$	Penalty for deviations from the low frequency mode
+ R1(#significant reflectors)	Penalty for number of reflectors that exceed treshold

Table 3.1: The objective function formul used by deterministic inversion. Modified after Petrel Quantitative Interpretation, (2015).

3.3.1 Low frequency model

The low frequency model is needed because of the band-limited nature of the seismic data which is generally lacking low frequencies describing the trend, and high frequencies responsible for the resolution (**Figure 3.7**). The frequency spectrum of the seismic data is usually in the range of 7-55 Hz (Hassan et al., 2015).

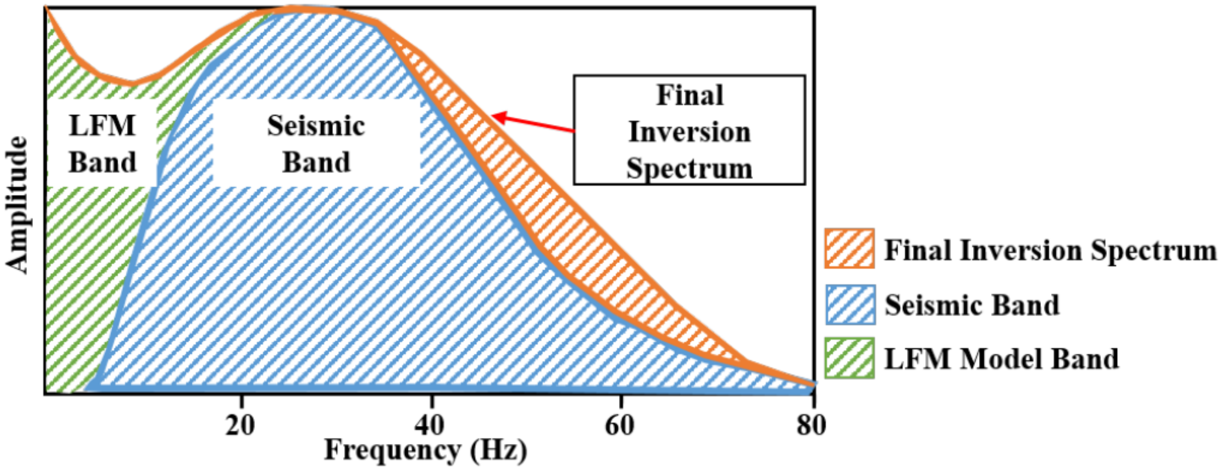

***Figure 3.7**: Frequency versus Amplitude plot illustrating the band-limited nature of seismic. Note how the Low Frequency Model (LFM) fill the band below the seismic. Adlakha, (2018) modified after Pendrel and Van Riel (2000).*

Because of the missing low frequencies, it is impossible to derive an absolute acoustic impedance model from the seismic traces. **Figure 3.8** illustrates a simple impedance layer model which is filtered for three different frequency ranges (Latimer et. al. 2000). When the frequency of the wavelet ranges between 10-80 Hz (**Figure 3.8a)** the inverted acoustic impedance fails to match the acoustic impedance log. This situation does not change when higher frequencies are added (**Figure 3.8b**). However, when the low frequencies are included the inverted data fit the log data. Consequently, in order to obtain an absolute acoustic impedance of the seismic traces, the seismic frequency range is combined with a low frequency model. The LFM is derived from well log data which is interpolated and guided by the seismic horizons in order to add the trend and accuracy for deriving the absolute acoustic impedance (Sams and Saussus, 2013).

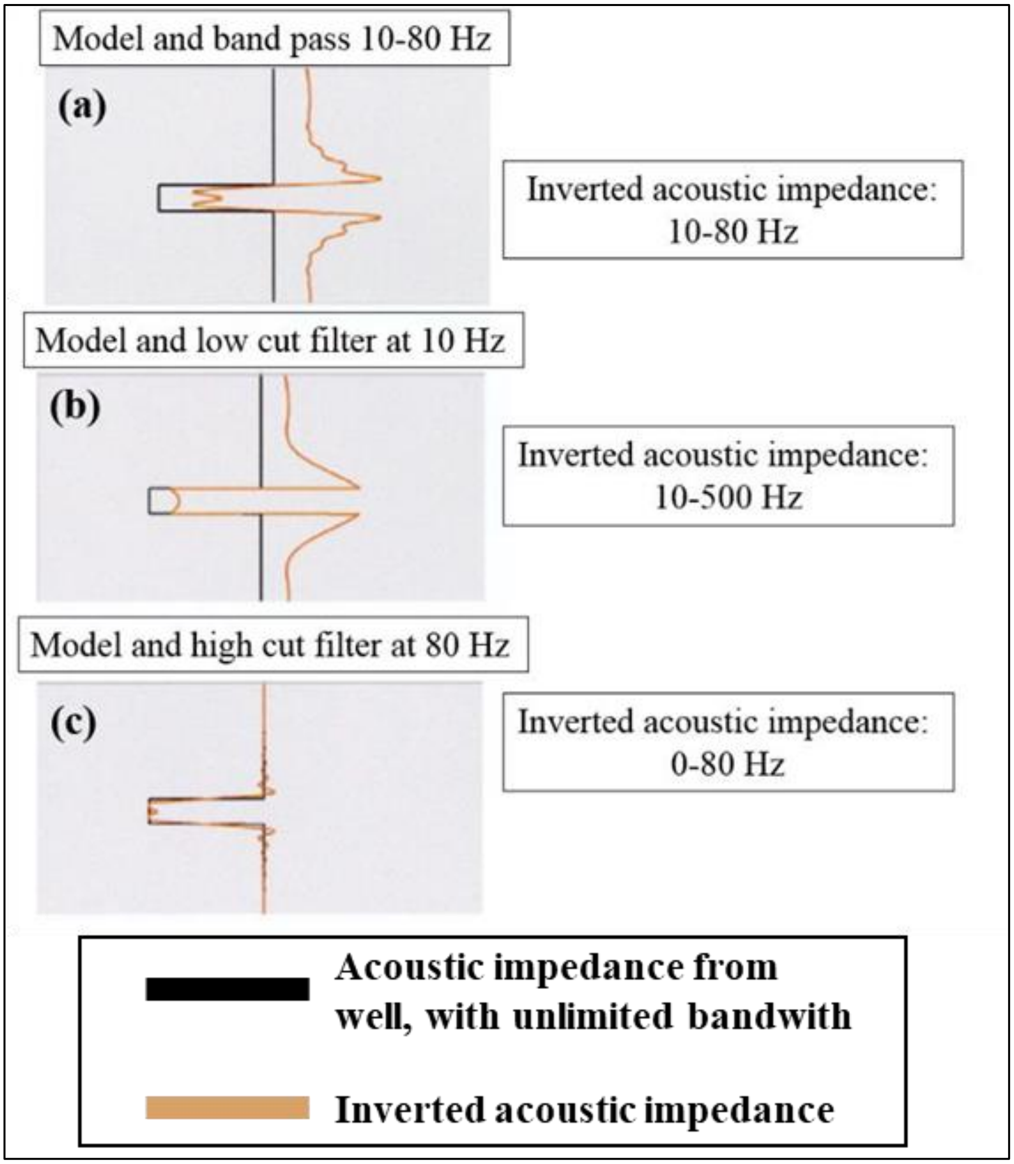

Figure 3.8 An impedance model explaining the importance of low frequencies in seismic inversion. (a) An inverted acoustic impedance using wavelet of 10-80 Hz, (b) An acoustic impedance created using wavelet of 10-500 Hz and (c) includes the low frequencies from 0-80 Hz. The model (c) gives a more reliable impedance compared to acoustic impedance from the well log. Modified after Latimer et al. (2000).

3.3.2 Inversion QC

While the wavelet and LFM model are needed for a successful inversion, these parameters also represent uncertainties as they may introduce artefacts which are not representative of the geology. Therefore, the inversion results must be quality checked (QC). There are two main common ways of doing it.

The first method represents the comparison between the original seismic and the synthetic seismic generated from the inverted impedance using the wavelet (**Figure 3.9a and 3.9b**). The difference between these two is the residual cube which for a successful inversion should show very low amplitudes (**Figure 3.9c**). In case of an unsuccessful inversion, the residual cube would show significant reflectors because the synthetic seismic would not be in agreement with the original seismic. However, because the model-based inversion delivers one, best-fit result from an infinite equiprobable possibilities, a small misfit between the seismic and the synthetic seismic does not guarantee the right answer (Simm and Bacon, 2014).

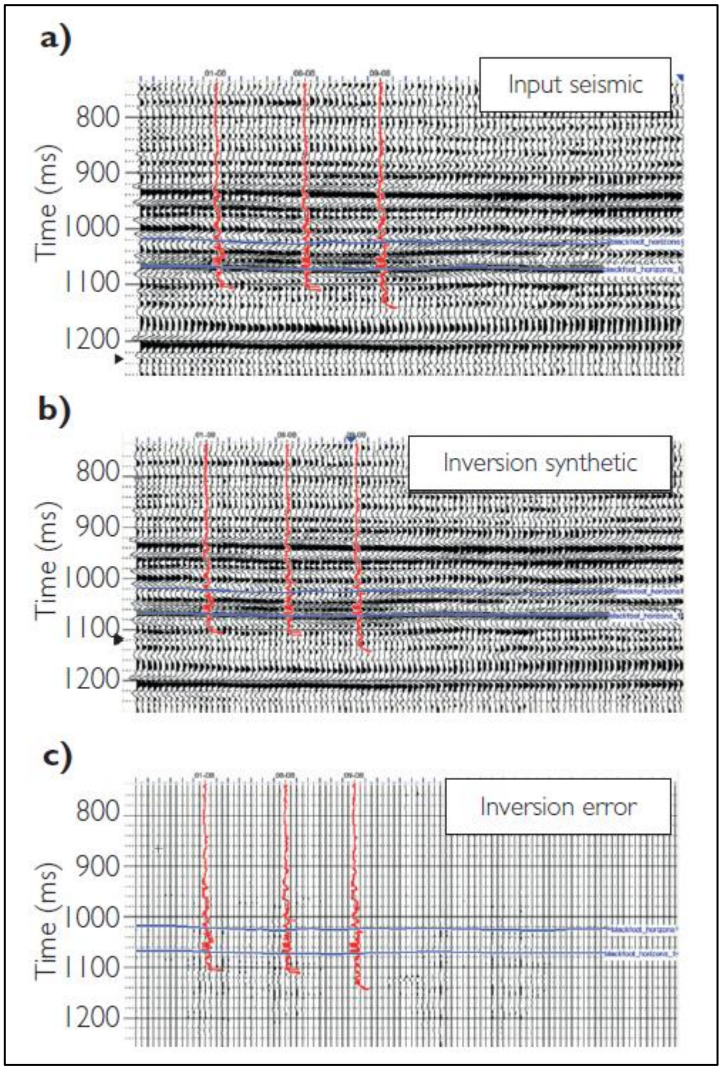

Figure 3.9 a) Original seismic used for inversion. B) Synthetic seismic calculated from the inversion. C) Residual cube, the difference between the original and synthetic seismic. Modified after Simm and Bacon, (2014).

This QC method is useful for checking the influence of the wavelet. However, the impact of the LFM cannot be assessed by checking the synthetic seismogram, as the original seismic is missing the low frequencies. Therefore, another way of checking the inversion result is by comparing the modeled acoustic impedance derived from the inversion process with the impedance log at a well location (**Figure 3.10**). This method allows to investigate the scaling of the wavelet. If the scaling is correct, then the amplitude of the inverted acoustic impedance should match the impedance well (Simm and Bacon, 2014). Also using the seismic well tie, the impedance zones can be checked by the well tops as wavelets can sometimes cause a time shift in the resulting impedance model. Lastly the influence of the LFM can be checked and the cut-off can be adjusted until a good match is encountered.

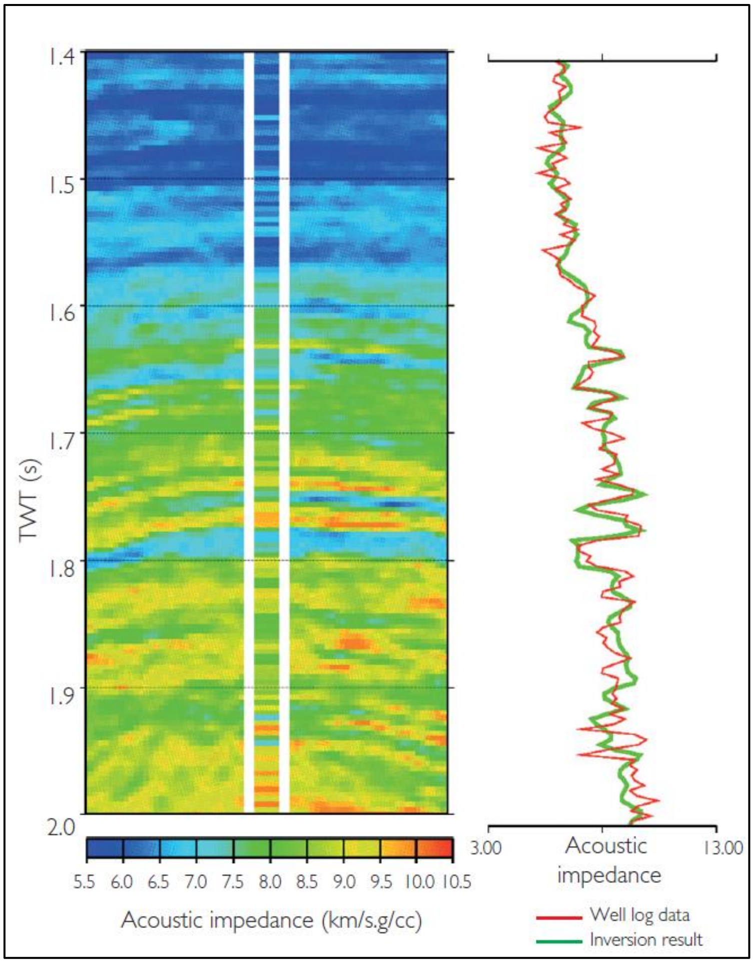

Figure 3.10 Comparison between the inverted impedance result and the impedance log at the well location. Modified after Bach et al., (2000).

3.4 Stochastic inversion

The first stochastic or geostatistical inversion methods were introduced by Bortoli et al. (1992) and Haas and Dubrule (1994) and came as a necessity to address the non-unique solution due to the band limited nature of seismic (Tarantola 2005). Whilst model-based inversion is providing one best-estimate result, stochastic inversion delivers multiple realizations that honor the seismic data thus allowing for an uncertainty estimation.

Figure 3.11 displays an example of stochastic inversion showing multiple impedance realizations alongside synthetic sections generated from each realization. This figure illustrates the non-uniqueness of the seismic inversion. Each impedance section is matching the well data and all the synthetic sections are honoring the original seismic. However, the impedance simulations are showing variability and differ from each other. Note how the sand bodies represented by strong acoustic impedance values marked by a blue color vary in both thickness and lateral connectivity between the simulations (Francis, 2006b).

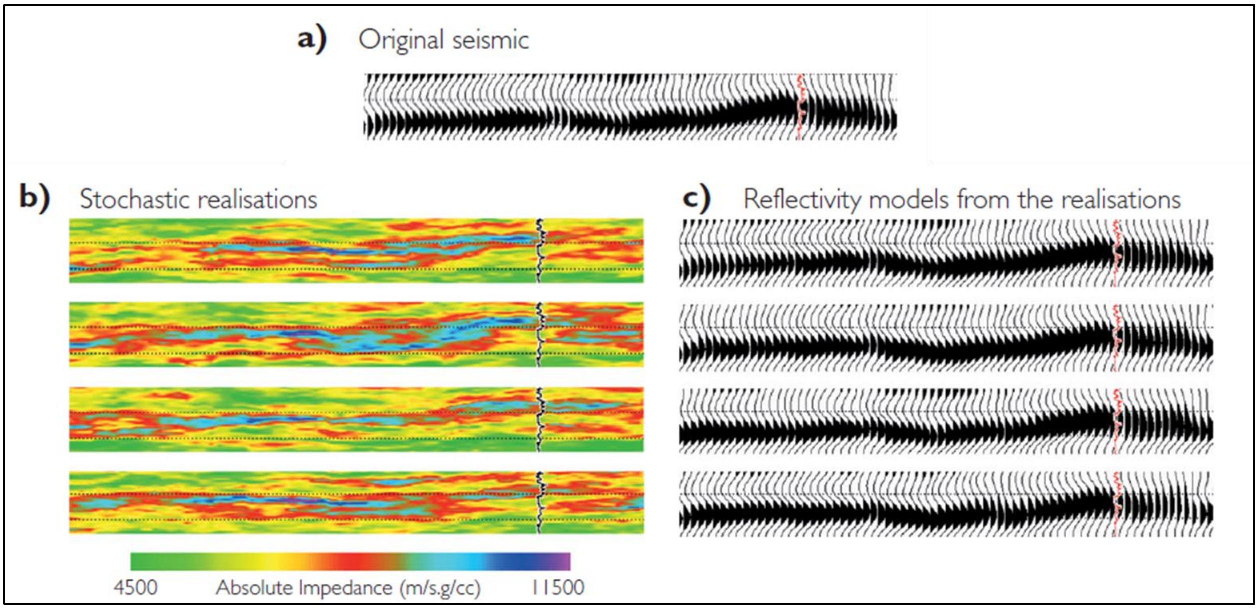

Figure 3.11: Comparison of stochastic inversion results: a) original seisimc, b) muliple realisation from stochastic inversion and c) the synthetic seismic generated from the realisations shown in b). Modified after Francis, (2006b).

By using Sequential Gaussian Simulation (SGS), the stochastic inversion process simulates multiple equiprobable realizations. **Figure 3.12** presents the general workflow used by stochastic inversion. This inversion method is performed on a 3D grid in the time domain. The cell thickness usually varies between 1-4 ms, below seismic resolution (Doyen, 2007). Besides the low frequency model, the high frequencies are added by SGS of the upscaled acoustic impedance log. A large number of "equiprobable" impedance traces are simulated at every trace location visited in a random order (Shiv et al., 2000). The simulation applies kriging to well data to determine a value with its variance for each grid cell along a trace. Then the cumulative distribution function (CDF) is derived from the variance and centered at the kriged value. The final impedance value is simulated through sampling the CDF using Monte Carlo (Sim and Bacon, 2014). Once the impedance trace is calculated, the reflectivity coefficient is derived and convolved with the seismic wavelet in order to create a synthetic seismic trace. The synthetic is compared with the original seismic and if the error is small enough the corresponding trace is stored in the 3D grid. Another seismic trace is then chosen randomly, and the process is repeated until all cells in the grid are populated by impedance values. Multiple realizations can be made by repeating the whole process using different random paths.

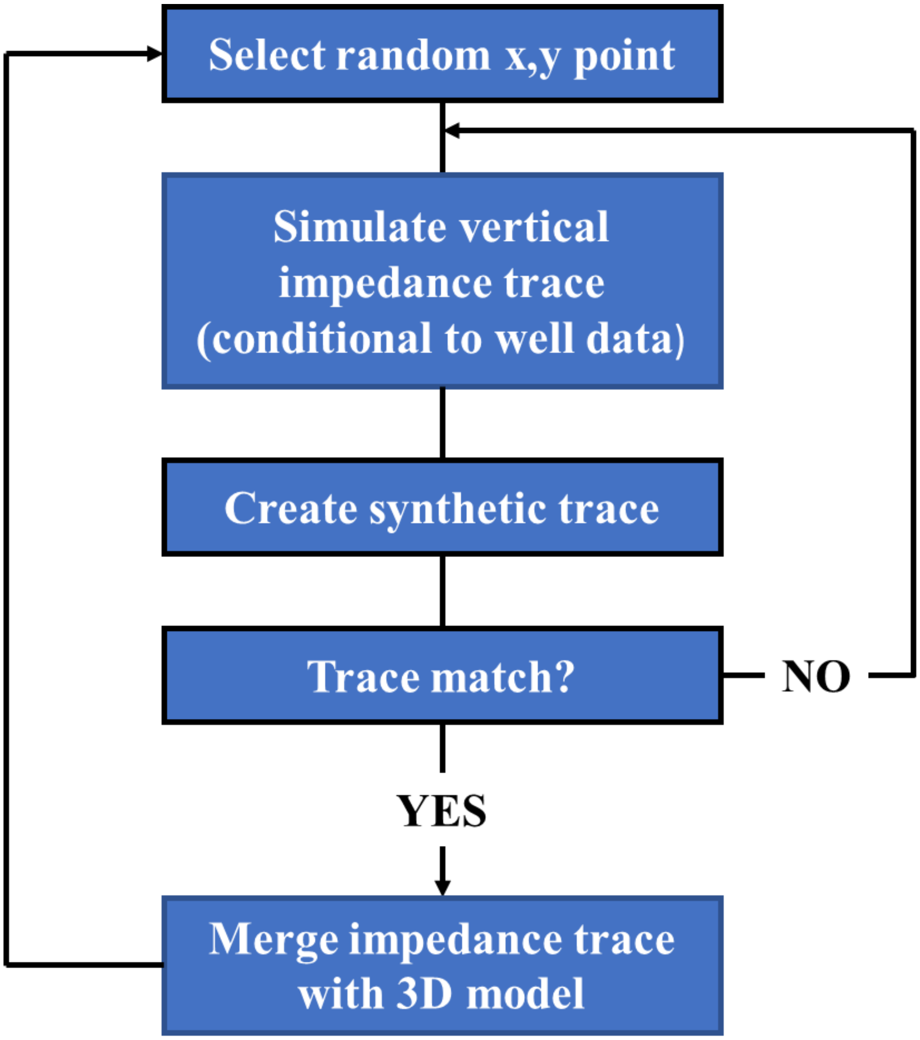

Figure 3.12 General worklow for stochastic inversion using Sequential Gaussian simulation modified after Haas and Dubrule, (1994).

Although stochastic inversion can be run at any sample rate given by the grid resolution, it should be mentioned that stochastic inversion remains influenced by the seismic frequency band (Francis, 2006b). In geostatistical inversion, the high frequencies are not inverted from the seismic data but are simulated from the well data and controlled by the vertical variogram model generating multiple impedance models, all in agreement with the original seismic (**Figure 3.13**). Lastly, if enough realizations are averaged, the result would be a smooth mean model equivalent to the result from the model-based deterministic inversion.

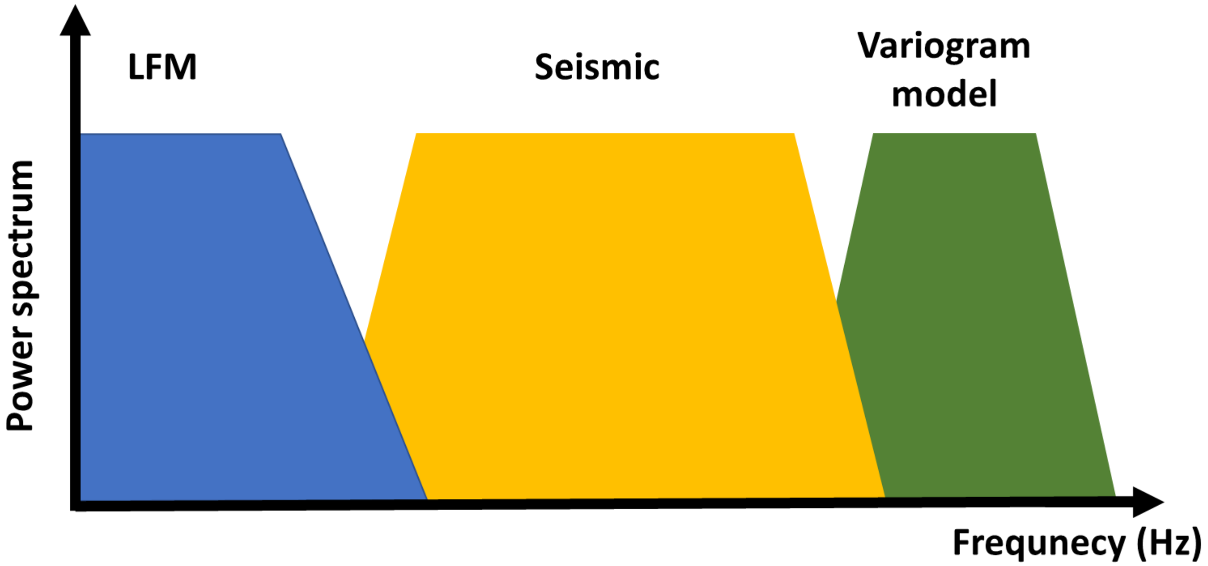

Figure 3.13: Typical normalized amplitude spectrum of seismic data. The low frequencies are added by the LFM while the higher frequencies are added by the variogram model. Modified after Dubrule , (2003).

3.4.1 Variogram

The variogram controls the spatial distribution of the model parameters (Ringrose and Bentley, 2015). It provides the relationship between the differences of individual data pairs (variance) and the distance between them. It can be expressed by the following function:

$$\gamma(h) = \frac{1}{2}\mathrm{E}\left\{[Z(x+h) - Z(x)]^2\right\} \qquad (2)$$

where γ represents the semivariance, Z(x) is the data point of a certain parameter in space and Z(x+h) is the data value at separation distance, h also known as the lag.

A semivariogram model (**Figure 3.14**) is created when the variogram points are approximated by an analytical function. The model is needed for instance for kriging or Gauss simulation. The semivariogram model is defined by three main features: the range, the sill and the nugget. The range controls the distance at which the data pairs exhibits no longer any relationship between each other. The sill can be defined as an average semi-variance value that is approached by data pairs of a separation distance (lag) larger than the range (Ringrose and Bentley, 2015). The nugget expresses the sudden variation between very closely spaced data pairs, and it can be related to random noise or to variations caused by a scale smaller than the sample rate (Doyen, 2007).

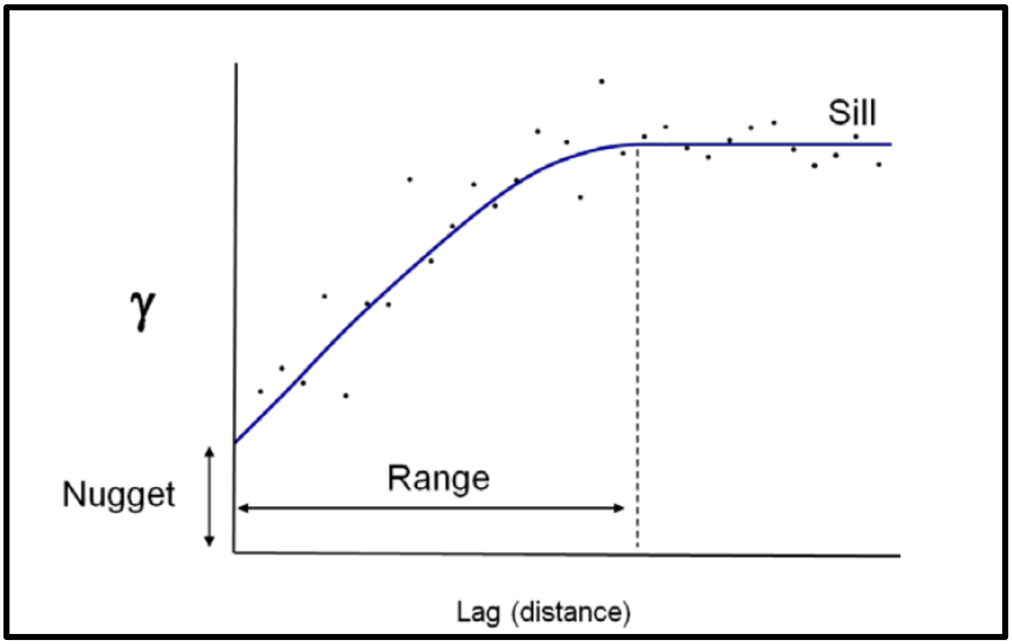

Figure 3.14 A semivarigram model fiited to the data points displaying the three main defining features :the sill, the nugget and the range. Modified after Ringrose and Bentley, (2015).

In stochastic inversion the variogram controls the vertical and lateral distribution of the acoustic impedance realizations. The vertical variogram which constrains the higher frequencies is derived from well data. However, there aren't usually enough wells to reliably derive the lateral variogram parameters, which are responsible for the connectivity of the modeled impedance. Therefore, the lateral variogram is often derived from geological analogues, amplitude or impedance maps (Sim and Bacon, 2014).

Figure 3.15 illustrates examples of vertical and lateral variograms. Sometimes the variogram varies horizontally with spatial direction, and the variogram values along different ranges will describe an elliptic distribution as shown in **Figure 3.15b**. This is called geometric anisotropy and is characterized by two principal axes along which the major and the minor range are derived (**Figure 3.15d**). The orientation of the ellipse is measured by the azimuth of the major axis, which corresponds to the direction of greatest lateral continuity (Doyen, 2007). In case the two perpendicular horizontal directions deliver variograms of different sills we talk about zonal anisotropy (**Figure 3.15c**). If the values of sill and range from the variogram along all horizontal directions are the same, then the data is regarded as isotropic (Sim and Bacon, 2014).

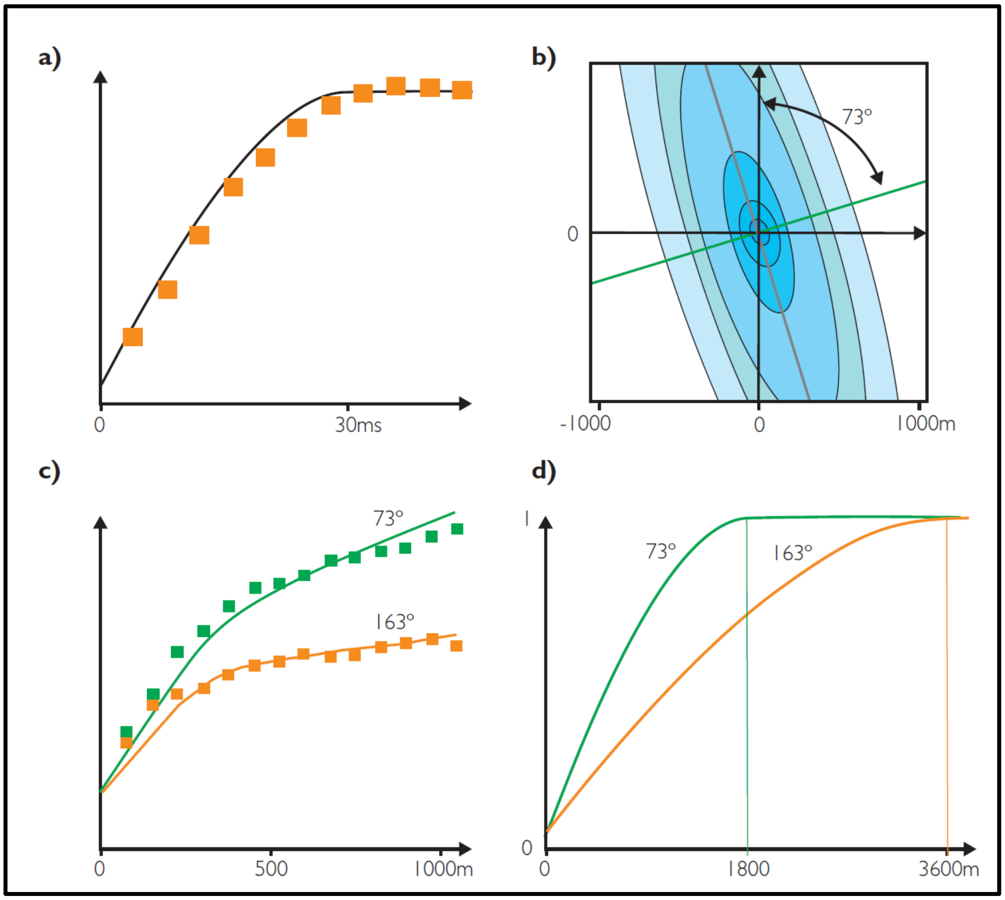

Figure 3.15 Example of variogram used for stochastic inversion. a) vertical variogam derived from well impedacne. b) Variogram map exibiting anisotropy of the data. c) Horizontal variograms showing zonal anisotropy). d) Horizontal variograms showing geometrical anisotropy Modified after Hass and Dubrule, (1994).

3.4.2 Inversion QC

As in deterministic inversion, the results from stochastic inversion have to be quality checked. The comparison between the synthetic cube derived from the stochastic inversion and the original seismic can be accomplished. Another method is the blind well test which allows to include the low frequency part of the inversion in the QC process (Simm and Bacon, 2014).

The software used for the stochastic inversion includes an automatic procedure for QC of the inversion results. These are the Sequence, Cost, Converged and Iteration attributes which are explained in the following.

The Sequence attribute reveals the order the cells were visited during the inversion process. The Cost function represents the correlation between the synthetic and the original seismic. The converged diagnostic is a Boolean attribute. It is set to 'True' if the cost function is above a user defined threshold value. Otherwise it is set to 'False'. An acceptable convergence value is 0.8 meaning that the correlation between the seismic and the synthetic trace is 80% or higher. The Iteration diagnostic shows the number of iterations needed to successfully converge to an acceptable solution defined by the threshold value of the cost function. If the number of iterations is low, it means that the inversion process was able to fit the data. If the number of iterations is equal to the maximum number given by the user, it indicates that the cost function is low, and the impedance at these cells did not successfully converge to a reliable solution (Petrel Quantitative Interpretation, 2015).

Figure 3.16 shows an example of the Cost, Iteration and Converged diagnostic. Note the relationship between them. Where the cost function is low (marked by yellow and green colors) the number of iterations is high (100 tries marked by the red colors). In turn, this corresponds to cells marked by a red color of the converged diagnostic indicating the Boolean flag 'False'.

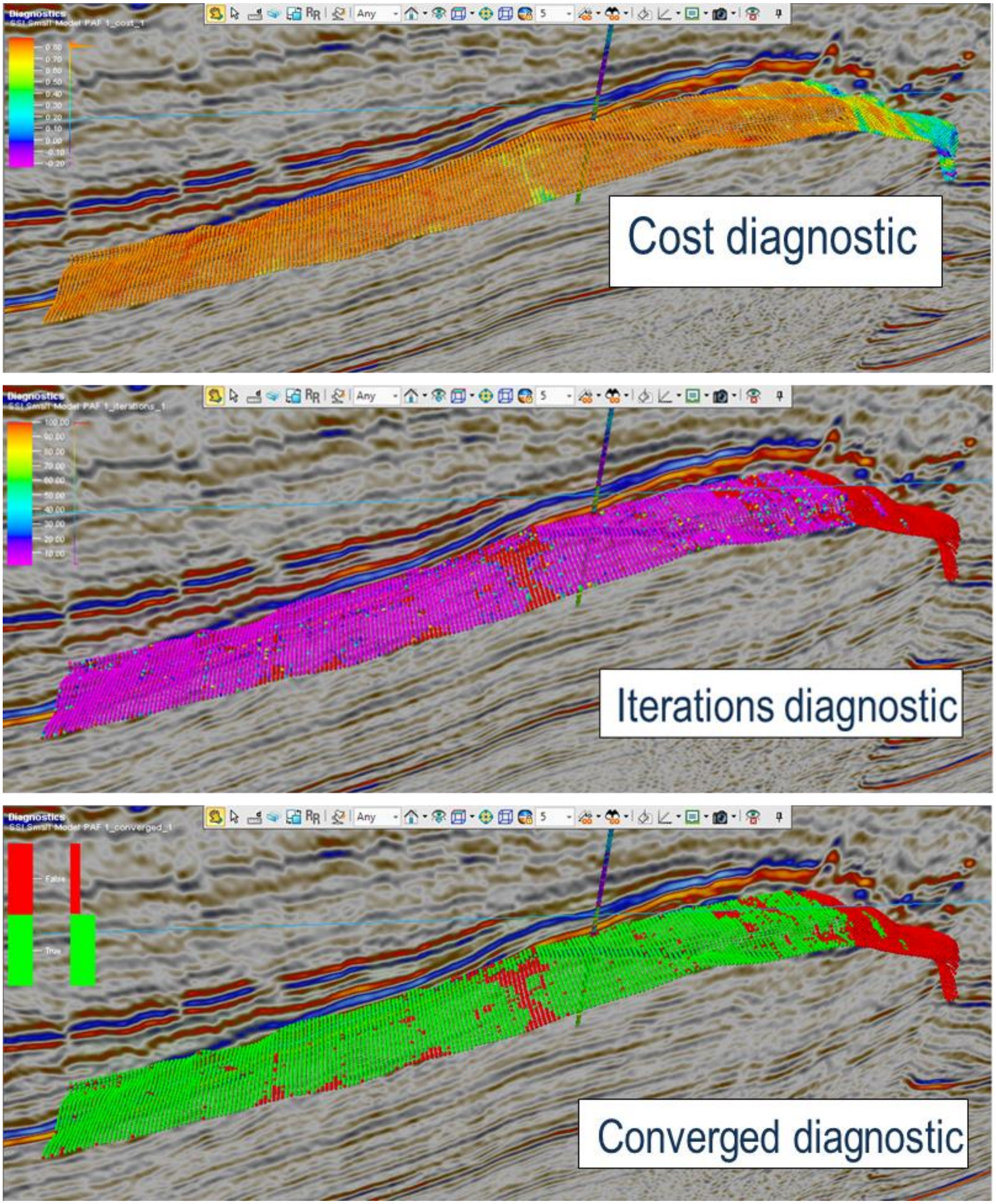

Figure 3.16: Example of the cost, iterations and converged diagnostic. Modified after Petrel Quantitative Interpretation, (2015).

3.5 Facies modeling

This section briefly describes the methods used for facies modeling.

3.5.1 Kriging

Kriging is a geostatistical method developed by Matheron (1963) commonly used for spatial interpolation of a reservoir property (Ringrose and Bentley, 2015). In order to better understand this method, we can use **Figure 3.17** which illustrates an area with data points at Xi and the location X0 where we want to estimate the property. We can use the following formula:

$$Z(x_0) = \sum_{i=1}^{n} \omega_i \, Z(x_i) \tag{3}$$

where $Z(x_0)$ is the unmeasured value at location X0, ω_i are the weights calculated from the variogram model and $Z(x_I)$ are the known values at location Xi.

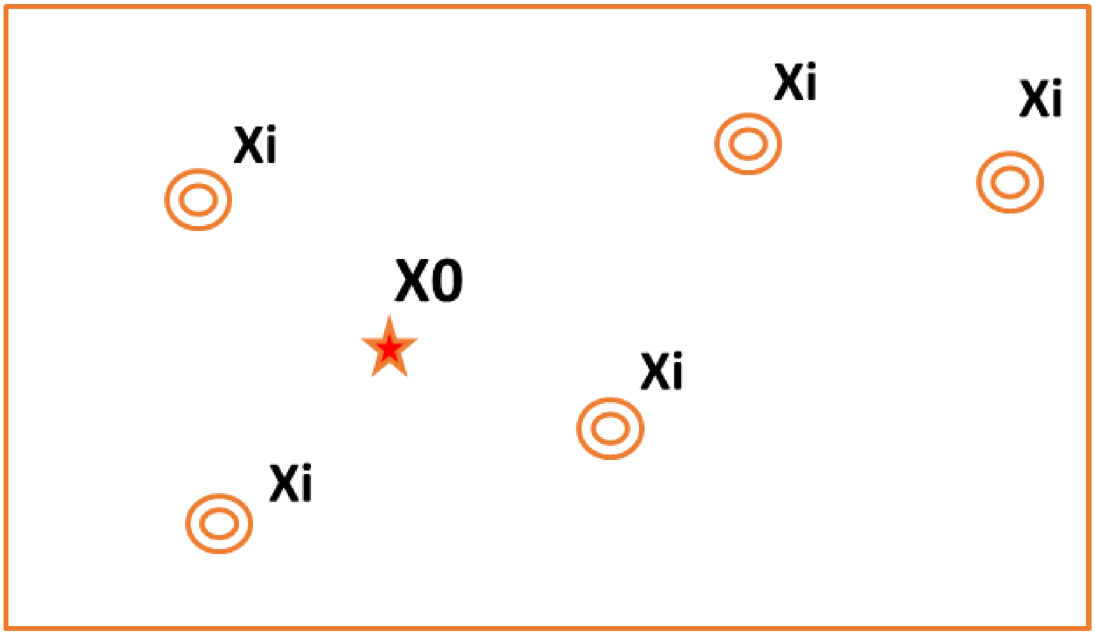

Figure 3.17: Illustration of the kriging method. Modified after Petrel Quantitative Interpretation, (2015).

Kriging is using an objective function to minimize the variance. Therefore, the weights ω_i are used to obtain a minimum expected variance given the known data points $Z(x_i)$.The result of kriging will be smooth and will show less variance compared to the input data. There are several different mathematical approaches of kriging one of it being the Simple Kriging method (Ringrose and Bentley, 2015).

3.5.2 Simple kriging

The Simple Kriging assumes that the mean and distribution are known and considered to be spatially constant. If we consider the example of **Figure 3.17,** Simple Kriging can be defined as:

$$Z(x_0) = \sum_{i=1}^{n} \omega_i \, Z(x_i) + [1 - \sum_{i=1}^{n} \omega_i]m \tag{4}$$

where, $Z(x_0)$ is the unmeasured value at location X0, $Z(x_i)$ are the known values at location Xi, $\sum_{i=1}^{n} \omega_i$ is the sum of the weights which lies between [0….1] and m is the mean derived from all data points.

In order to obtain an estimate of the property, the weights of each data point have to be calculated in order to minimize the error. This can be done by using a semivariogram to quantify the correlation of the points (Ringrose and Bentley, 2015). The smaller the weights the bigger the influence of the mean on the calculated value Z at position x_0. If the wells are close together, they will have a smaller variance or larger correlation and consequently the weights will increase. However, at large distances between location x_0 and the data points, the correlation approaches zero and Simple Kriging will deliver the mean value of the data (Doyen, 2007)**.**

Of critical importance is the accurate determination of the variogram range. The influence of the range is demonstrated in **Figure 3.18**. For a small range, the radius of influence of the data points is small as well and the mean value covers a considerable part of the surface (**Figure 3.18a**). With increasing range, the data points influence a larger area and the area showing values close to the mean becomes small (**Figure 3.18b**). Note that the sample variogram shown in the insets of the figure allows to derive the variogram range quite accurately from the data, which underlines the importance of a reliable variogram evaluation.

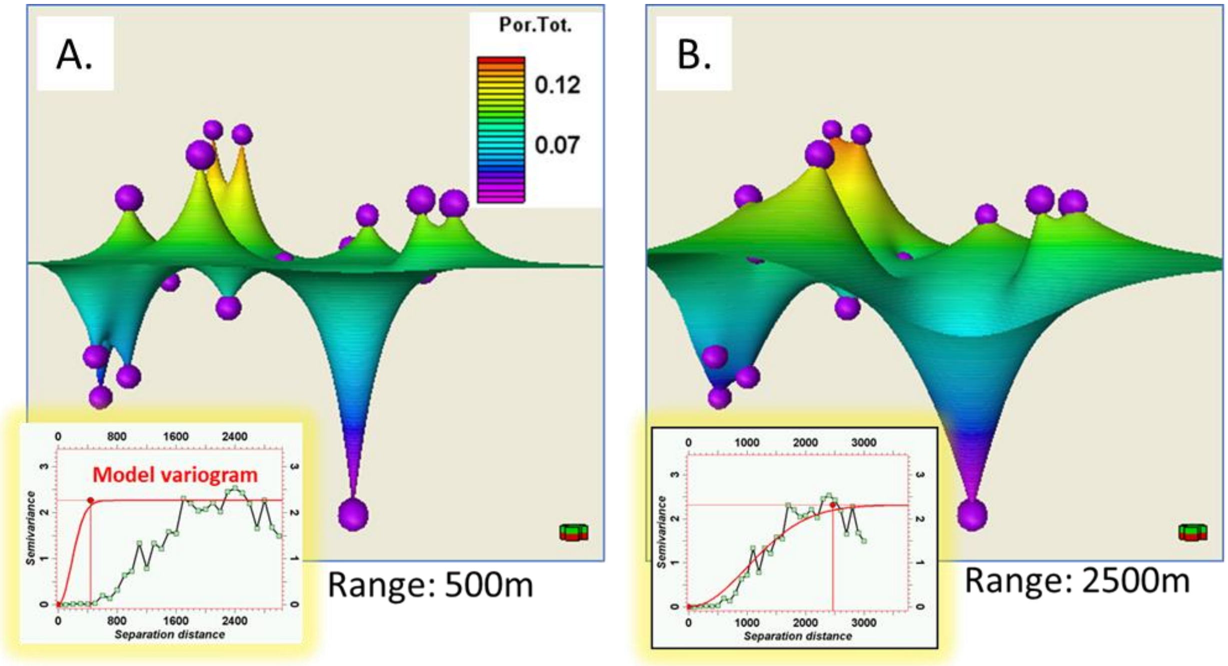

Figure 3.18 Example of porosity mapping using Simple Kriging. A) Porosity map based on a small variogram range which is not supported by the sample variogram shown in the small figure. B) Porosity map based on a large variogram range supported by the variogram. Modified after Petrel Quantitative Interpretation, (2015).

3.5.3 Gaussian Simulation

Sequential Indicator Simulation (SIS) is a generalization of SGS and is described in the conceptual 2D example shown in **Figure 3.19 (**Journel and Gomez-Hernandez, 1989). The map shows how the sand probability is calculated at the grid cell marked by the red cross. All data points that show the facies sand get the sand probability ‘1’. All other data showing different facies get the sand probability of zero. Each cell is visited in a random order. At the grid cell marked by the red cross, using Indicator Kriging (IK) alongside the well data (yellow and blue circles) and the already simulated cells (blue cross), the local sand probability is calculated. In a similar way the probability of all other facies (in this example only the facies shale) will be calculated. Next, the cumulated distribution function for the facies probabilities is set up for each grid cell. Finally, using the Monte Carlo method, a random simulated value between 1 and 0 is drawn and applied to the PDF. The resultant facies is assigned to the grid cell (Jensen et al. 2000). The underlying random number generator is controlled by a user-defined so-called ‘seed’ value. Each seed value is linked to a random number. This allows to reproduce simulation results.

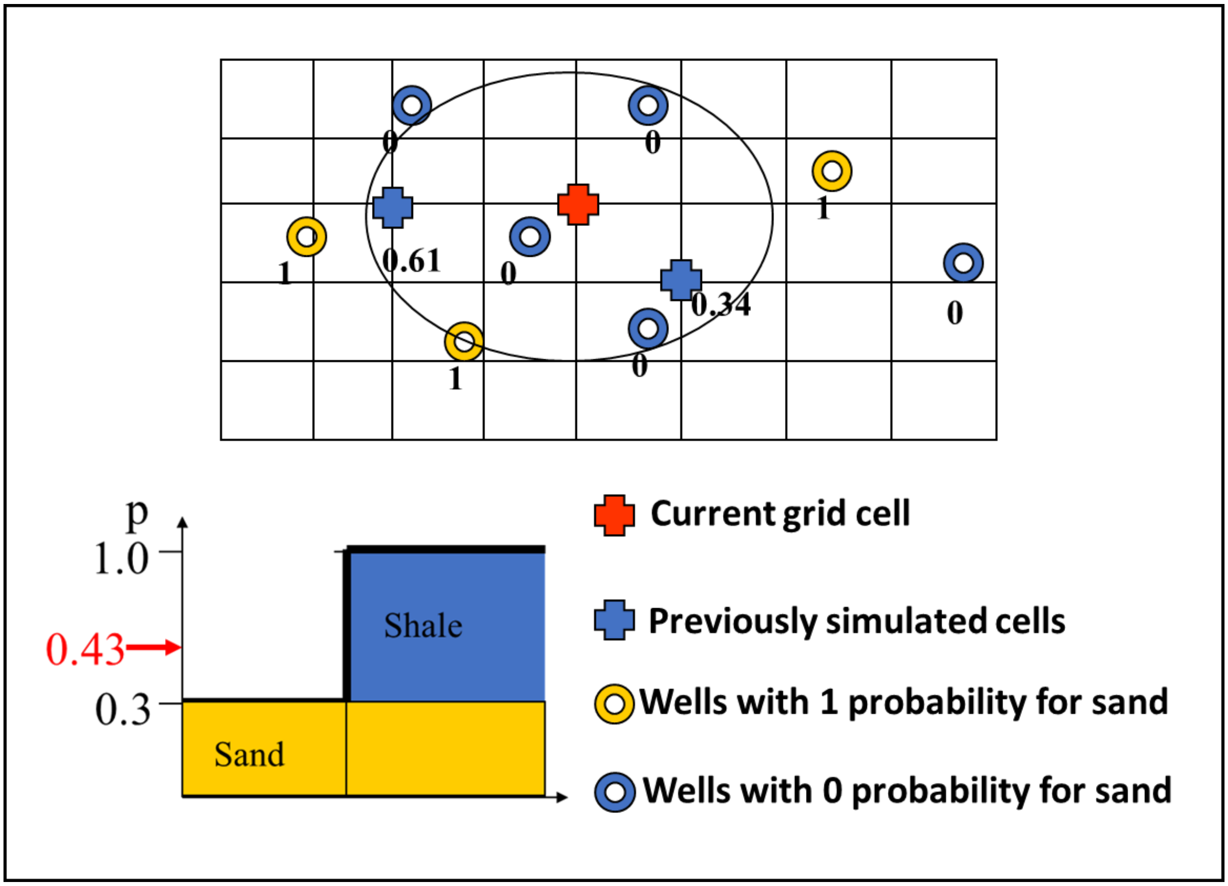

Figure 3.19 Conceptual example showing how Sequential Indicator Simulation works. Modified after Petrel Property Modelling, (2017).

Seismic data can also be used to constrain the SIS realizations. A seismic volume such as an acoustic impedance cube can be used to define spatially variable proportion trends for the different facies (Doyen, 2007). Using stochastic inversion results, a probability cube can be derived and used along SIS as follows:

$$Z(x_0) = \sum_{i=1}^{n} \omega_i \, Z(x_i) + \left[1 - \sum_{i=1}^{n} \omega_i\right] \times Probability\_Trend_{Sand}^{Global}$$

where the $Probability\_Trend_{Sand}^{Global}$ is represented by the probability cube derived from several stochastic impedance realizations.

Deterministic inversion can also be used to distribute the facies by replacing the probability cube coming from stochastic inversion with a look-up table (**Figure 3.20**). The look-up table works as followed: every cell in the model has an impedance value coming from the seismic inversion cube sampled into the 3D grid. Along the well paths the cells also have a facies value coming from the facies logs. The impedance cube is subdivided in several classes of different value ranges. For each class the facies distribution is derived from the grid cells which also have a facies log value. In this way separate facies CDFs are derived for each impedance value class. During the SIS process the global facies distribution may change from cell to cell depending on the impedance value assigned to the grid cells. In this way the impedance distribution influences the facies simulation (Petrel Property Modelling, 2017).

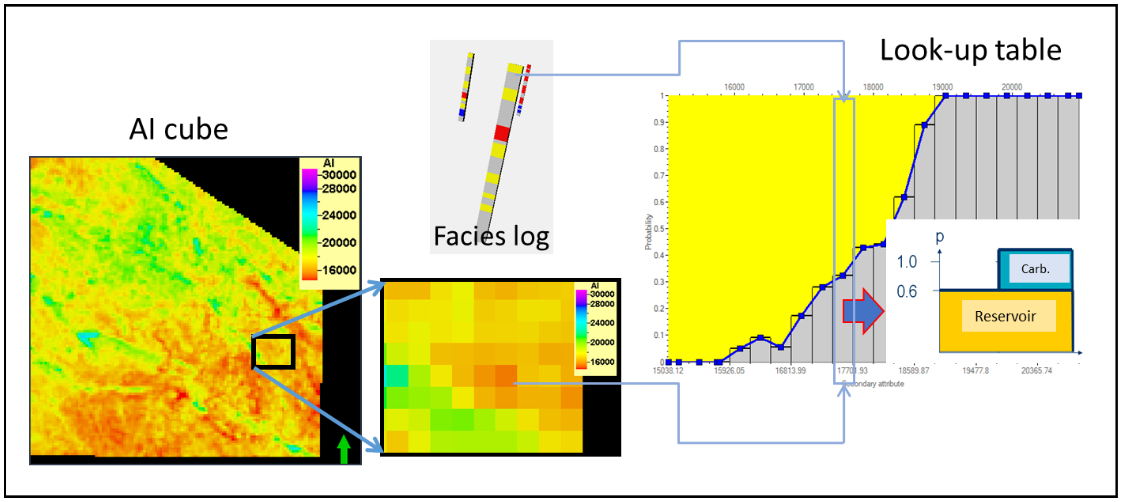

Figure 3.20: Schematic workflow describing how the look-up table works. Modified after Petrel Property Modelling, (2017).

4 Data

The data set was provided by Equinor ASA and consists of a 3D full-stack PP seismic cube, several time surfaces including the top of the reservoir, Brent Group (**Figure 4.1** and **Figure 4.2**) and 12 wells, of which 9 are related to exploration and 3 to production. Also, three of the wells are not covered by the seismic survey. The overview of the wells with the key logs is included **Table 4.1**.

The seismic survey was acquired in 2008 in block 30/9 covering an area of approximately 160 km^2, targeting the Oseberg J-area. The PP seismic data has SEG (Society of Exploration Geophysicists) polarity in which a displayed read peak means a “hard” kick which corresponds to an increase in acoustic impedance with time. The frequency range within the reservoir interval (-1800 to -2800 ms) ranges between 5-37 Hz (**Figure 4.3**) and the sample interval is 4 ms.

The software used for this Master thesis is Petrel 2018.

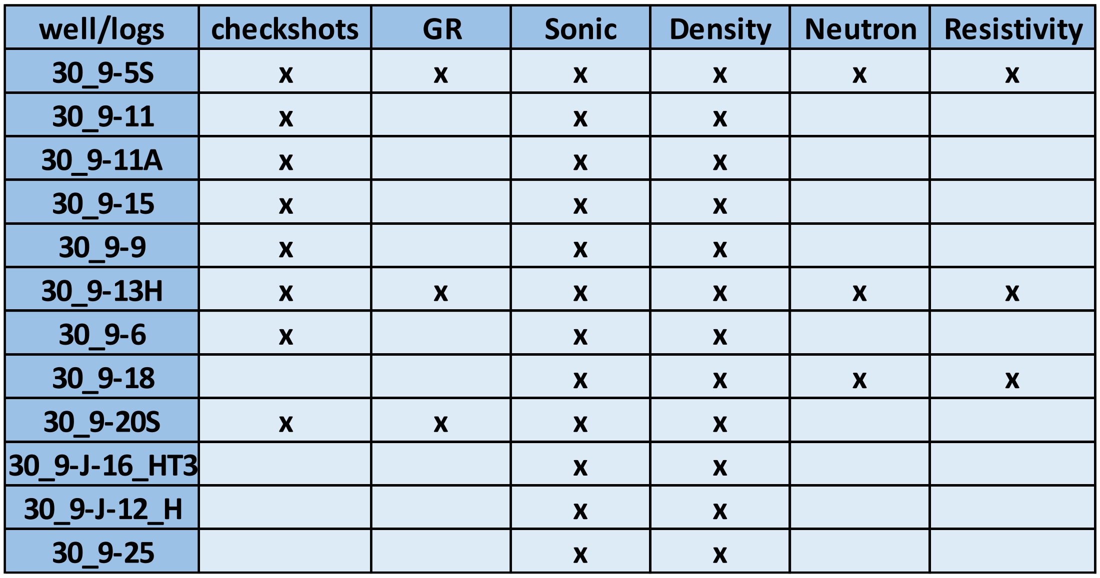

well/logs	checkshots	GR	Sonic	Density	Neutron	Resistivity
30_9-5S	x	x	x	x	x	x
30_9-11	x		x	x		
30_9-11A	x		x	x		
30_9-15	x		x	x		
30_9-9	x		x	x		
30_9-13H	x	x	x	x	x	x
30_9-6	x		x	x		
30_9-18			x	x	x	x
30_9-20S	x	x	x	x		
30_9-J-16_HT3			x	x		
30_9-J-12_H			x	x		
30_9-25			x	x		

Table 4.1 Overview of the available wells with key logs

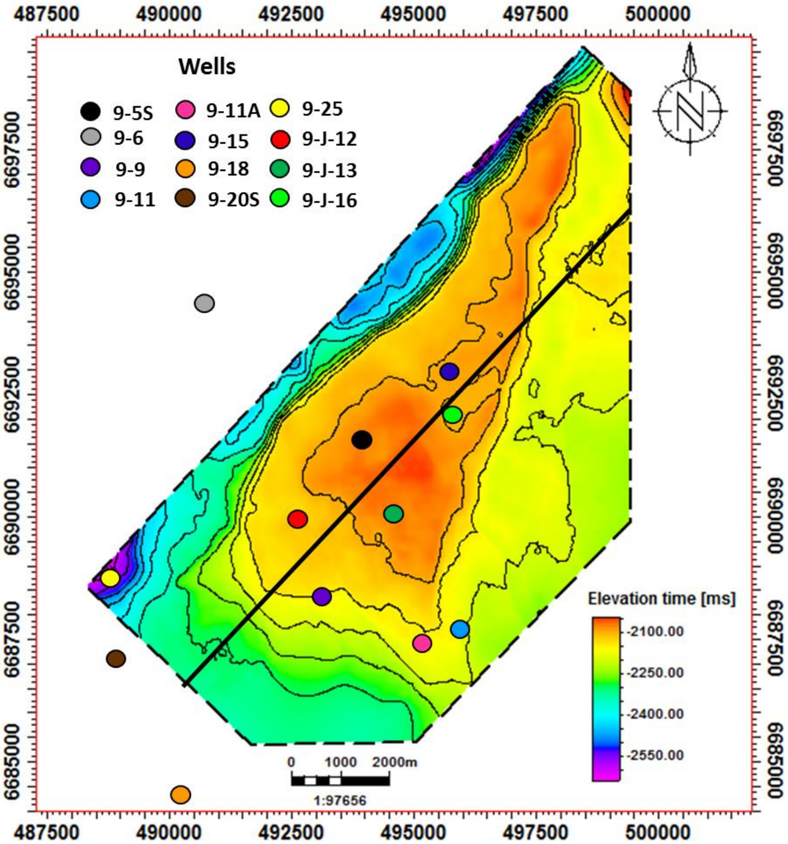

Figure 4.1:Interpretation of top reservoir (Brent Gp.) provided by Equinor ASA. Location of the wells and the cross-section shown in figure 4.2 are included in the map. Contour interval is 50ms.

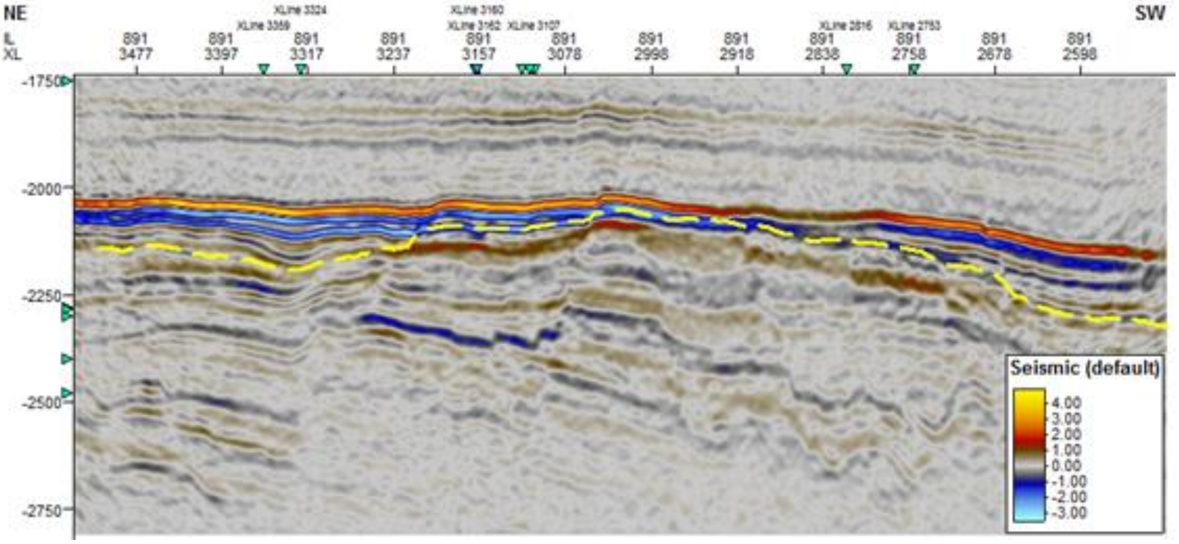

Figure 4.2: SW-NE seismic section showing the interpretation of top reservoir (Brent Gp.)

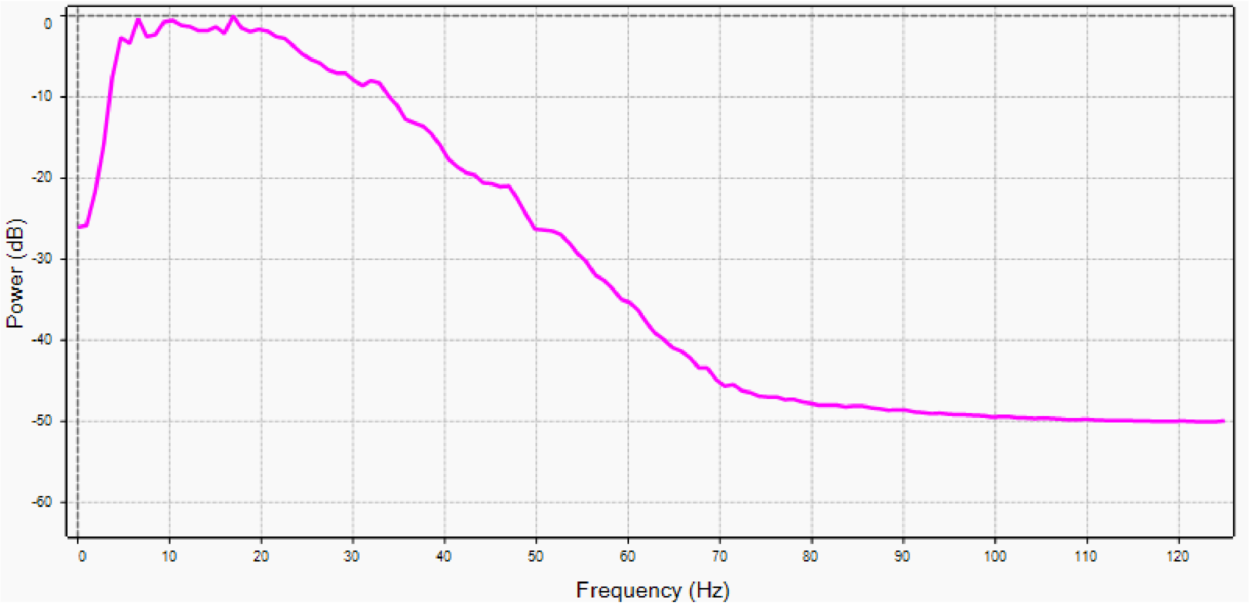

Figure 4.3: Frequency spectrum of the seismic data.

5 Methodology

The general workflow used in this study is shown in **Figure 5.1**. Firstly, a 3D model of the study area was built (section 5.1). Then deterministic seismic inversion (section 5.2) and stochastic seismic inversion (section 5.3) were conducted. The results from these processes were used alongside the well data to create facies models (section 5.4). Finally, the volumes and uncertainty coming from these facies models were calculated and compared (section 5.5).

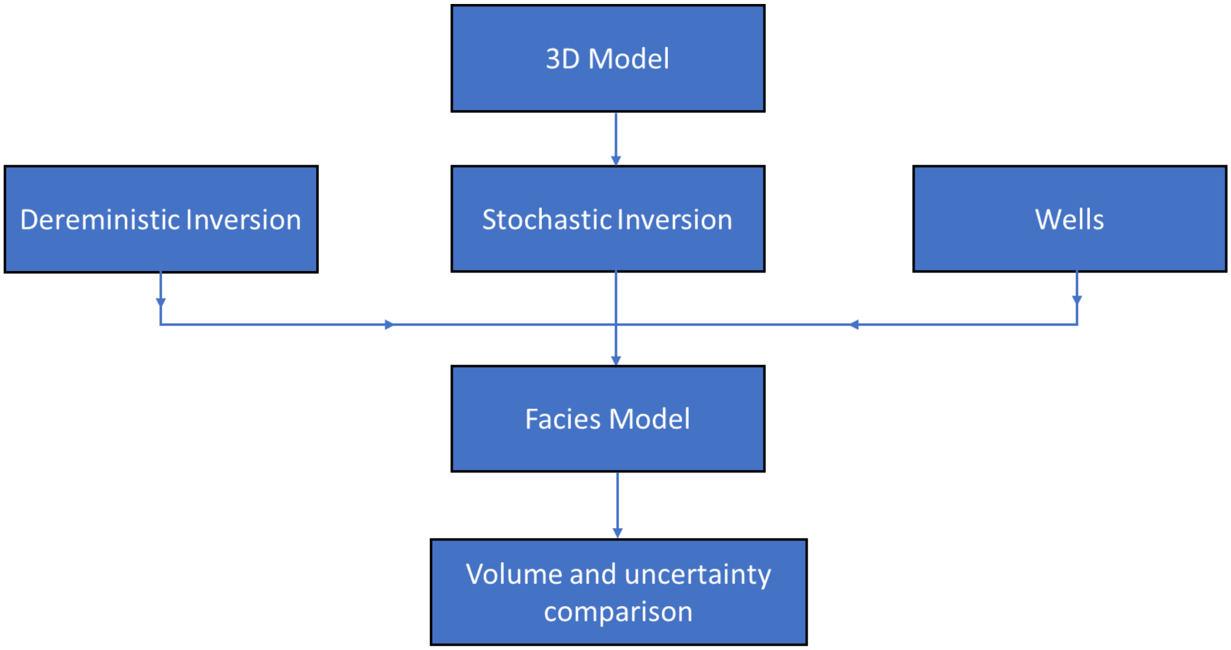

Figure 5.1: The general workflow of the main methods applied in this thesis.

5.1 3D modeling

Prior to the modeling process the study area must be identified. Therefore, based on the interpretation of the well data the reservoir zones were identified. Afterwards the outline of the reservoir was quality checked and conditioned to the well tops. Based on the horizons and the well tops a simple 3D grid was created, and the facies logs and the acoustic impedance logs upscaled (**Figure 5.2**).

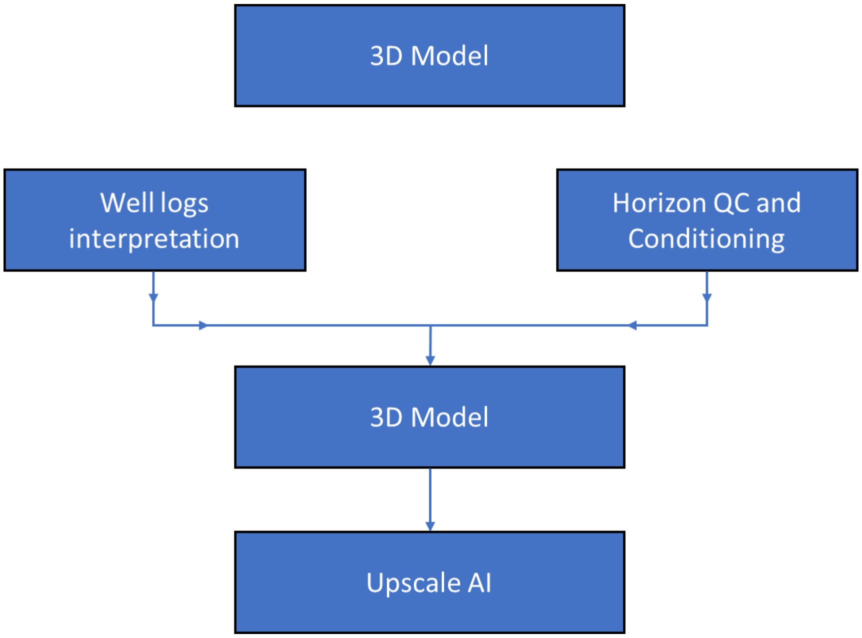

Figure 5.2: Generic workflow used for creating the 3D model

5.1.1 Well log interpretation and horizon conditioning

The reservoir zone (Brent Gp) was studied using the well data available. Based on the gamma-ray log and the neutron/density cross-over, the reservoir was identified alongside the different lithologies.

Based on the available well tops and well log interpretation, four surfaces were chosen for creating the 3D model: Shetland Gp., Brent Gp., Drake Fm. and Cook Fm. The surfaces were then cropped around the horst structure thus defining the study area.

5.1.2 Creation of the simple 3D grid

With the exception of the two major faults, the Barge Fault and the Brage East Fault, there are no major faults compartmentalizing the reservoir. Therefore, a simple 3D was created without any fault framework. The 3D model was build using four surfaces as input: Shetland Gp., Brent Gp, Drake Fm. and Cook Fm (**Figure 5.3**).

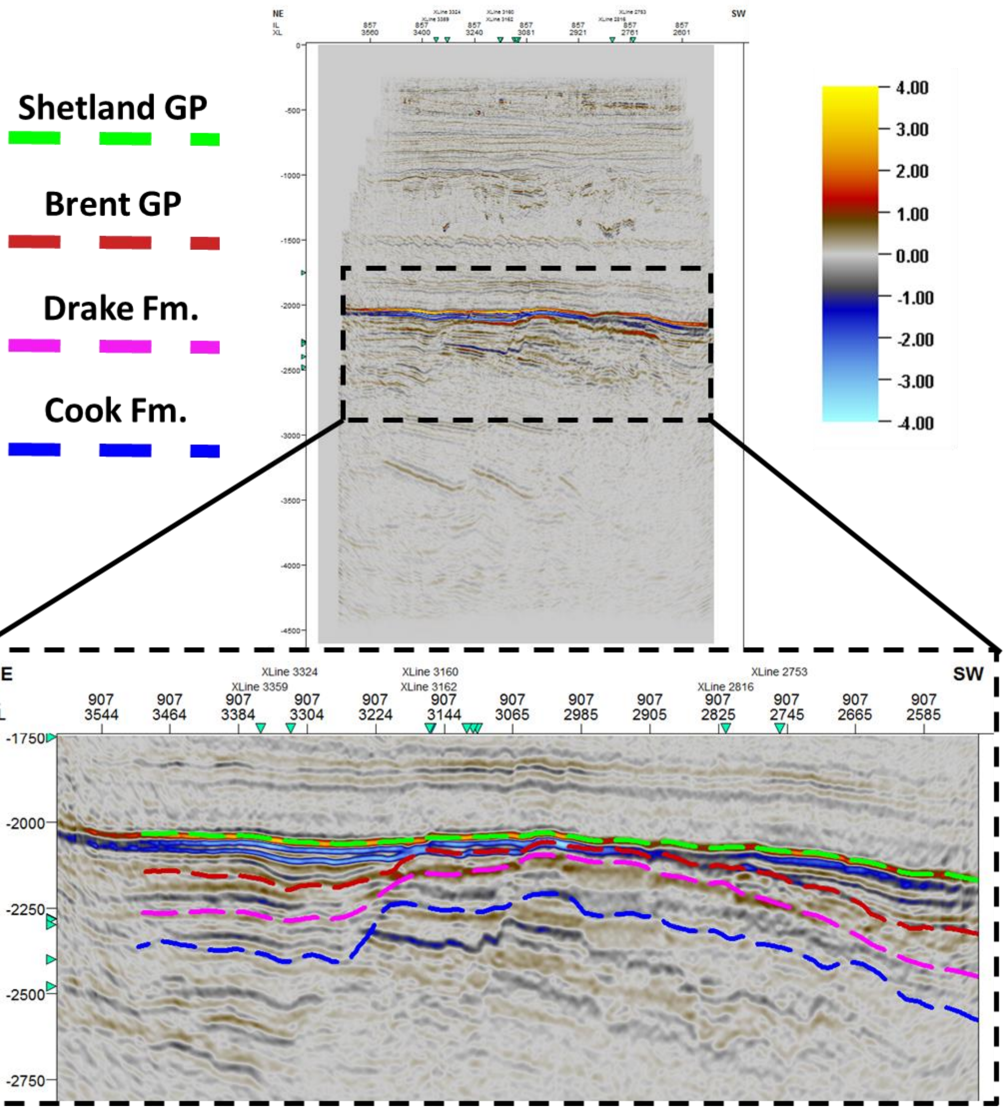

Figure 5.3: Seismic section showing the four horizons used for creating the 3D model.

The four surfaces divide the model into 3 different zones (**Figure 5.4**). The upper zone Shetland GP-Brent Gp represents the seal of the reservoir and it mainly consists of tight limestone with very low porosity. The middle zone, Brent Gp. – Drake Fm. represents the reservoir interval and it mainly consisting of sand with intercalation of shale and thin, tight limestone layers. The zone beneath the reservoir, Drake Fm – Cook Fm, mainly consists of shales.

The layering used for the model is proportional thus the upper and lower zones were divided in 40 layers while the middle one was divided in 20 layers. Lastly the acoustic impedance log has been upscaled into the 3D model. The statistics of the 3D grid are summarized in **Table 5.1**.

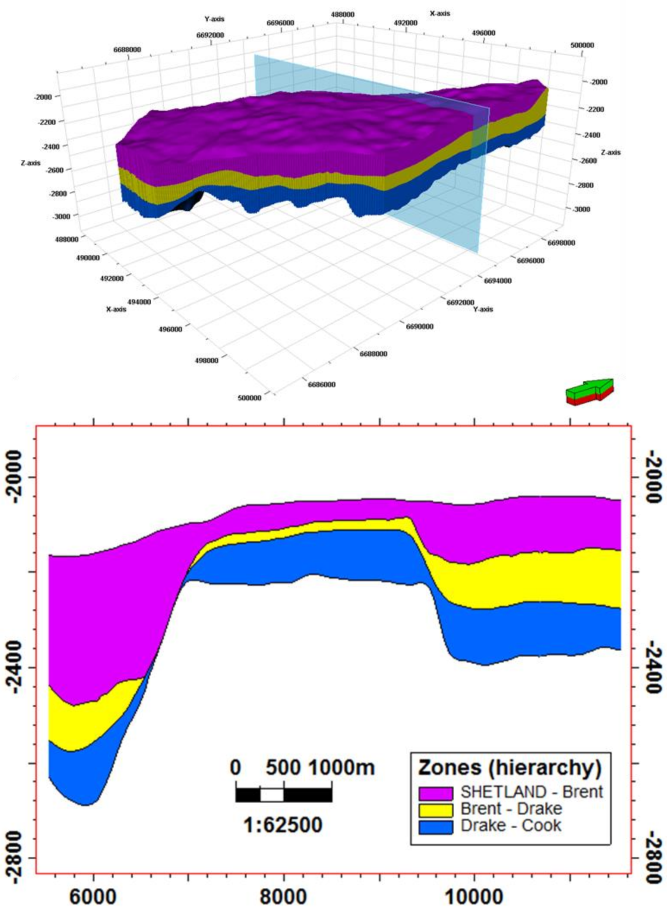

Figure 5.4: 3D model (top) and a cross-section through the model (bottom) showing the 3 different zones of the model : Shetland Gp.- Brent Gp., Brent Gp.- Drake Fm. and Drake Fm,-Cook Fm.). The navigation of the cross section is shown by the light blue plane in the upper figure.

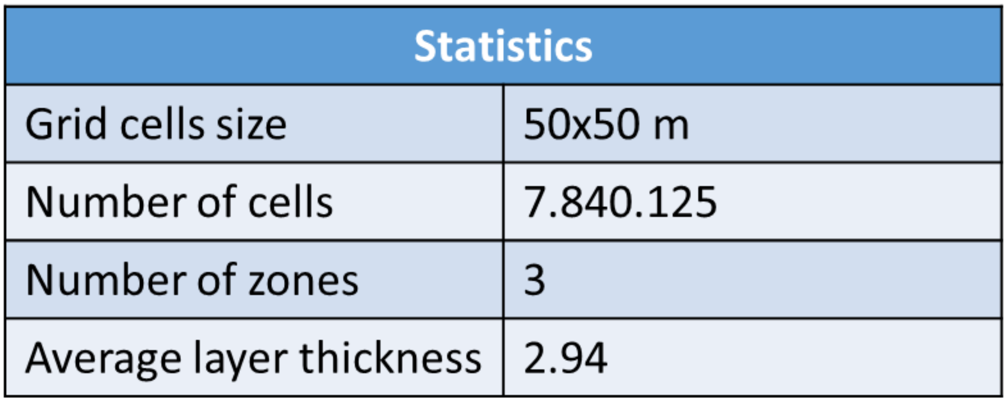

Statistics	
Grid cells size	50x50 m
Number of cells	7.840.125
Number of zones	3
Average layer thickness	2.94

Table 5.1: Statistics of the 3D Grid.

5.2 Deterministic inversion

The workflow used for deterministic inversion is shown in **Figure 5.5**. The extracted wavelet, the low frequency model, and the seismic cube serve as input parameters for the deterministic inversion. The output of this process is represented by the acoustic impedance cube, the synthetic cube, and the residual cube. In the end a quality control of the results is carried out.

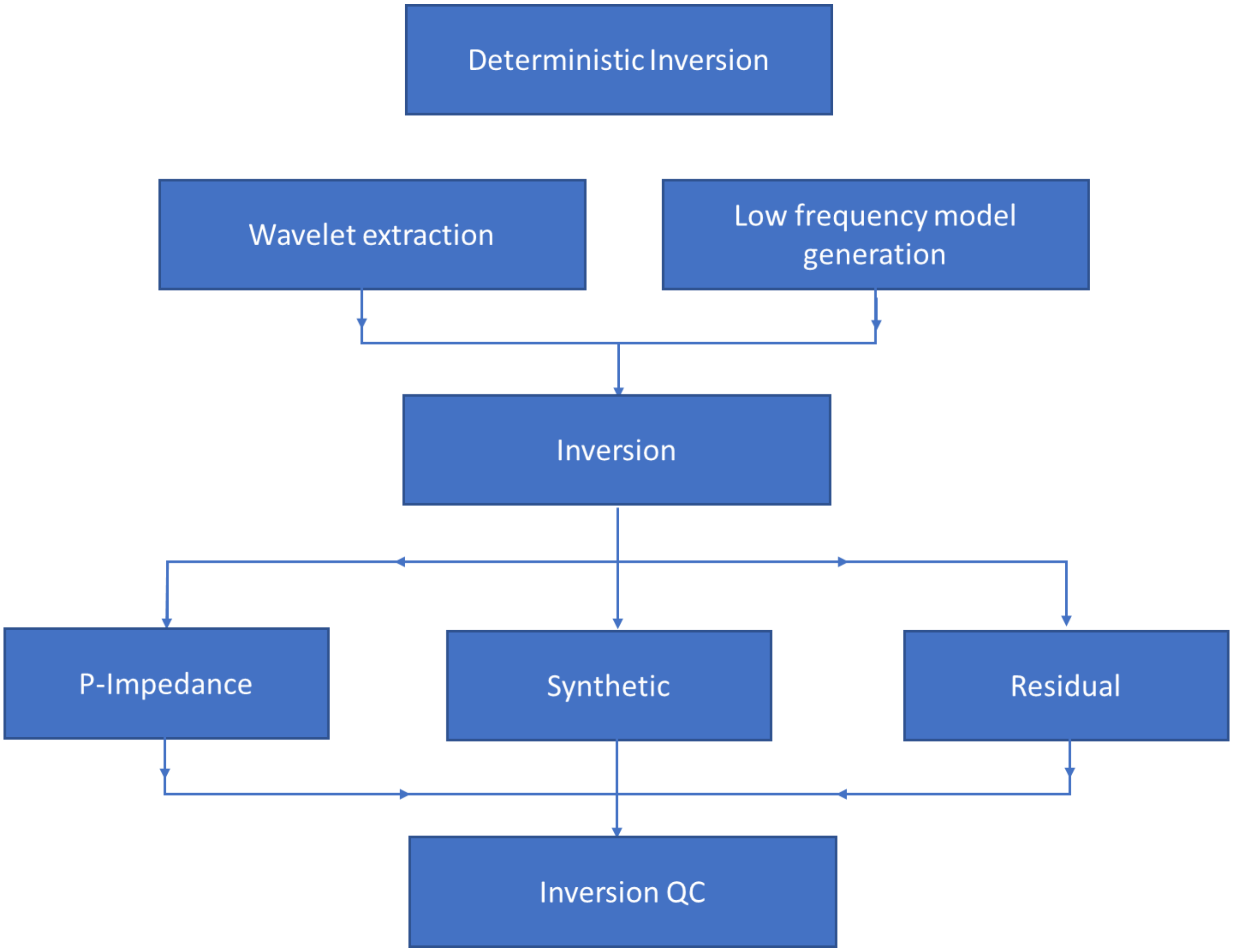

Figure 5.5: Workflow used for the deterministic inversion

5.2.1 Wavelet Extraction

The first step in the inversion process is the integration of the log data and seismic traces at the well locations. Within the study area, 9 of the 12 wells were drilled in the reservoir. They have sonic and density logs that allow correlating the well data with the seismic data. Reflectivity series and synthetic seismograms were generated from these well logs and used for performing the seismic-to-well tie thus updating the time-depth relationships and estimating a wavelet from the seismic data.

The following wavelets based on different extraction methods were used: analytical, statistical, deterministic. In order to check which wavelet gives the best result several hundred deterministic inversions were made and a quality control of the results was carried out.

5.2.2 Low frequency model

Because of the limited bandwidth nature of the seismic, the missing low frequencies were provided by the low frequency model (LFM) (**Figure 5.6**). Using the seismic cube, the geometry of the LFM was determined. Next the acoustic impedance log was extrapolated and guided through the volume by the top (Brent Gp) and base (Drake Fm.) horizons. Finally, a high-cut filter of 5 Hz was applied to the well data, which is the lowest frequency contained by the seismic.

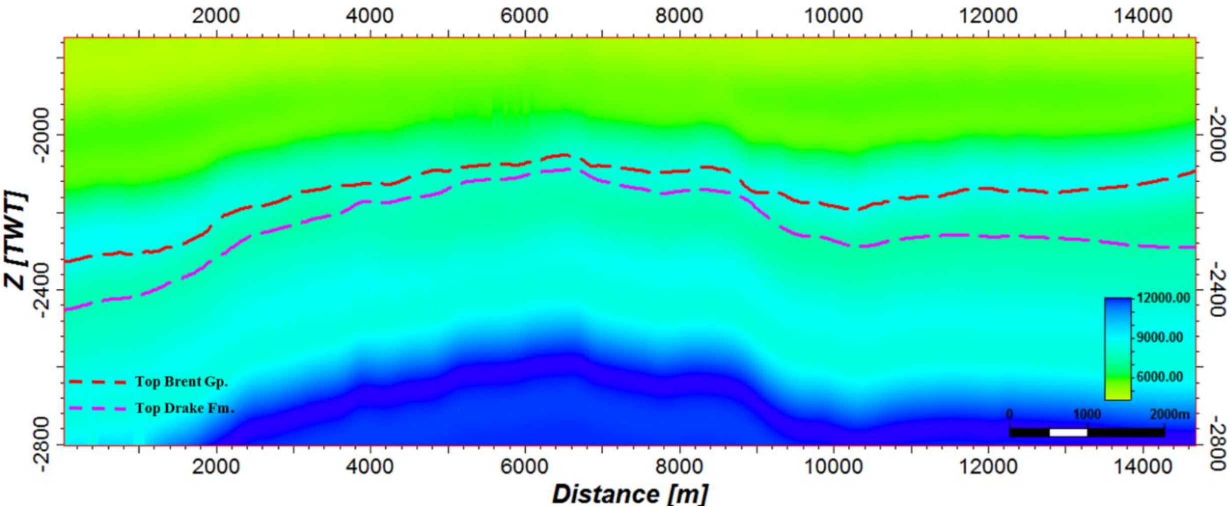

Figure 5.6: LFM of the acoustic impedance generated from well data to provide the missing low frequencies of the seismic data. The guiding horizons top Bren Gp. (red) and top Drake(purple) are highlighted in the section.

5.2.3 Inversion

The input for the deterministic inversion is represented by the extracted wavelet, the LFM and the seismic cube. The results of the inversion are a P-impedance, a synthetic and a residual cube.

5.2.4 Inversion QC

Two methods were used to quality control (QC) the inversion results. The first one is the comparison of the synthetic cube with the seismic cube which delivers the residual cube. The percentage of misfit between the synthetic and the seismic cube was analyzed and the result with a misfit higher than 4% were disregarded (**Figure 5.7**).

The second method used to QC the results is to compare the modeled acoustic impedance with the acoustic impedance log at the well location.

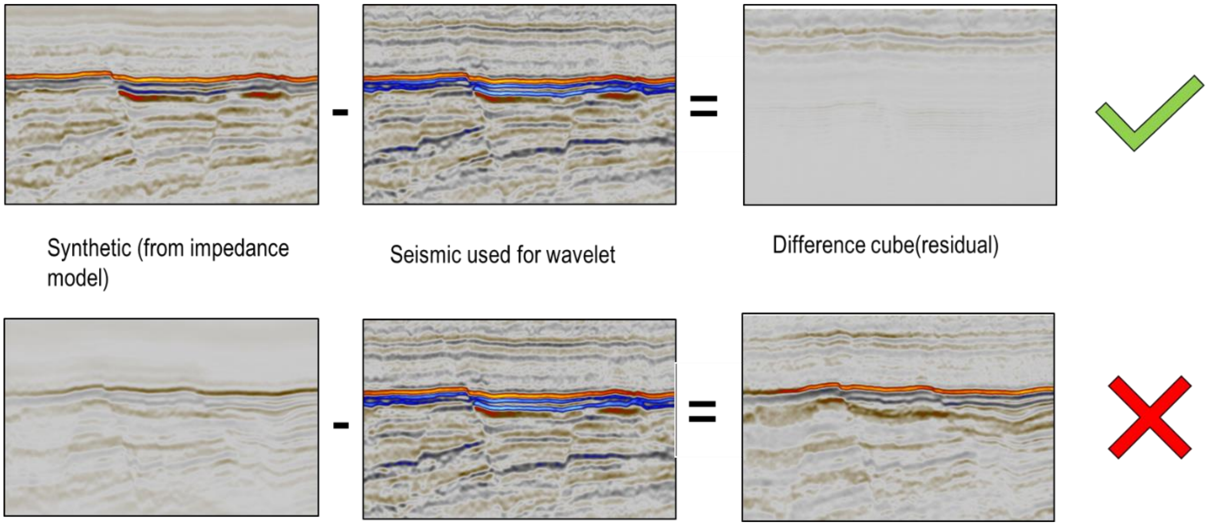

Figure 5.7: Quality checking the residual cube

5.3 Stochastic inversion

The proposed workflow for stochastic inversion is illustrated in **Figure 5.8**.

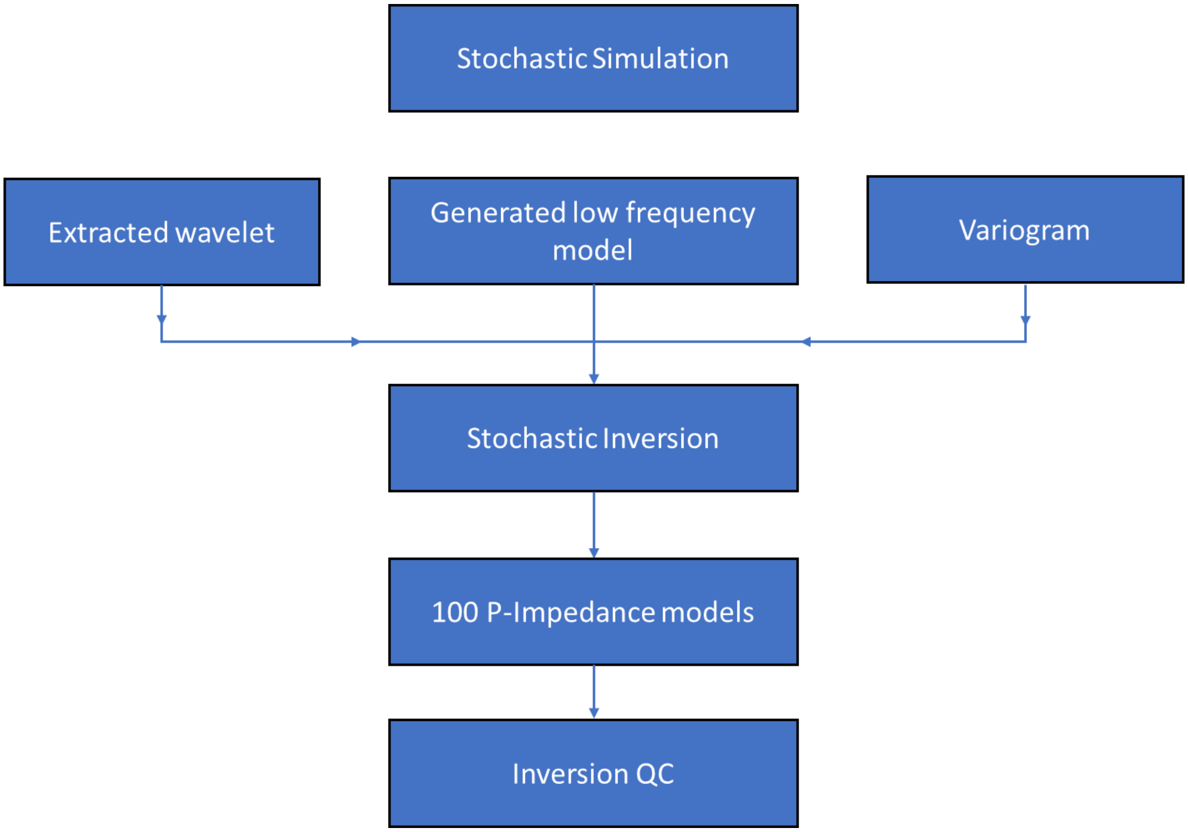

Figure 5.8: Generic workflow used for stochastic inversion

5.3.1 Variogram

The variogram is an important parameter controlling the distribution of the high-resolution information provided by the upscaled acoustic impedance log. The vertical variogram was set up from the well data (**Figure 5.9a**). Unfortunately, the limited number of wells does not allow to derive a reliable horizontal variogram. Therefore, the horizontal variograms model was derived from the deterministic inversion (**Figure 5.9b**, **5.9c**) which shows a high correlation with the acoustic impedance logs of the wells. In order to address a possible anisotropy, an analysis of the horizontal variogram extracted for different azimuths allowed to derive the variogram value for the major and minor horizontal ranges.

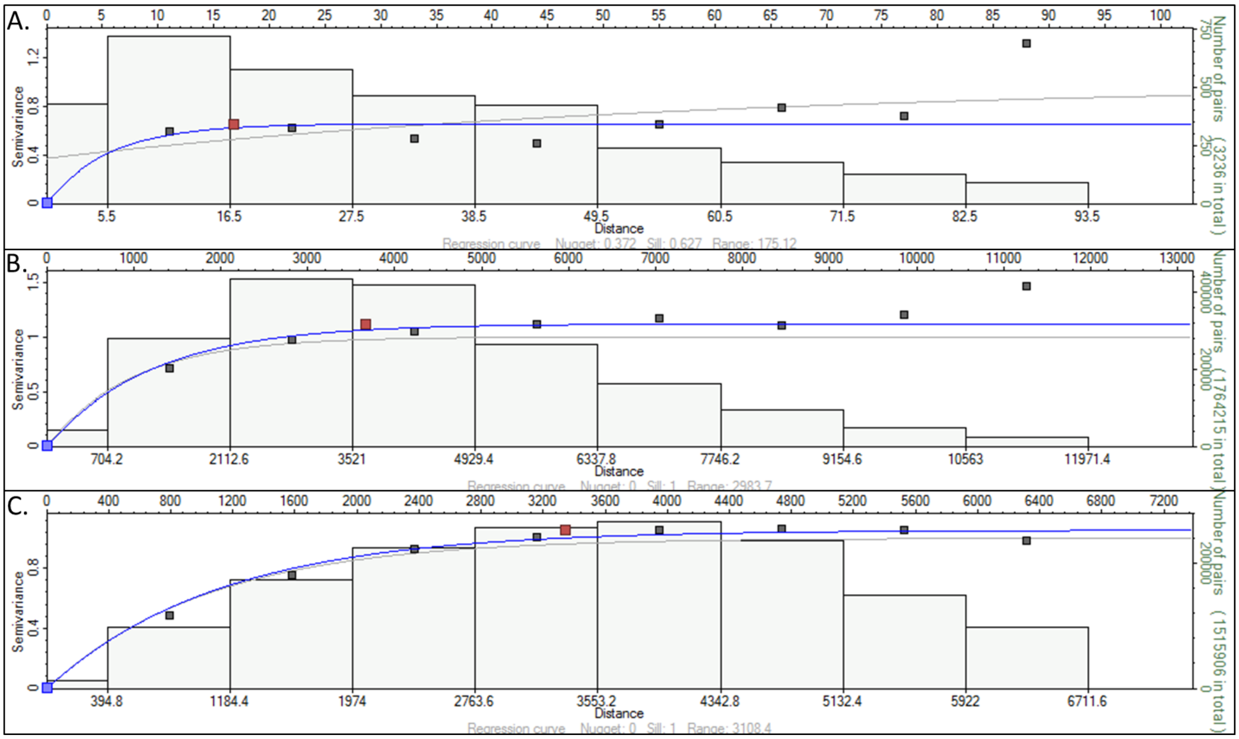

Figure 5.9: Exponential variograms used for stochastic inversion. A. Vertical variogram extracted from the well data. B. Horizontal minor range variogram extracted from deterministic inversion. C. Horizontal major range variogram extracted from deterministic inversion.

5.3.2 Stochastic inversion

100 stochastic inversion were generated for each wavelet. The same wavelets and LFM used for the deterministic inversion serve as input for stochastic inversion alongside with the upscaled acoustic impedance log, the seismic and the variogram. The output is represented by multiple acoustic impedance cubes.

5.3.3 Inversion QC

There are two ways of checking the results coming from the stochastic simulation. First the diagnostics of the results are reviewed. The diagnostic tools are the cost function, the number of iterations needed for achieving a correlation between the synthetic and the seismic above the user threshold value for each trace, and the Boolean function labeling whether an inversion trace has a cost function above its threshold value. If the cost function values are above the 0.8 threshold, the result is considered as reliable. If the number of iterations is low, then the inversion process was able to fit the data easily. In areas where the cost function is low, the number of iterations is usually maximum.

5.4 Facies Modeling

This chapter describes the methods used for the facies modeling. The workflow is illustrated in **Figure 5.10**. First the acoustic impedance cube coming from deterministic inversion was upscaled into the 3D grid. Afterward a facies log was made from the acoustic impedance log and sampled into the 3D grid. Based on the results from the deterministic and stochastic inversion probability cubes were generated and used for guiding the facies simulation. In addition, facies modeling based solely on well data was set up.

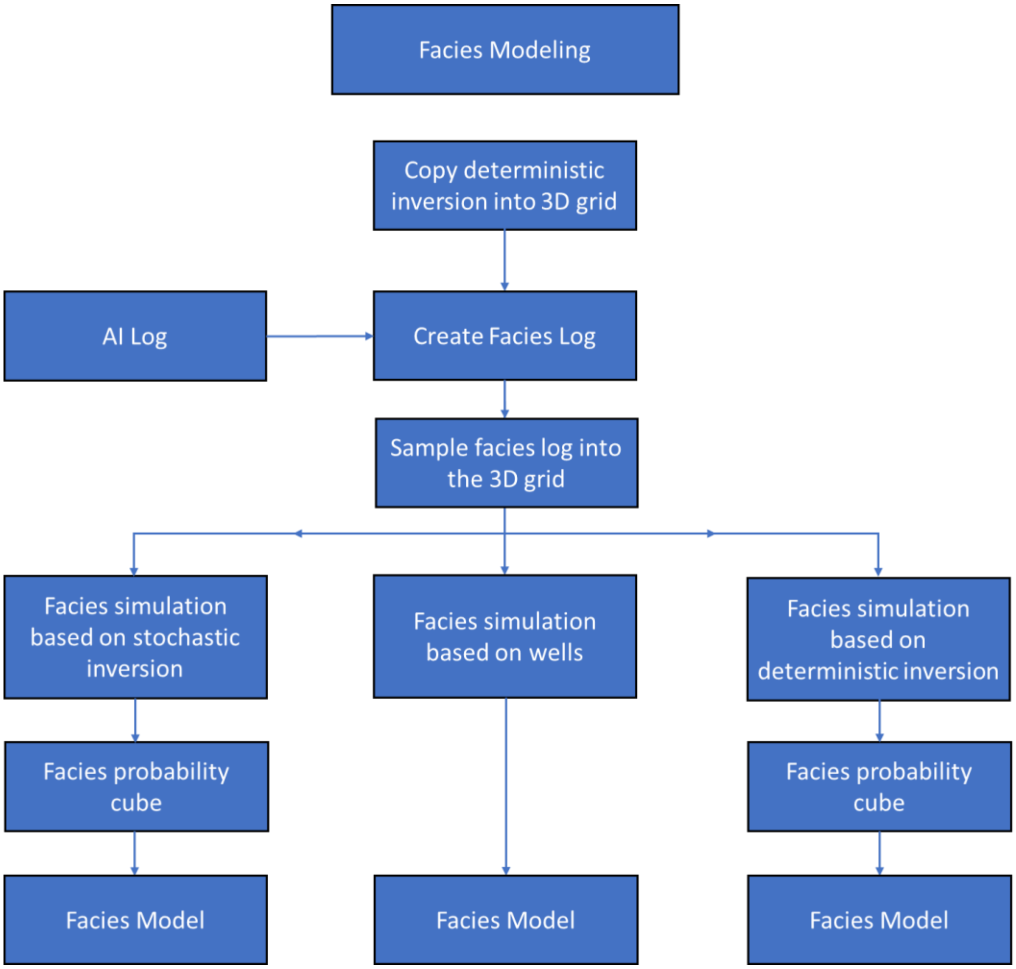

Figure 5.10: Generic workflow used for facies modeling

5.4.1 Facies log

Initially a facies log was build using the well logs gamma ray, acoustic impedance and porosity. Three different facies were distinguished: sandstone, shale and limestone. However, after plotting the acoustic impedance versus the seismic impedance and color coding the results using the facies log (**Figure 5.11**), it became obvious that the acoustic impedance does not allow to differentiate between sand and shale. Therefore, a new facies log was built based on a cut-off of the acoustic impedance. The acoustic impedance values higher than 9000 kPa.s/m were assigned to limestone and all values smaller than 9000 kPa.s/m were assigned to siliciclastic.

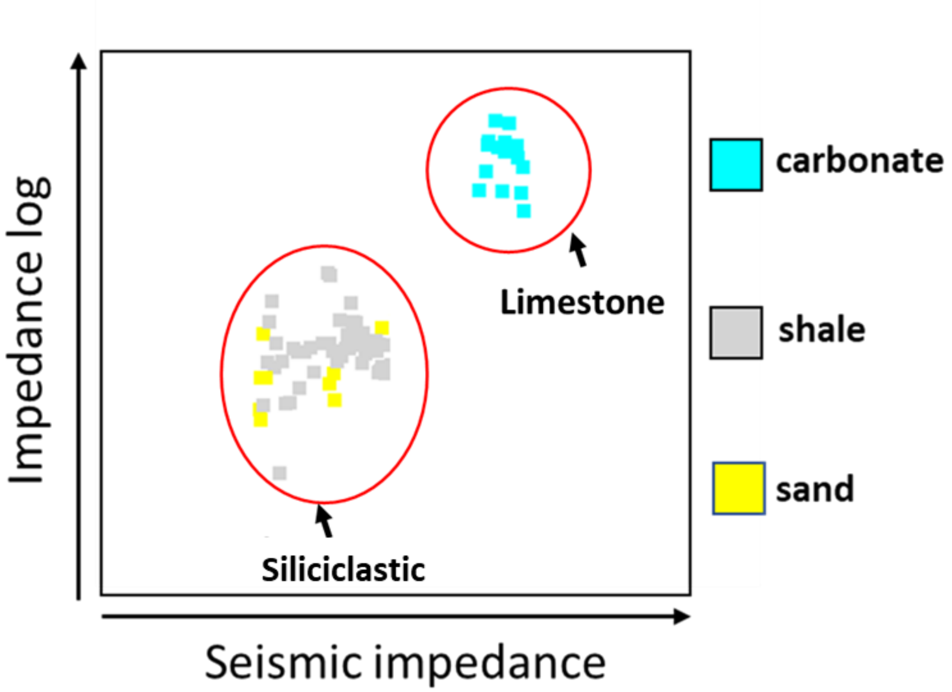

Figure 5.11: Crossplot between the seismic impedance and the impedance log color coded by the facies log.

5.4.2 Facies simulation based on deterministic inversion

For guiding the facies using deterministic inversion, the look-up table was used for each model zone. The algorithm used for the modeling is Sequential Indicator Simulation (SIS). The variogram parameters used for stochastic inversion were also used for distributing the facies.

5.4.3 Facies simulation based on stochastic inversion

For guiding the facies using stochastic inversion, a probability cube for the carbonate was built based on 100 stochastic impedance realizations. Using the same cut-off of the acoustic impedance as the one used for building the facies log the stochastic inversion cubes were converted into carbonate probability cubes thru simply assigning ‘one’ to carbonate and ‘zero’ to siliciclastic. The final probability cube for carbonate followed through simply averaging the individual probability cubes. The algorithm used for the modeling was SIS (see section 3.5) and the variogram parameters used for guiding the facies were the same ones that served as input for the stochastic inversion.

5.5 Volume calculation

The 3D Model was depth converted. A script (Petrel workflow) was set up for the calculation of 200 facies models using deterministic inversion, stochastic inversion and well data only. The script allowed deriving the carbonate volume (**Figure 5.12**).

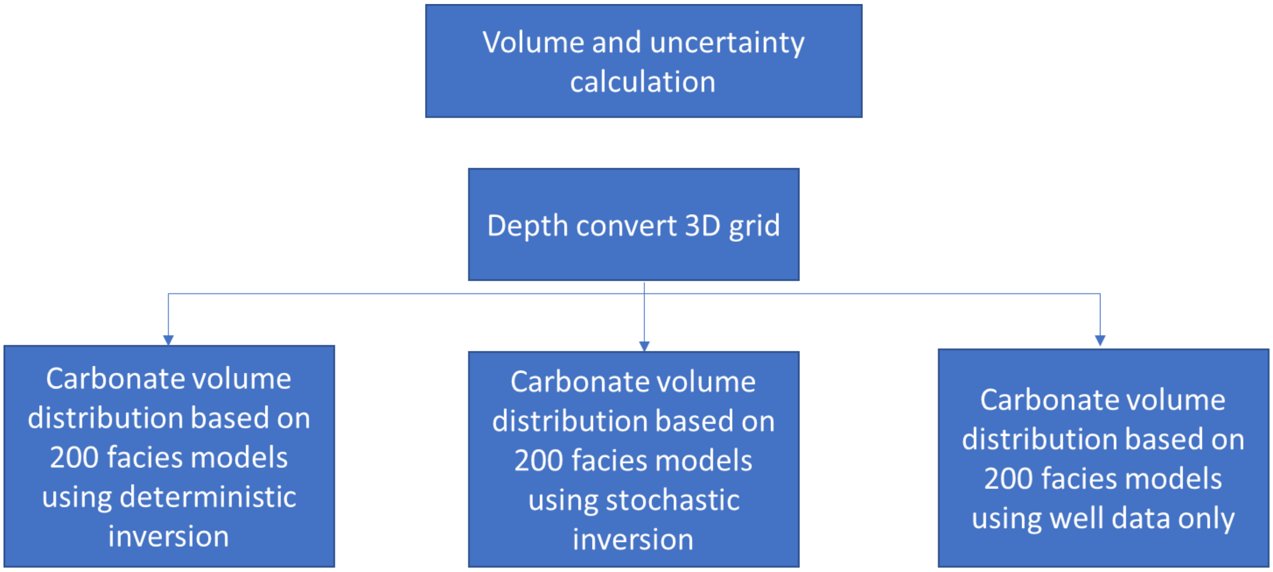

Figure 5.12:Generic workflow used for volume and uncertainty calculation.

5.5.1 Depth conversion of 3D grid

A velocity model was built for converting the 3D Grid from time to depth. The model was based on a PSDM seismic velocity cube provided by Equinor. The model uses the same surfaces used for creating the 3D grid. The well tops linked to the seismic surfaces were applied to the velocity model to adjust the seismic velocities to the wells.

5.5.2 Volume and uncertainty calculation

A workflow was made for creating 200 facies models based on the deterministic inversion, stochastic inversion and well data only. Gross rock volumes for carbonate were derived for each model. The P10, P50 and P90 volumes and their corresponding models were then identified.

6 Results

This chapter summarizes the results of the thesis. Section 6.1 covers the well log interpretation in the reservoir zone and the building of the 3D model. Section 6.2 describes the results of the deterministic inversion. Section 6.3 covers the results of stochastic inversion while section 6.4 presents the volumes calculated solely based on well data.

6.1 3D Modeling

6.1.1 Well log interpretation and horizon QC and conditioning

This thesis focuses on the main reservoir zone represented by the Brent Gp around the horst structure between the Brage and The Brage East faults (**Figure 6.1**).

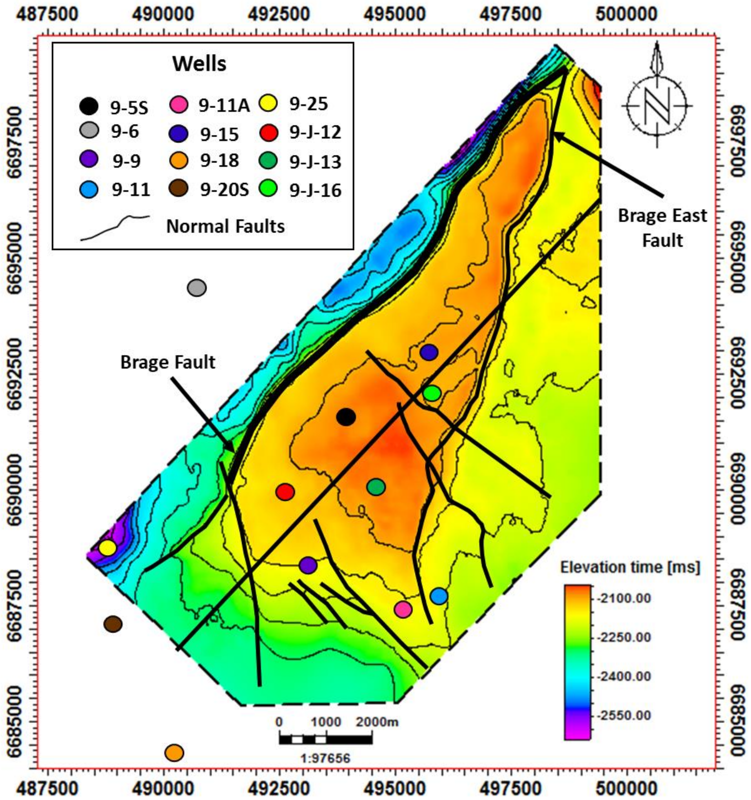

Figure 6.1: Top of reservoir (Brent Gp.) time surface showing the location of the wells and the interpreted faults. The contour interval is 50 ms.

Well 30/9-J-13 was used for identifying the reservoir zones and for interpreting lithology along the Shetland Gp and the complete Brent Gp **(Figure 6.2)**. The limestone was identified based on the high acoustic impedance value and low gamma-ray and porosity values. The shale was interpreted based on the high GR values and a positive separation in the neutron porosity/density (Nphi/Rhob). Finally, the sandstone was identified based on a negative separation in the Nphi/Rhob and intermediate to low GR values. Based on the large negative cross-over between the Nphi and Rhob logs several reservoir zones were identified within the Brent Gp. Also, thin carbonate layers with low porosities were identified along the Brent Gp which can act as baffle zone within the reservoir.

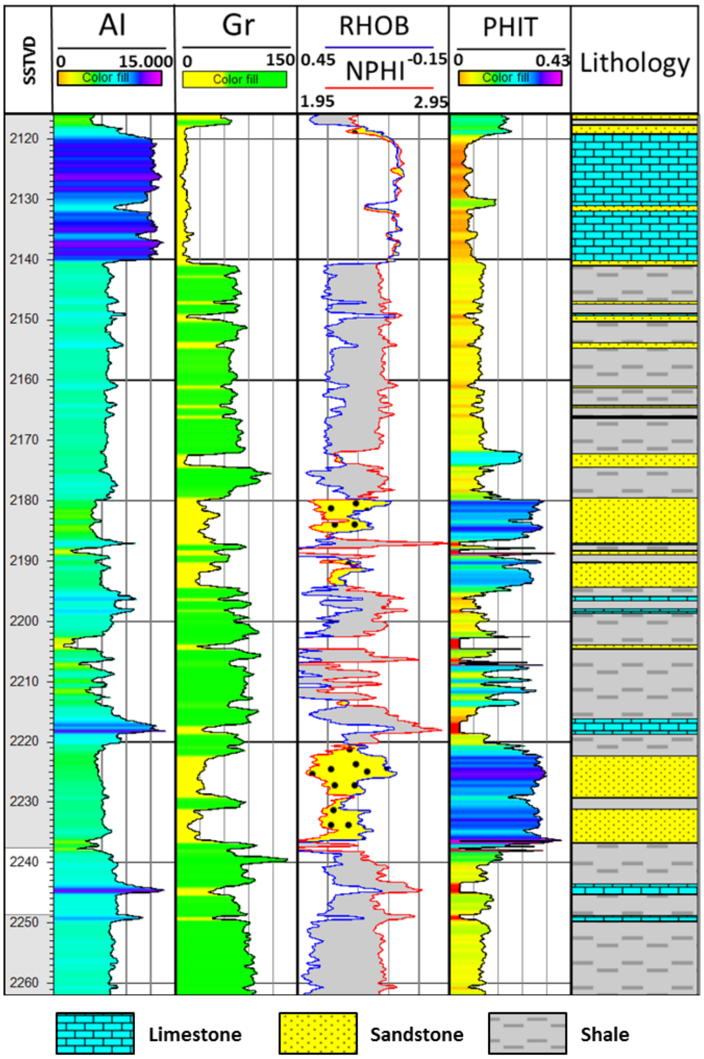

Figure 6.2: Well section for well 30/9-j-13. From left to right: SSTVD axis, acoustic impedance (AI) log, gamma-ray (Gr) log, neutron/density (Nphi/Rhob) log, porosity (PHIT) log and interpreted lithology. See Figure 6.1 for the well location.

6.2 Deterministic inversion

6.2.1 Wavelet extraction

Three different algorithms for extracting the wavelet were applied to the data of the wells drilled within the horst structure. As mentioned in Section 5.2.1 in order to test which wavelet is gives the best result deterministic inversion was performed on a predefined set of inlines.

The importance of the wavelet is shown in **Figure 6.3** where different wavelet extraction algorithms were used for the well 30/9-5S. The Extended White wavelet extracted for this well gives a smooth result with low resolution regarding the acoustic impedance. The residual cube shows several strong reflectors thus indicating an unreliable acoustic impedance. The statistical wavelet gives better results with some variation and increased resolution in the acoustic impedance, and the reflectors present in the residual cube are very weak. The best result is given by the Isis Frequency wavelet with a misfit between the seismic and the synthetic below 4%.

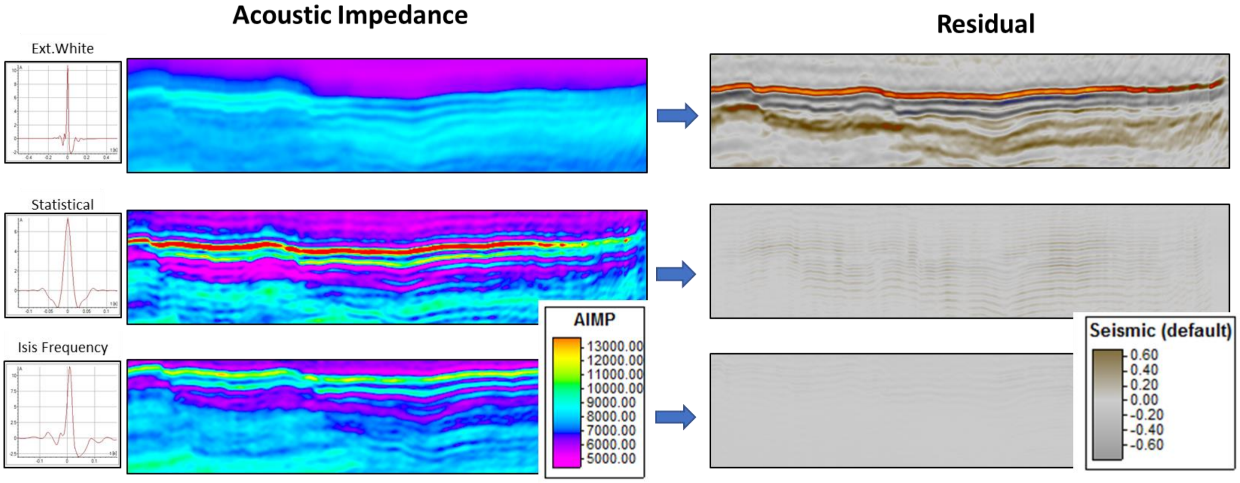

Figure 6.3: The influence of the wavelet on the inversion results. From left to right: three different wavelets, acoustic impedance sections and residual sections.

Therefore, after testing numerous wavelets derived from the reservoir wells, the best results were delivered by the following four wavelets: 13J Isis Frequency wavelet, 5S Isis Frequency wavelet coming from two different wells (30/9-**5S** and 30/9-**J-13**), Extended White wavelet derived from well 30/9-J-13, and finally a Statistical wavelet from well 30/9-5S (**Figure 6.4**). Because all these wavelets produced similar results, all of them were used for guiding the facies and calculating the volumes.

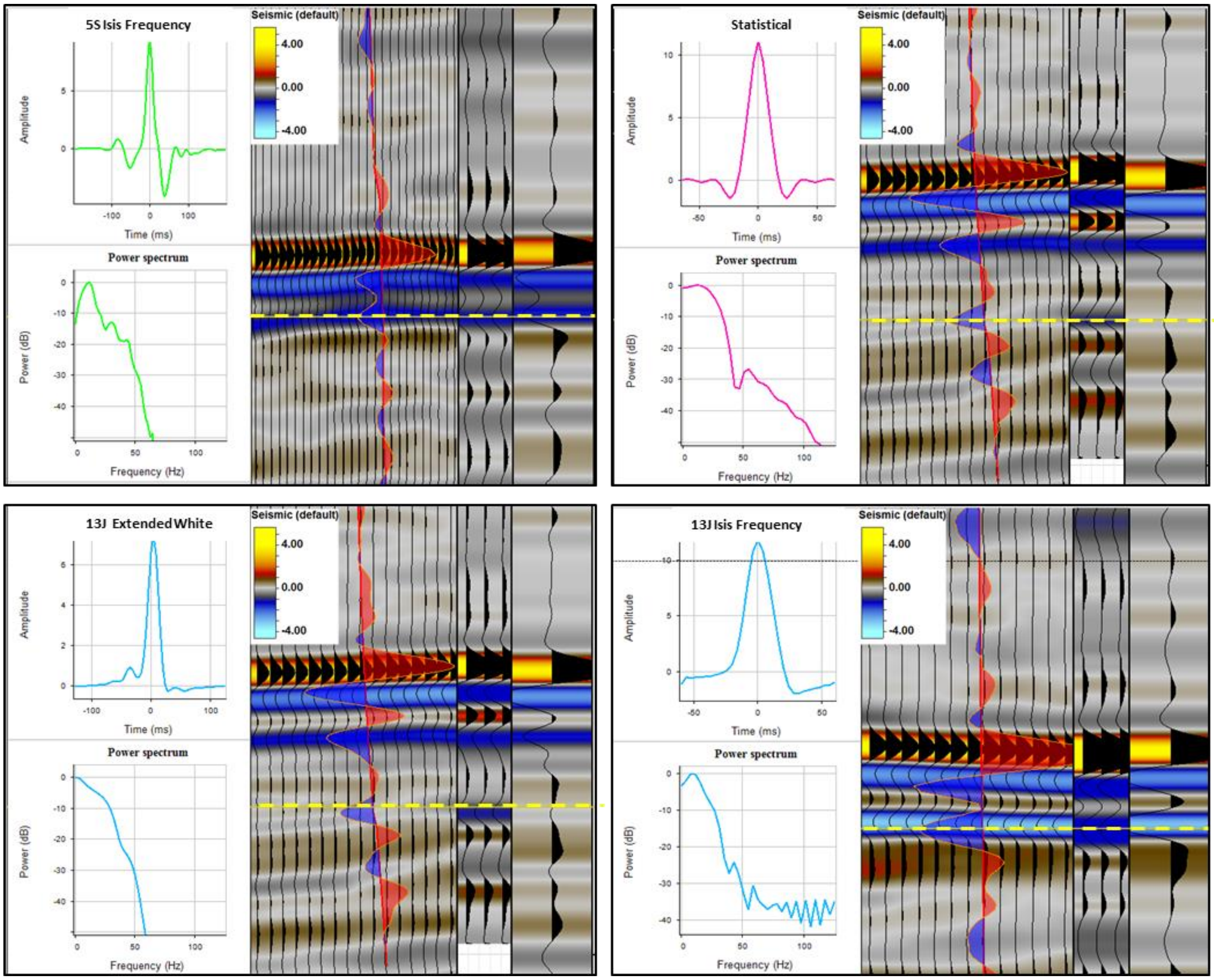

Figure 6.4: The four different wavelets which provided the best inversion results alongside the seismic well tie. Interpretation of top reservoir (Brent Gp) displayed with yellow dashed lines.

6.2.2 Inversion

The four wavelets previously shown together with the LFM and the seismic serve as input for the deterministic inversion. The output of this process consists of an acoustic impedance cube, a synthetic cube and a residual cube.

The acoustic impedance simulations from each wavelet are shown in **Figure 6.5**where the top of reservoir (Brent Gp.) is marked by a red dashed line while the base of the reservoir (Drake Fm.) is marked by a dashed purple line**.**

Figure 6.5A shows the results of deterministic inversion from the 13J Isis Frequency wavelet together with a zoomed in section at the reservoir interval. Above the reservoir, the Shetland Gp. is marked by high acoustic impedance values above 12000 kPa.s/m., represented by the purple color. These values indicate the presence of the tight limestone which is sealing the reservoir. However, within the reservoir interval, the acoustic impedance values vary between 5000 to 8000 kPa.s/m, which according to the facies log (see section 5.5.1) indicates the presence of siliciclastic sediments (sand and shale). Furthermore, the acoustic impedance response shows poor variability both horizontally and vertically.

Figure 6.5B shows the results of the deterministic inversion from wavelet 5S Isis Frequency. **Figure 6.5C** and **6.5 D** represent the acoustic impedance sections from the Statistical and the 13J Extended White wavelet, respectively. These results are similar to the ones from the 13J Isis Frequency wavelet. They all show a gradual increase of acoustic impedance with depth due to compaction. Furthermore, all the simulations capture the seal of the reservoir interval (Shetland Gp.) showing some variability in the amplitudes of this interval. Overall within the reservoir interval there is no high acoustic impedance values above 9000 kPa.s/m with most of the values ranging between 5000 to 8000 kPa.s/m.

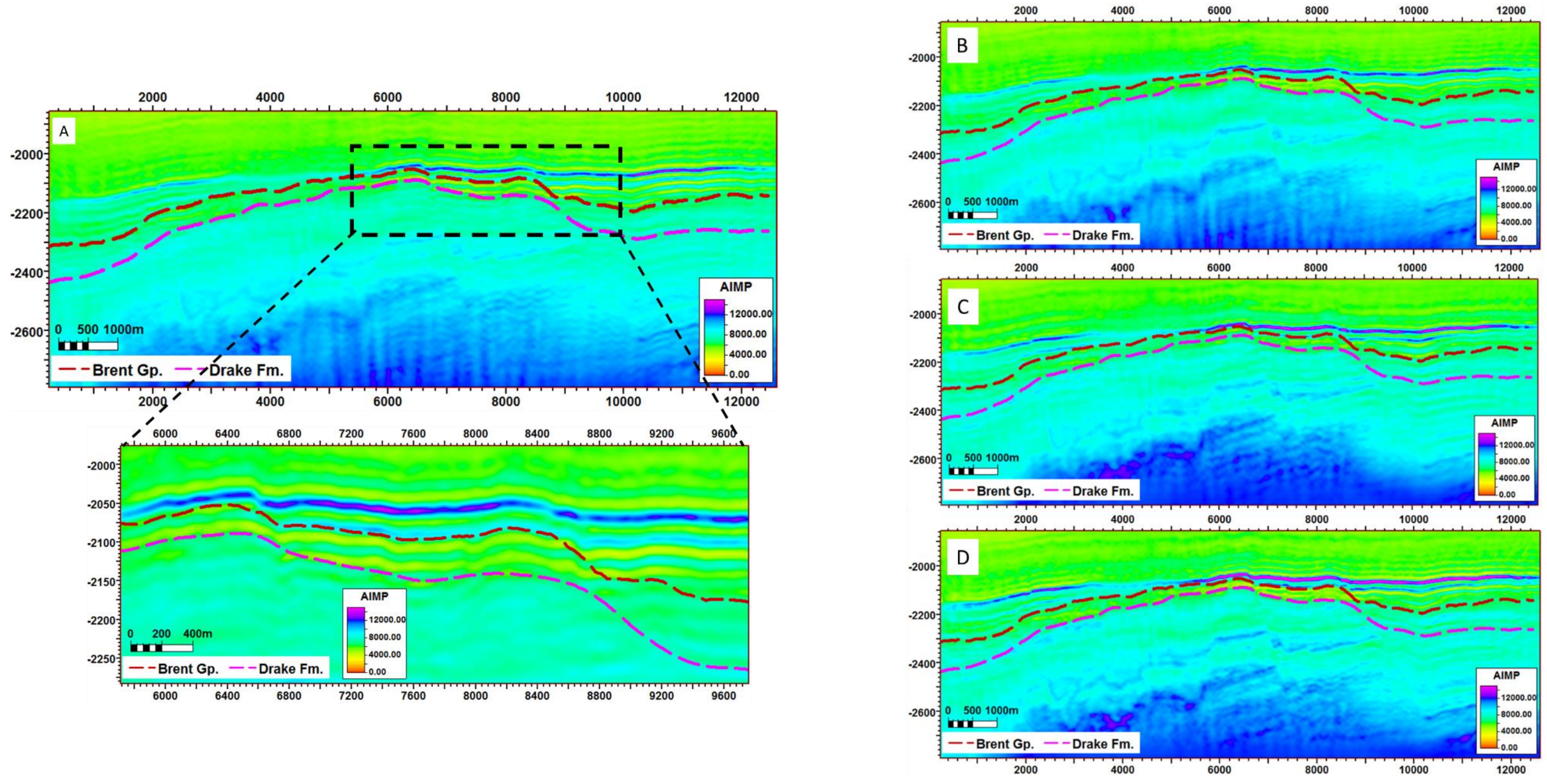

Figure 6.5 Acoustic impedance section coming from deterministic inversion using: A. 13J Isis Frequency, B. 5S Isis Frequency , C. Statistical and D. 13J Extended White. Top and base of the reservoir (Brent Gp. and Drake Fm.) are illustrated with red and purple dashed lines, respectively.

6.2.3 Inversion QC

As mentioned in section 5.2.4, two ways of quality checking the inversion results were used. Firstly, the residual cube was checked and then the synthetic seismic coming from each simulation was compared with the real seismic.

Figure 6.6 shows a seismic section alongside a synthetic seismic section from the deterministic inversion using the wavelet 13J Isis Frequency wavelet, and their difference (residual). The seismic response from the deterministic inversion shows a good correlation with the original seismic and the relative misfit between the two is lower than 3%. The inversions based on the other wavelets show similar results with a good correlation with the original seismic and a relative misfit not higher than 4%.

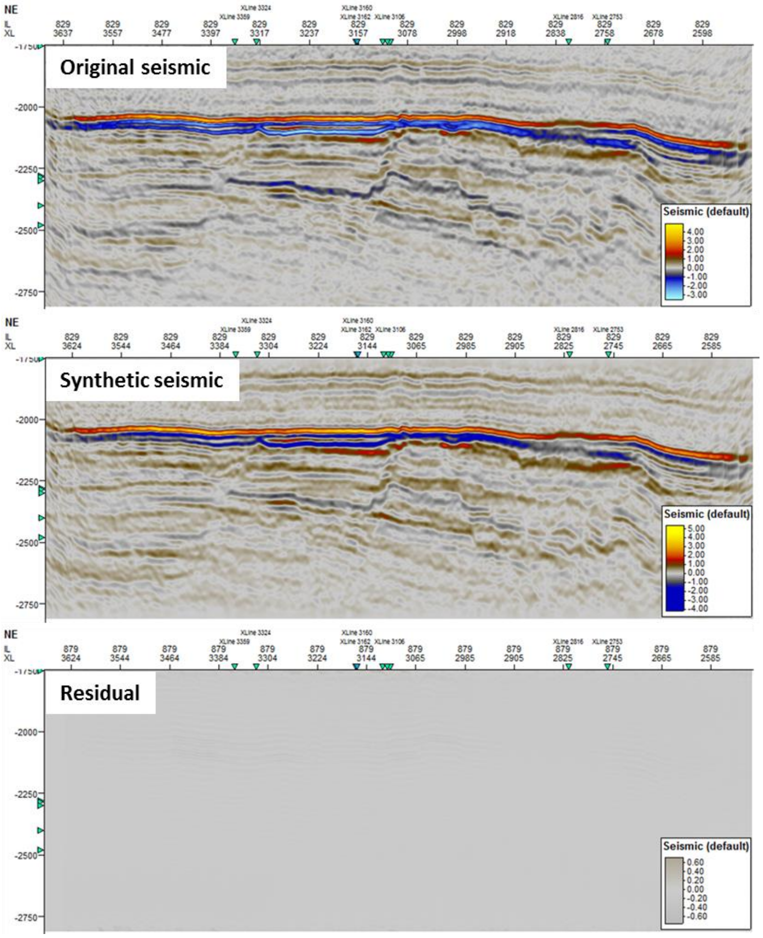

Figure 6.6: Section of the original seismic(top), synthetic seismic from the deterministic inversion using 13J Isis frequency wavelet (middle), and their difference or residual section (bottom).

The other method to assess the quality of the inversion is to compare the modeled acoustic impedance with the acoustic impedance log at the well location. **Figure 6.7** shows this inversion QC using both wells 30_9-15 and 30_9-11. The sections show the modeled acoustic impedance using the 13J Isis Frequency (top) and the 5S Isis Frequency (bottom) wavelets. Although the wavelets were extracted from different wells, the modeled acoustic impedance sections are in agreement with both wells.

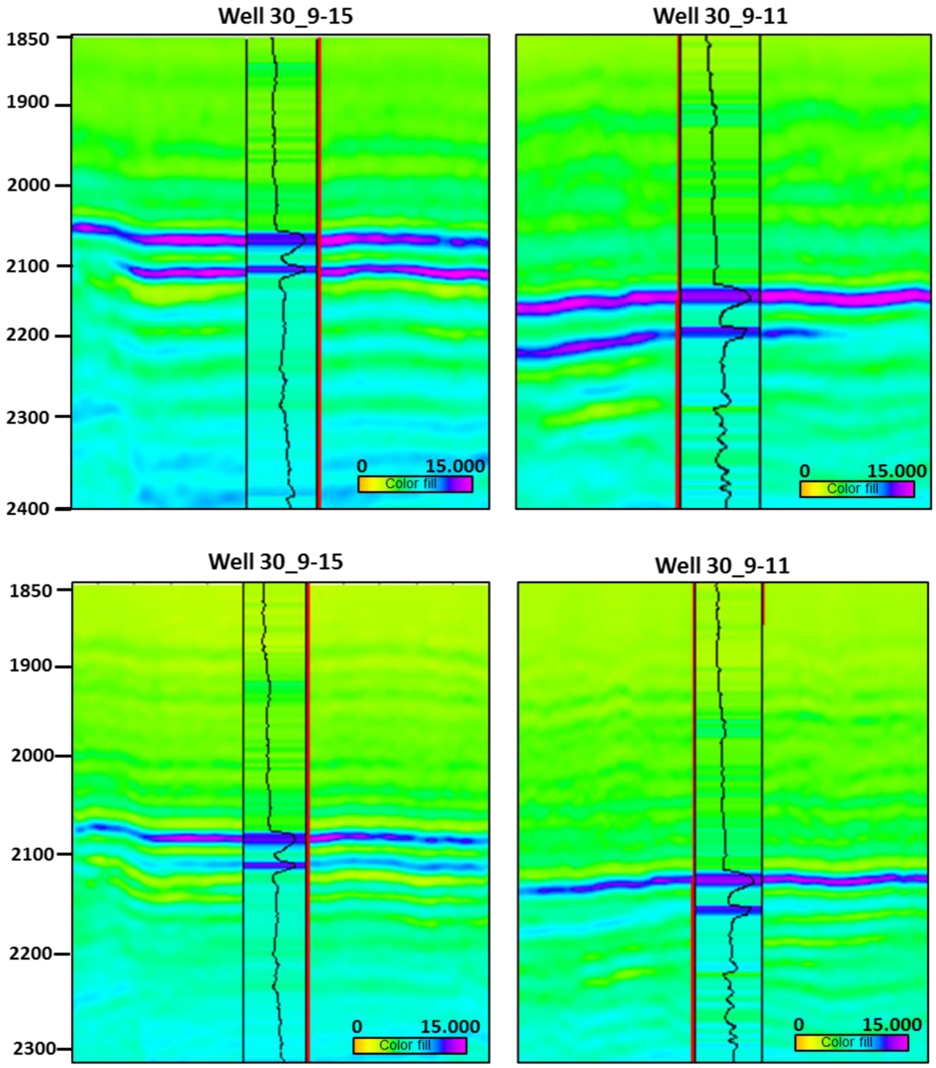

Figure 6.7: Deterministic inversion QC for well 30_9-15 (left) and well 30_9-11 (right). The viewport displays the acoustic impedance of the well log

6.2.4 Facies Modeling

The four acoustic impedance cubes from the different wavelets were copied into the 3D grid. Prior to facies modeling, the 3D grid was converted to depth using the velocity model (see section 5.5.1). **Figure 6.8** shows well 30/9-J-13 with the four deterministic inversion results together with the acoustic impedance log, the upscaled acoustic impedance log, and the facies log which is based on a cut-off of the acoustic impedance log (see section 5.5.1). Within the Shetland Gp., the deterministic inversion has no problems in capturing the thick, high acoustic impedance limestone layers. However, within the reservoir interval (Brent Gp.), the deterministic inversion cannot resolve the thin layers of limestone.

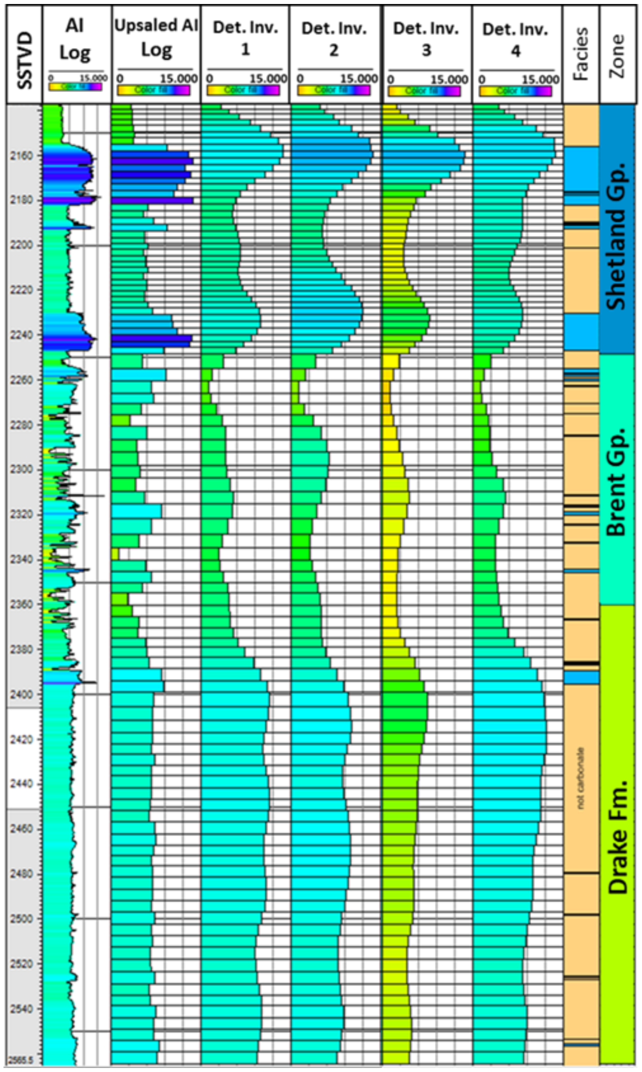

Figure 6.8 : Well section for well 30/9-J-13. From left to right: SSTVD axis, acoustic impedance log (AI), upscaled acoustic impedance log, deterministic inversion from wavelet 30J Isis Frequency wavelet (1), wavelet 5S Isis frequency (2), statistical wavelet (3), and 13 Extended White wavelet (4), and facies Log and zone division. See Figure 6.1 for well location.

As discussed in section 5.4.1, limestone has acoustic impedance values in the range of 9000-15000 kPa.s/m. **Figure 6.9** shows the look up tables used for guiding the facies for each zone of the model, based on the deterministic inversion coming from the 13J Isis Frequency wavelet.

Within the first zone which is represented by the thick carbonate layers the impedance values range from 5000-14000 kPa.s/m. The function assigns high limestone probabilities for the acoustic impedance above 9000 kPa.s/m but it also assigns lower probabilities for values bellow 9000 kPa.s/m, which is in conflict with the well data.

Within the reservoir interval characterized by thin layers of limestone, the deterministic inversion delivers acoustic impedance values bellow 8000 kPa.s/m. However, the look-up function assigns significant limestone probability for impedance values in the range of 7000-8000 kPa.s/m.

The Drake-Cook zone shows impedance values similar to the ones in the reservoir interval, but limestone probability is significantly lower.

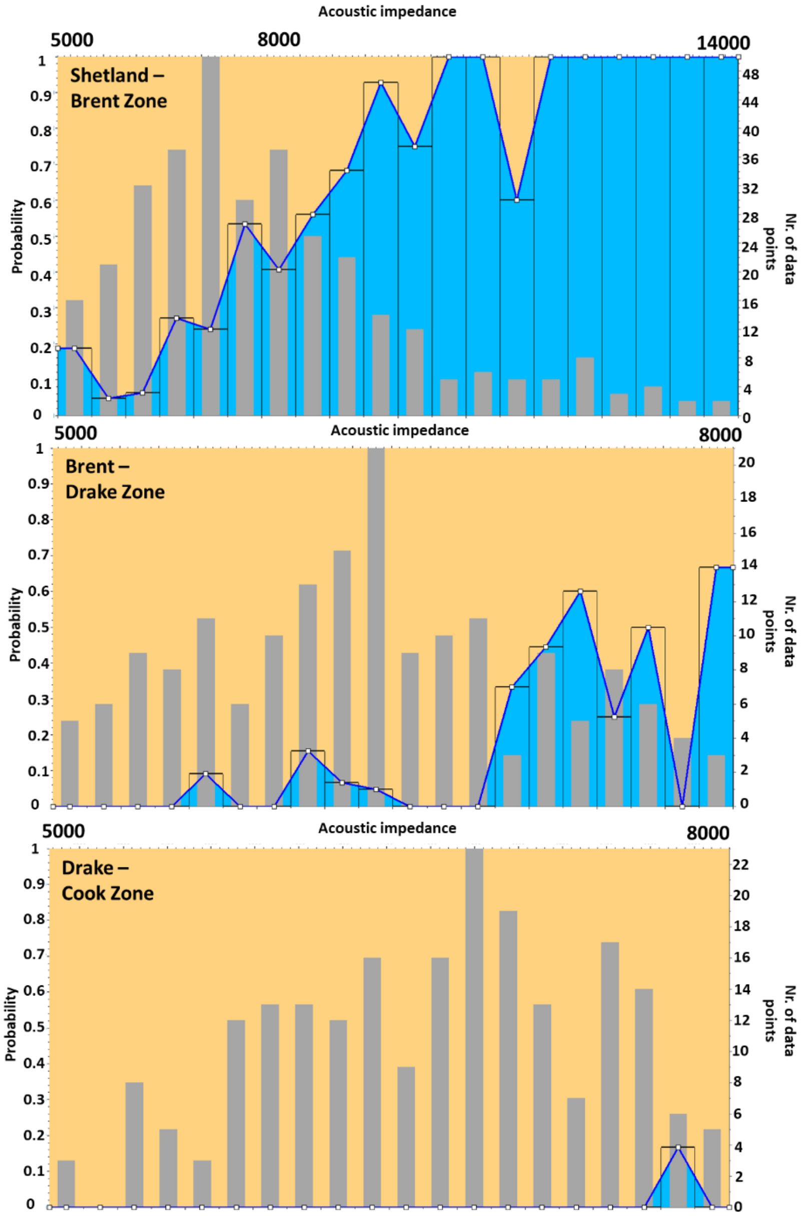

Figure 6.9 Look up function for each zone of the model from the deterministic inversion using the 13J Isis Frequency wavelet. The limestone probabilities assigned to different impedance values are shown by the blue bars. The grey bars represent the number of well data points available.

Based on the look-up function discussed above, a probability cube was calculated. Then an average probability map was derived for the reservoir interval (**Figure 6.10**). Within the horst structure where most of the wells are drilled, the limestone probability varies between 5 to 15% while outside the horst the probability is higher an it ranges from 25 to 72%.

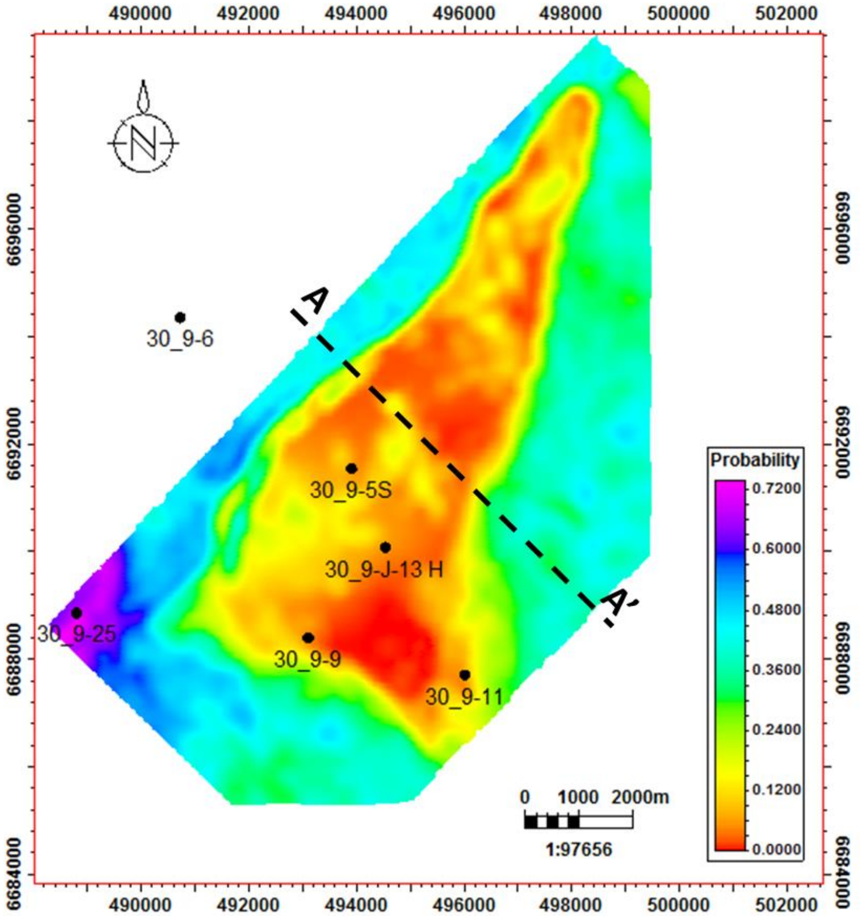

Figure 6.10: Average probability map for the reservoir interval. Within the horst structure the probability varies between 0-15% while on the flank of the structure, away from the wells, the probabily increases and it ranges from 25 to 72%.

The algorithm used for the facies modeling is SIS. The variogram parameters controlling the distribution of the facies were derived from the deterministic inversion results (see section 5.3.1) and they are listed in **Table 6.1**. By using the different seed numbers (see section 3.5), equiprobable (stochastic facies simulation) results were obtained. These results were used for the uncertainty of carbonate distribution.

	Major range	Minor range	Vertical range	Sill	Nugget effect
Shetland Gp.- Brent Gp.	3855.676	3210.795	14	1	0
Brent Gp. – Drake Fm.	3535.917	3489.148	14	1	0
Drake Fm. – Cook Fm.	4625.652	3949.61	17	1	0

Table 6.1: Variogram parameters used for the facies modeling. The horizontal variograms were derived from the deterministic inversion while the vertical ones were derived from well data.

Figure 6.11 displays the deterministic inversion, probability cube, and two facies models for a cross-section whose navigation is shown in **Figure 6.10**. The probability cube was made using the look-up function showed in **Figure 6.9.** The acoustic impedance cross-section (**Figure 6.11-1.**) shows the result from the deterministic inversion using the 13J Isis Frequency wavelet. Although the acoustic impedance values within the reservoir are vary between 5000-8000 kPa.s/m, well below the 9000 kPa.s/m cut-off used for the facies log, the probability cube (**Figure 6.11-2.**) indicates limestone probabilities between 20-60% within the reservoir interval on the flank of the horst structure. Within the horst structure, the probability ranges between 0-10%, in agreement with the average probability map shown in **Figure 6.10. Figure 6.11-3** and **6.11-4** show two facies models made using SIS with different seed numbers and guided by the probability cube. It can be observed that both facies models are honor the probability cube, assigning mainly limestone where the limestone probability is high (above 80%). However, there are differences between the models where the probability is relatively low. For instance, at the flanks of the horst where the probabilities range between 20 and 60 % the facies distribution of the two models are different.

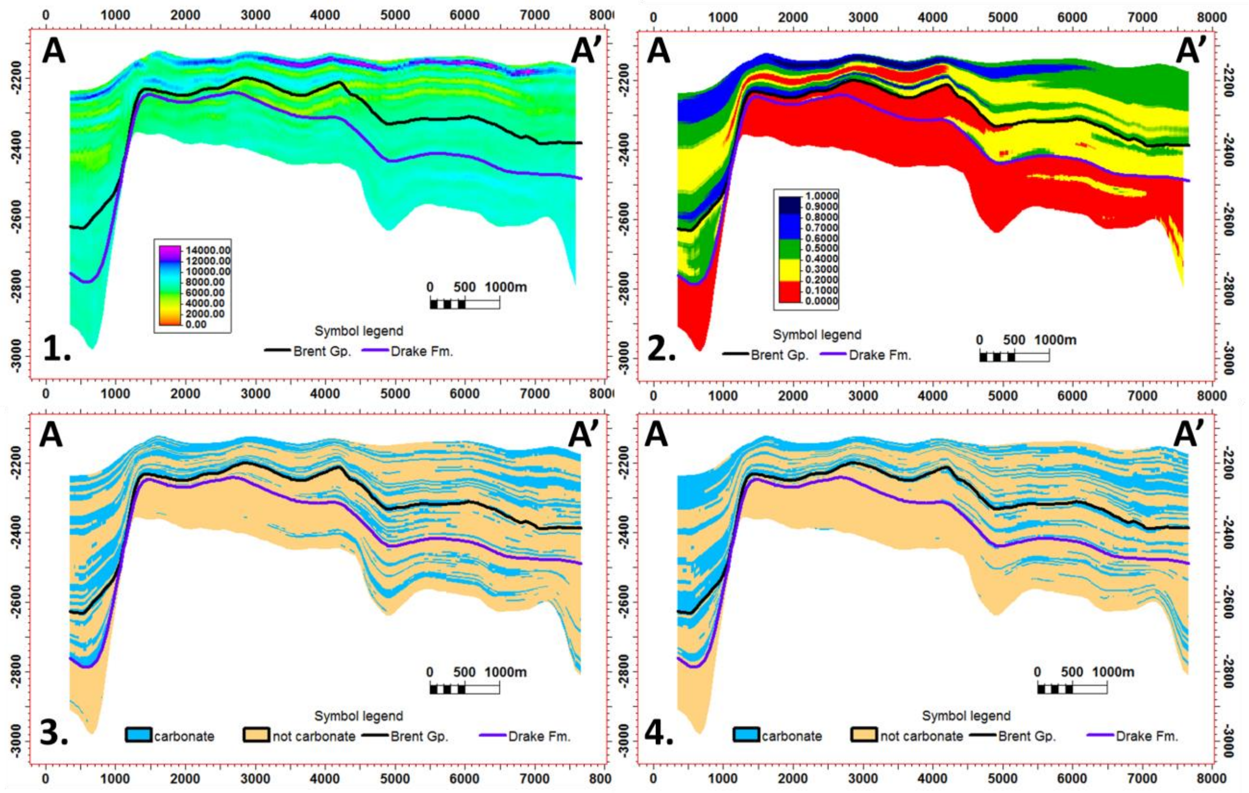

Figure 6.11: 1. Cross-section through the acoustic impedance cube from the deterministic inversion using the 13J Isis Frequency wavelet. 2.: Cross-section through the probability cube generated using the look-up function. 3. and 4.: Cross-section of two facies simulations. Top (Brent Gp.) and base (Drake Fm.) of the reservoir are shown in each cross-section as black and purple lines, respectively. The location of the cross-section is shown in Figure 6.10.

Figure 6.12 shows the limestone thickness map for the reservoir interval. Within the horst structure the thickness varies between 0 to 10 m which is in accordance with the probability cube that assigns low limestone probabilities to this area. Towards the flanks of the horst, the thickness increases significantly, and it ranges from 40 to 300 m.

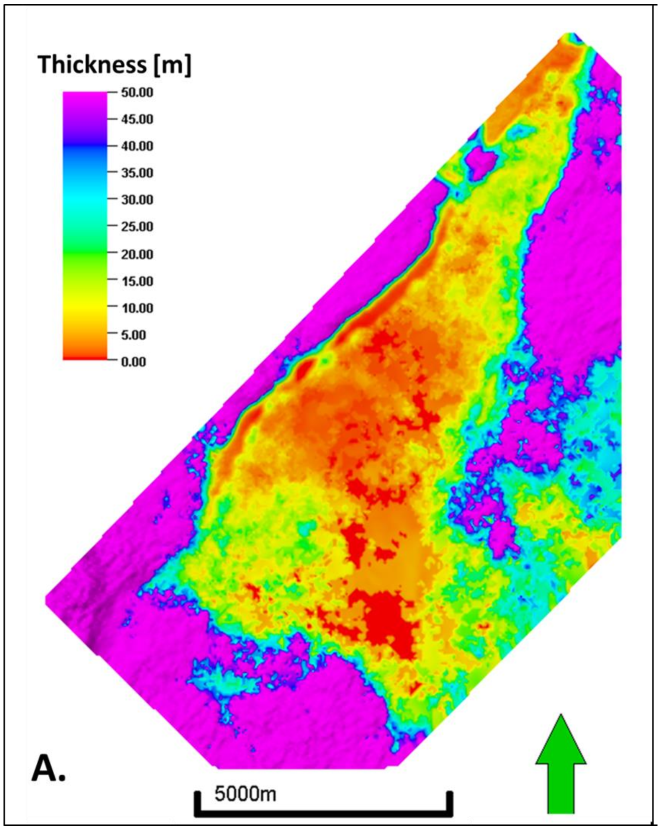

Figure 6.12 Limestone thickness map for the reservoir interval (Brent Gp. – Drake Fm.) from one facies model based on the deterministic inversion unsing the wavelet 13J Isis Frequency.

6.2.5 Volume and uncertainty calculation

200 facies simulations were calculated using SIS and the gross volume of the limestone was calculated for each model. Then the P10, P50 and P90 volumes were identified.

Figure 6.13 shows the limestone volume distribution from the 200 facies models alongside the wavelet used for deterministic inversion. The volume distribution is similar for all the wavelets ranging from 3.18E+9 m^3(P10) to 3.5E+9 m^3 (P90).

The P10 and P90 do not change when changing from 200 simulation to 100 simulations. However, the extreme values change. This test shows the reliability of the volume distribution: additional simulations would not significantly change the volume distribution.

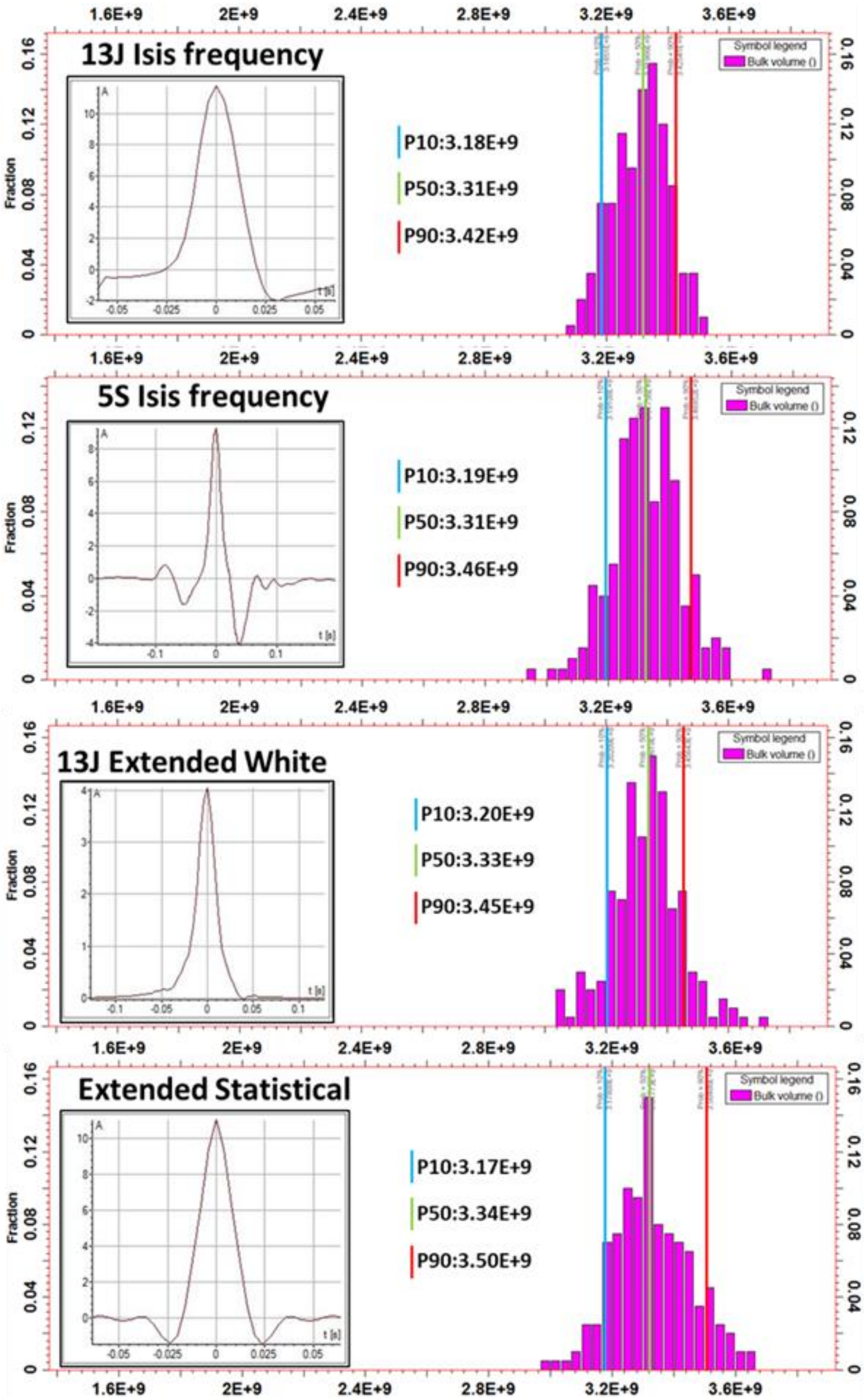

Figure 6.13 Histogram of the limestone volume within the reservoir interval based on 200 facies realisations based on the deterministic inversion using the 4 wavelets.

6.3 Stochastic inversion

6.3.1 Inversion

A total of 100 stochastic seismic inversion realizations were generated for each of the wavelets used for the deterministic inversion. **Figure 6.14** shows the results coming from three realizations and the average of 100 simulations with the 13J Isis Frequency wavelet. The results coming from the other wavelets are similar. The top of the reservoir (Brent Gp.) is marked with a red line while the base of the reservoir (Drake Fm.) is marked with a purple line.

Figure 6.14-A shows a zoom in section of the reservoir interval. Above the reservoir, within the horst structure, the Shetland Gp. is represented by high acoustic impedance values mainly above 9000 kPa.s/m indicating the presence of the tight limestone which is sealing the reservoir. However, on the flanks of the horst, lower acoustic impedance values between 2000-3000 kPa.s/m are present. Within the reservoir interval the acoustic impedance mainly ranges between 3000-7000 kPa.s/m but there are some thin layers represented by acoustic impedance values higher than 9000 kPa.s/m. Below the reservoir interval, the acoustic impedance values are lower than 9000 kPa.s/m indicating the presence of siliciclastic sediments.

Figure 6.14-B and **C** show different stochastic simulations made with the same wavelet. The results show a significant variation of the impedance values between the two realizations which leads to different facies distributions. One of the differences can be seen in **Figure 6.14-C** where within the reservoir interval on the flanks of the horst impedance values above 12000 kPa.s/m can be observed. On the other hand, in **Figure 6.14-B,** at the same location, the impedance varies between 7000 to 9000 kPa.s/m. Although these simulations are different, they are also equiprobable because they honor the seismic data thus showcasing the non-unique character of the seismic inversion.

Figure 6.14-D displays the average of the 100 stochastic simulations based on the 13J Isis Frequency wavelet. The results show a smoothed acoustic impedance model with less vertical and horizontal variability, thus resembling the results obtained from the deterministic inversion.

Because the stochastic inversion integrates the acoustic impedance log in the results a blind well test was conducted for well 30/9-J-13 in the following way: the acoustic impedance log and the low frequency model were recalculated without taking well 30/9-J-13 into account.

The result is given by **Figure 6.15** which shows four individual simulation alongside the AI log, upscaled AI log and the LFM in this well. It can be observed that all individual simulations differ from each other and none of them matches the acoustic impedance log of the well.

Within the first zone all stochastic simulations can approximately identify the two thick layers of carbonate. The simulations show some vertical variability assigning lower acoustic impedance values in a zone characterized by higher values. This vertical variability can also be seen in the impedance sections of **Figure 6.14-A**.

The blind-well test shows clearly that within the reservoir interval the stochastic inversion cannot honor the acoustic impedance log and fails in resolving the thin layers of carbonate. Instead it randomly assigns high values of acoustic impedance values thus resulting in the differences between **Figure 6.14-B** and **Figure 6.14-C.**

Figure 6.16 shows the AI log alongside the deterministic inversion and the mean of the 100 stochastic simulations made using the 13J Isis Frequency wavelet. It can be observed that although the individual simulations of **Figure 6.15** show large differences between each other, the mean of the 100 simulation have no problem in capturing the thick limestone layers. Furthermore, the mean of multiple stochastic simulations is very similar to the results from the deterministic inversion, which is in agreement with the observation made in **Figure 6.14-D.**

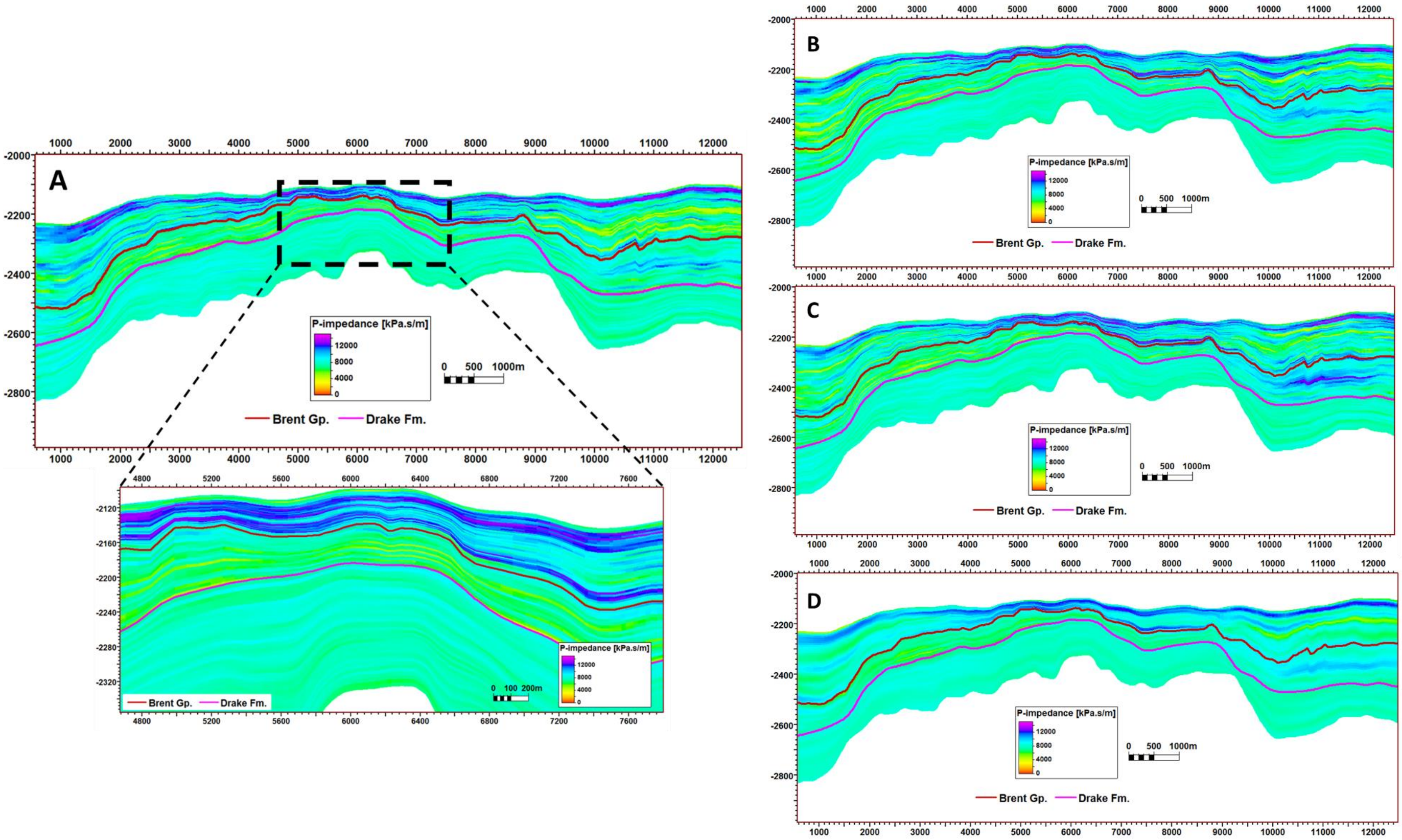

Figure 6.14: Acoustic impedance coming from stochastic inversion using the 13J Isis Frequency wavelet and different seeds (A,B,C). D represents the average of 100 stochastic inversion simulations. Top and base of the reservoir (Brent Gp. and Drake Fm.) are illustrated with red and purple lines, respectively.

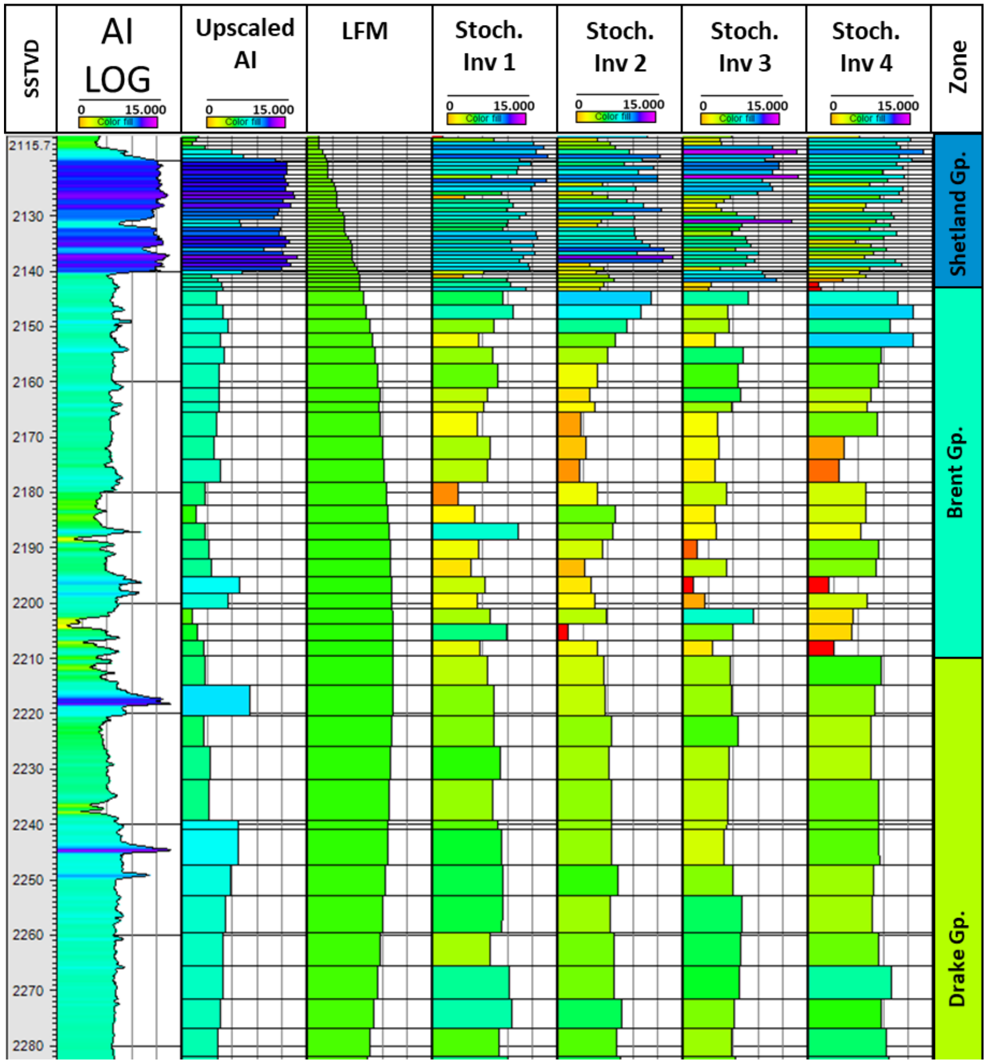

Figure 6.15 Well section for well 30/9-J-13 showing the results of a blind-well test.. From left to right: SSTVD axis, acoustic impedance log (AI), upscaled acoustic impedance log, LFM, stochastic inversion using the 13J Isis frequency wavelet and different seeds (Stoch. Inv 1,2,3 and 4) and zone division. See Figure 6.1 for well location.

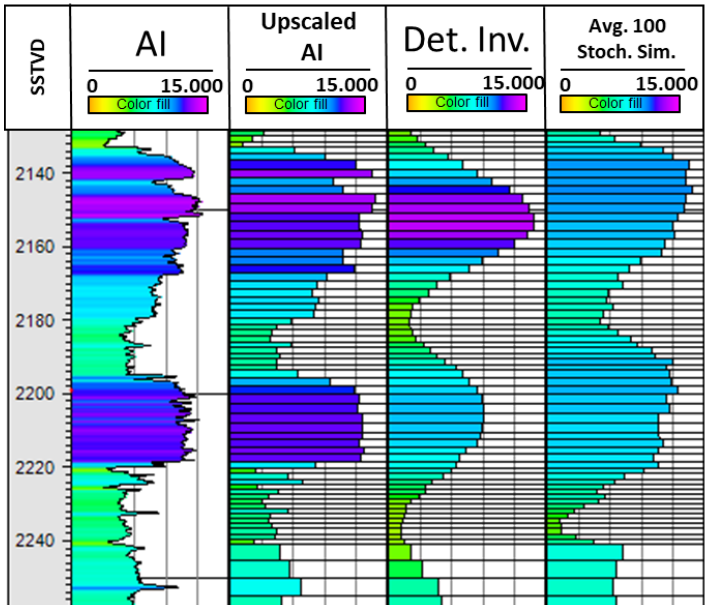

Figure 6.16 Well section for well 30/9-J-13. From left to right: SSTVD axis, acoustic impedance log (AI), upscaled acoustic impedance log, deterministic inversion from wavelet 30J Isis Frequency wavelet (Det. Inv.) and the average of 100 stochastic inversion simulations. See Figure 6.1 for well location.

6.3.2 **Inversion Q**C

The diagnostic output (see section 5.3.3.) of the stochastic inversion was analyzed for each simulation. **Figure 6.17** shows the cost function, number of iterations and the convergence (Boolean) map coming from one simulation based on the 13J Isis Frequency wavelet. The inversion results are overall successful but showing problems along the faults zones where the number of iterations is higher, or the cost function did not converge during the iteration procedure. This is mainly due to the low signal to noise ratio within the fault zones.

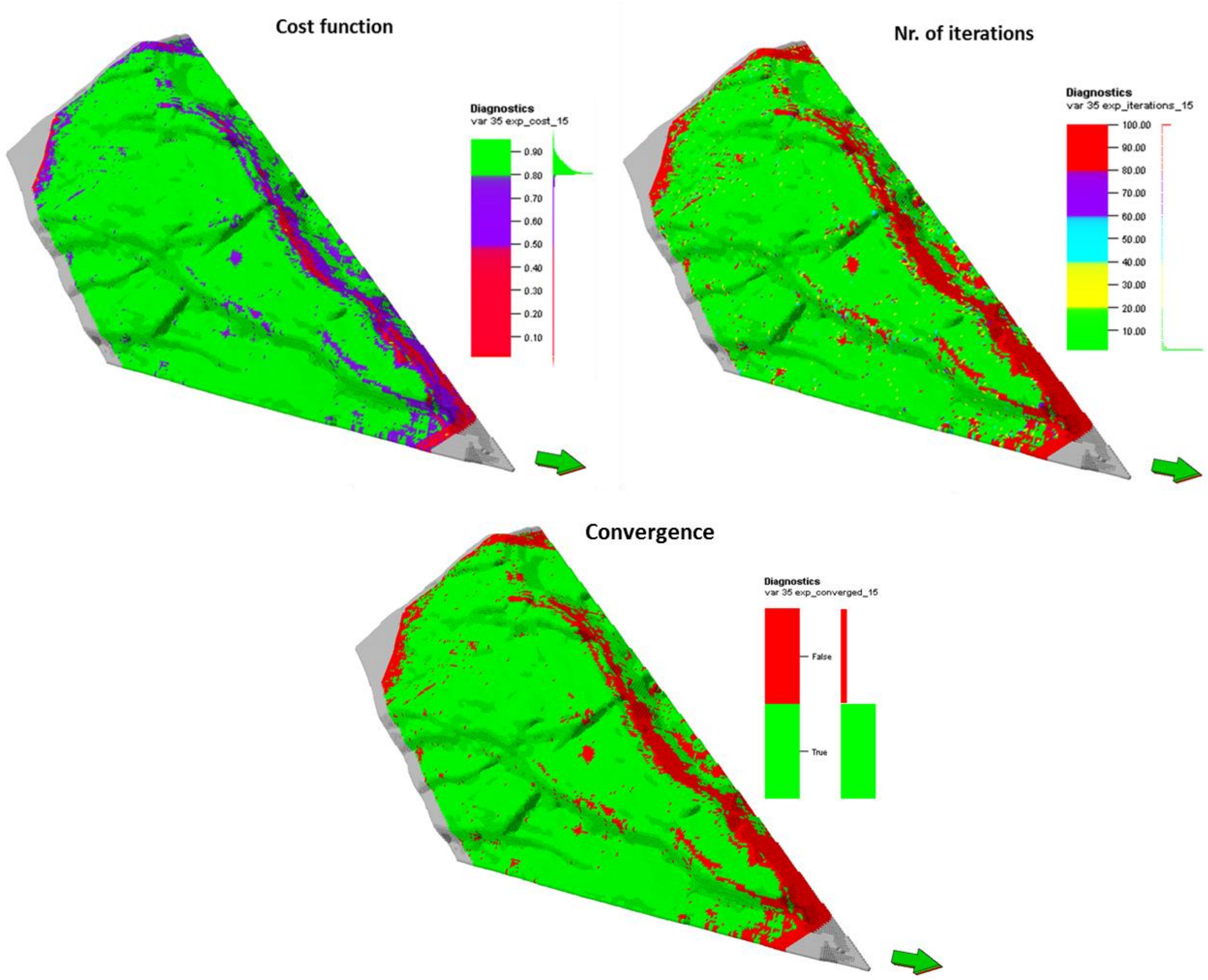

Figure 6.17 Diagnostic outup of the stochastic inversion made using the 13J isis frequency wavelet showing: costfunction(top left), number of iteration(top right) and the convergence (bottom). Note how the stohastic inversion has problems along the fault zones.

A synthetic seismic was generated for the same simulation in order to compare the results coming from the stochastic inversion with the original seismic (**Figure 6.18**). The synthetic shows a good correlation with the seismic, although fault zones in the synthetic are smoothed out. The largest differences are exhibited by the amplitude (**Figure 6.19**). These differences can be partly explained by the grid cell size used in the model. Due to time constraints a grid of 50x50 m was used for the model although the trace spacing of the seismic cube is 12.5x12.5 m.

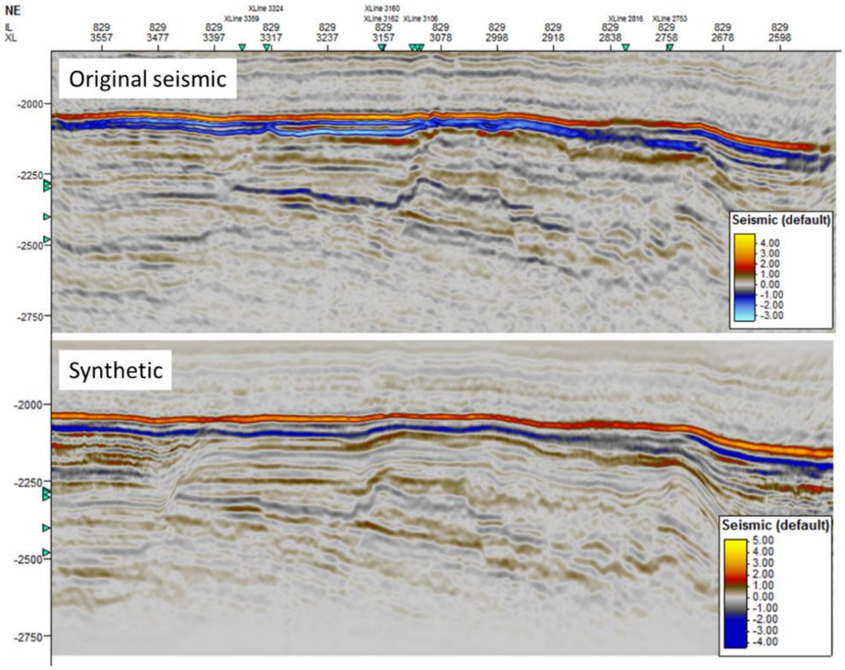

Figure 6.18 Section of the original seismic(top) and synthetic seismic(bottom) coming from one stochastic inversion simulation using 13J Isis Frequency wavelet.

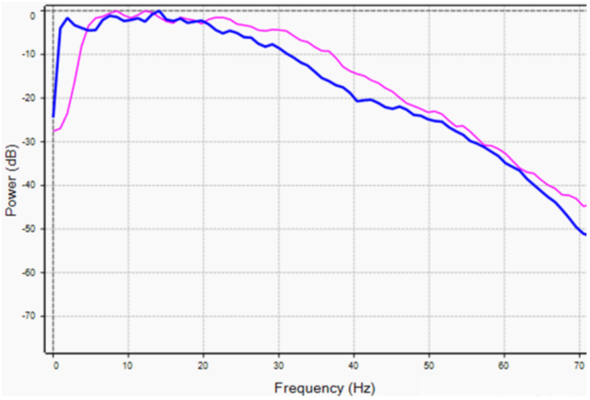

Figure 6.19: Amplitude spectrum comparing the seismic (pink line) and the synthetic seismogram for one stochastic simulation using the 13J Isis Frequency wavelet

6.3.3 Facies modeling

Based on the 100 acoustic impedance realizations a limestone probability cube was built using the same impedance (9000 kPa.s/m) cut-off of the acoustic impedance log (see section 5.4.1). This probability cube was used as an input for stochastic indicator simulation. **Figure 6.20** shows the average limestone probability for the reservoir interval. The map shows more variability than the one obtained from deterministic inversion (**Figure 6.10**) with overall lower probabilities away from the wells and at the flanks.

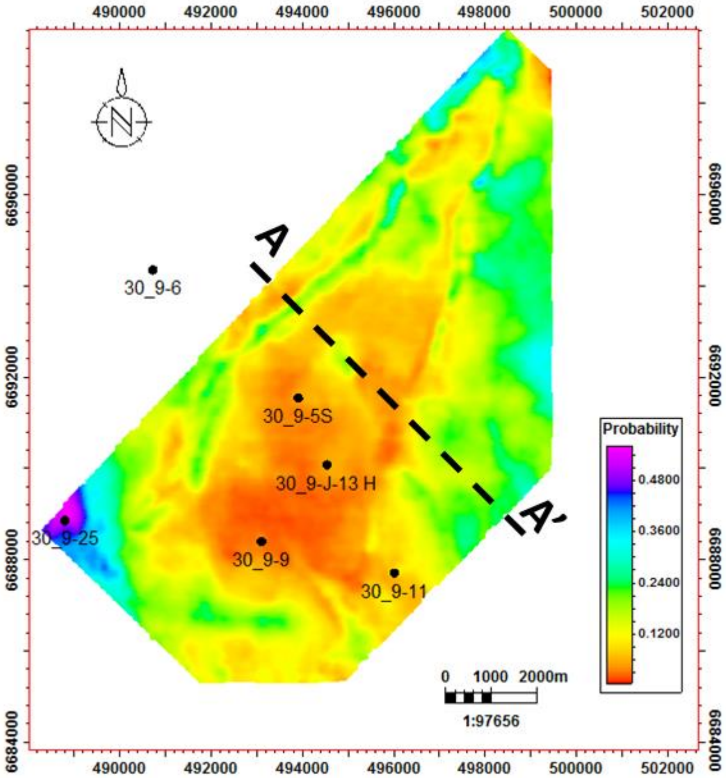

Figure 6.20 Average probability map for the reservoir interval. Overall the limestone probability is low between 0 to 25% within the reservoir interval.

Figure 6.21 shows one stochastic inversion, the probability cube and two facies models for a cross-section with the navigation shown in **Figure 6.20**. The acoustic impedance cross-section (**Figure 6.21-1.**) shows the result from the stochastic inversion using the 13J Isis Frequency wavelet. This cross-section shows high acoustic impedance values above 9000 kPa.s/m only in the Shetland Gp. zone resulting in high limestone probabilities between 60-100%. Within the reservoir interval, the acoustic impedance mainly varies between 5000-8000 kPa.s/m. with only one thin layer of acoustic impedance above 9000 kPa.s/m contributing to the 20-50% limestone probabilities shown in **Figure 6.21-2**. **Figure 6.21-3** and **6.21-4** show two facies models made by SIS with different seed numbers and guided by the probability cube. The high limestone probabilities of the Shetland Gp. produced thick and laterally continuous limestone layers in both facies models. Within the reservoir interval, the limestone layers are thin and poorly connected due to the low probabilities assigned.

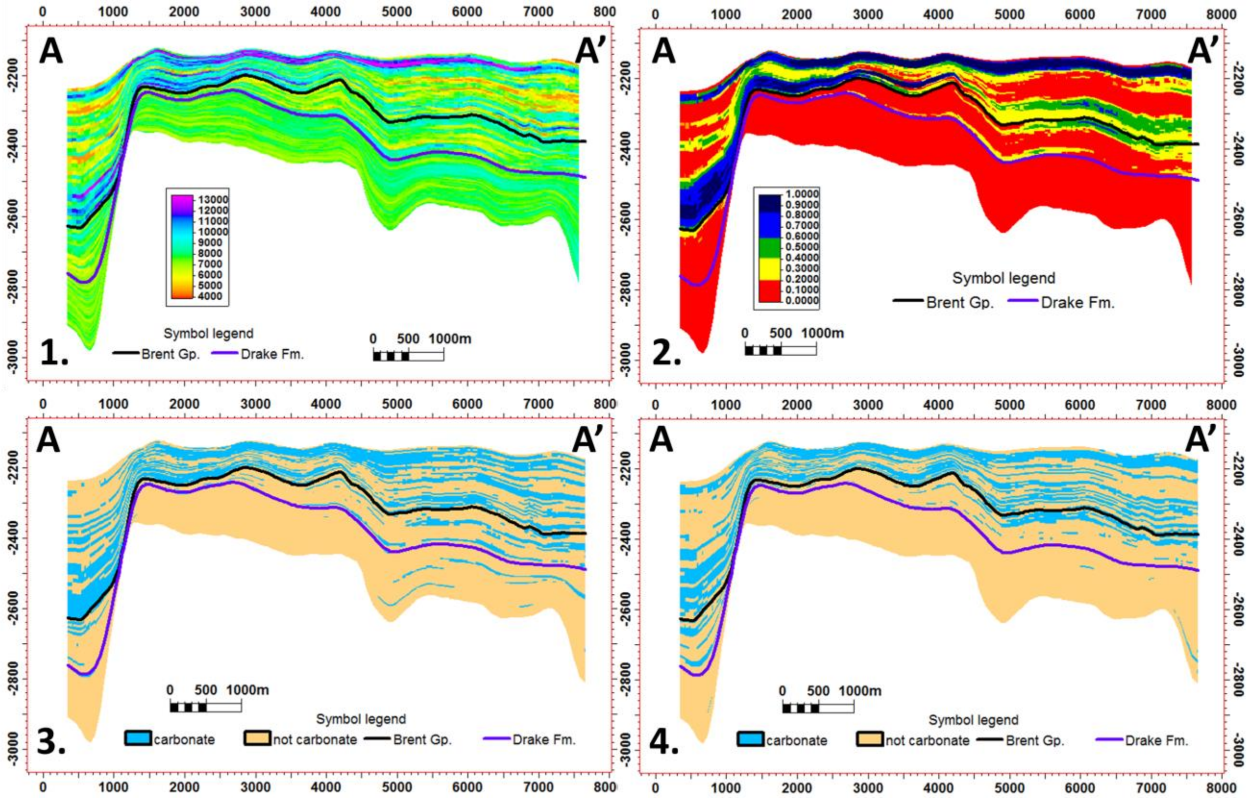

Figure 6.21: Cross-section through the acoustic impedance cube coming from the stochastic inversion using the 13J Isis Frequency wavelet. 2.: Cross-section through the probability cube generated based on the 100 stochastic simulations. 3. and 4.: Cross-section thorough two facies models using different seeds. Top (Brent Gp.) and base (Drake Fm.) of the reservoir are shown in each cross-section by black and purple lines, respectively. The location of the cross-section is shown in Figure 6.19.

Figure 6.22 shows the limestone thickness map for the reservoir interval derived from one facies model based on stochastic inversions using the 13J Isis frequency wavelet. Overall within the whole study area the limestone thickness is low varying from 0 to 30 m. However, there are still locations towards the edges of the study area where the thickness is ranges from 45 to 250 m. The thickness map corresponds to the average probability map shown in **Figure 6.20** with low thicknesses matching low probabilities and higher thicknesses corresponding to probabilities ranging between 25-50 %.

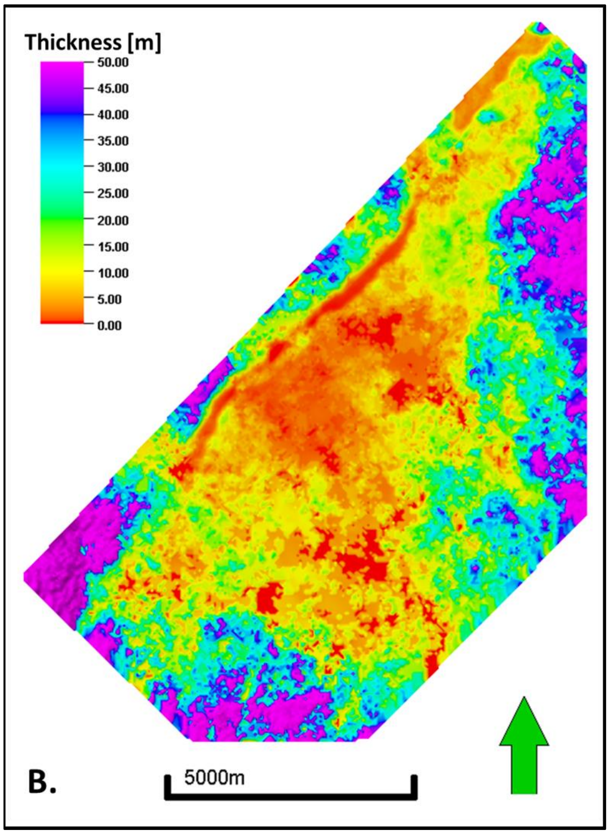

Figure 6.22 Limestone thickness map for the reservoir interval (Brent Gp. – Drake Fm.) coming from one facies model based on the stochastic inversion unsing the wavelet 13J Isis Frequency.

6.3.4 Volume and uncertainty calculation

After depth converting the stochastic simulations using the velocity cube, 200 facies simulations were calculated using SIS and different seeds.

Figure 6.23 shows the limestone volume distribution for the reservoir interval from the 200 facies models, for each wavelet used in the stochastic inversion process. There are large differences between these volumes and the ones coming from deterministic inversion (**Figure 6.13**). Stochastic inversion delivers almost half of the volumes delivered by deterministic inversion with values ranging from 1.68E+9 m^3 for the P10 to 2.02E+9 m^3 for the P90.

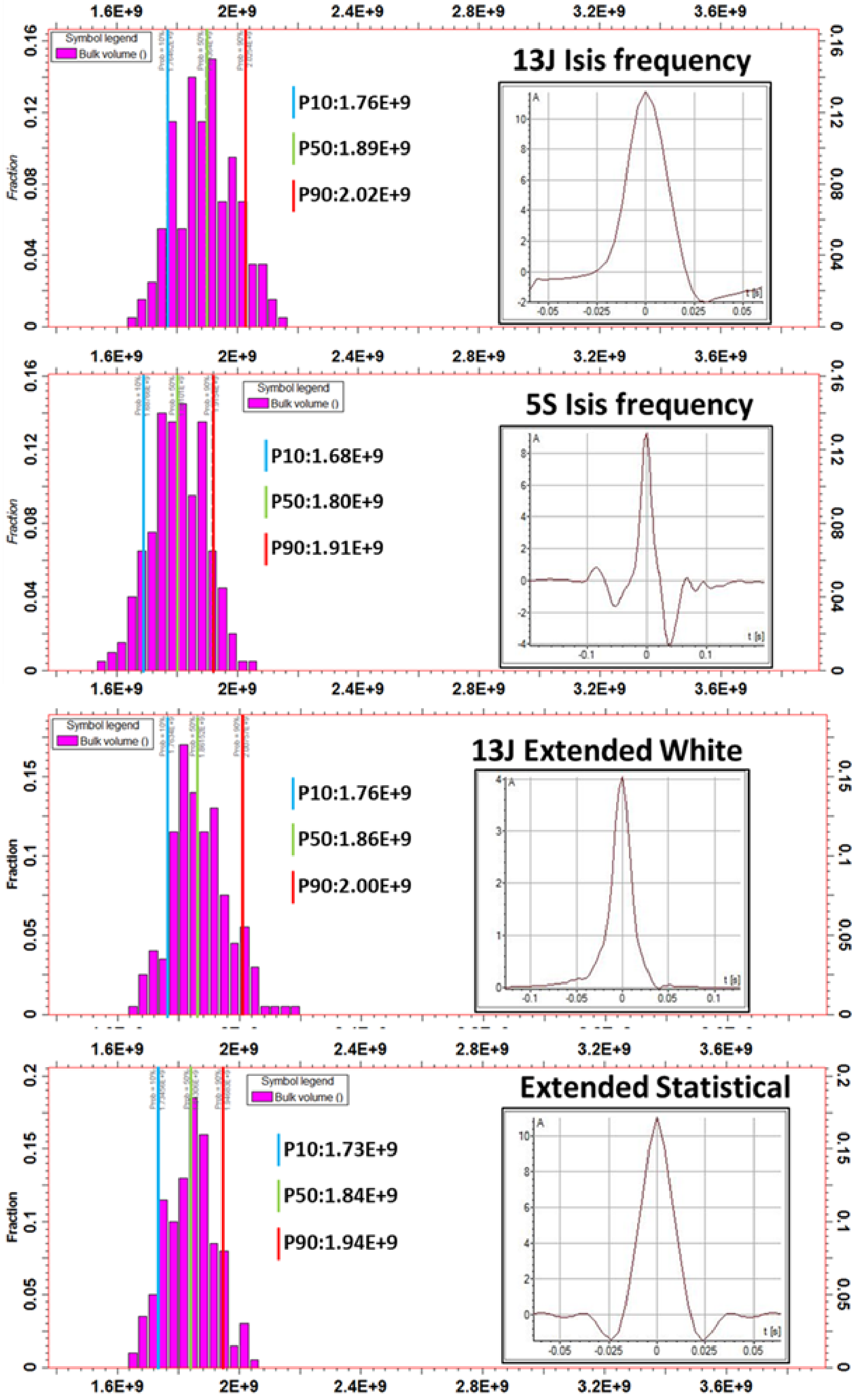

Figure 6.23: Histogram of the limestone volume of the reservoir interval based on 200 facies realisations and on probability cubes derived from stochastic inversion using the 4 wavelets.

6.4 Facies simulation based on well data only

The last modelling method consists of facies modeling using just the well data with no seismic guidance. Using SIS and the same variogram parameters used for the other two methods 200 facies models were built and the volume of limestone was calculated for each of them.

Figure 6.24 shows two facies models based solely on well data and different simulation runs. The top and base of the reservoir (Brent Gp. and Drake Fm.) are shown with red and pink lines. Within the Shetland Gp., the limestone layers are thick and continuous throughout the model in both cases. Some variability is shown in the reservoir interval where the upper facies model displays a thick and continuous carbonate layer, while the lower facies model presents a thin, more disconnected limestone layer.

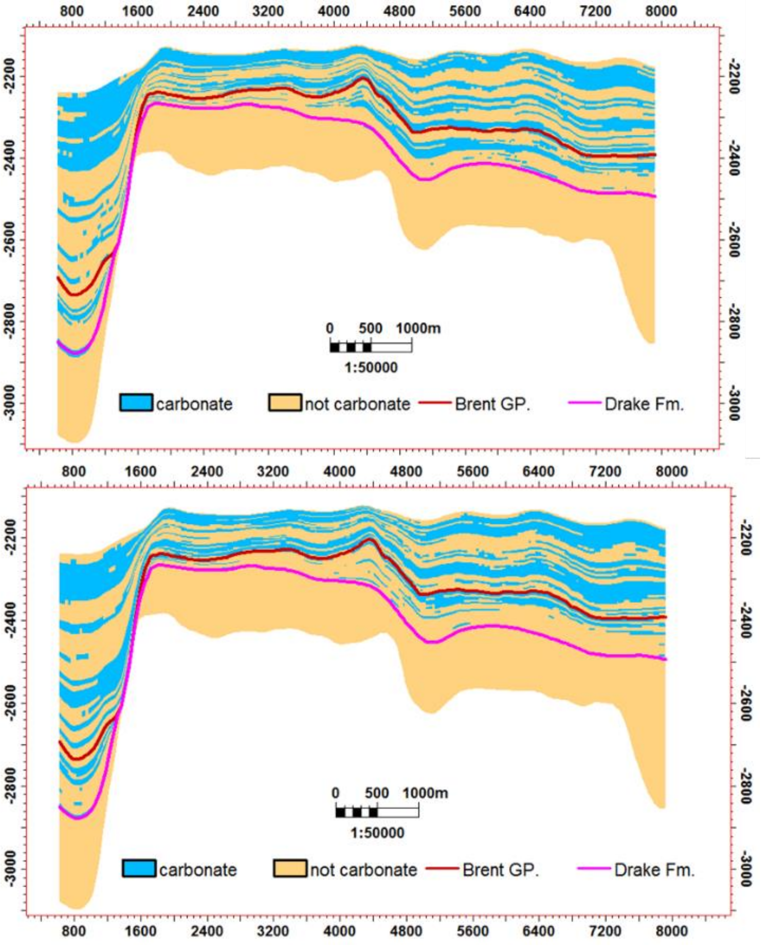

Figure 6.24: Two facies models based only on well data.

Figure 6.25 shows the limestone thickness map for the reservoir interval. Overall within the horst structure, the limestone thickness varies from 0-25m. On the flanks of the horst, the thickness map shows more variability with thicknesses ranging from 10-30 m in the south-eastern part and patches of very thick limestone deposits ranging for 50 to 300 m.

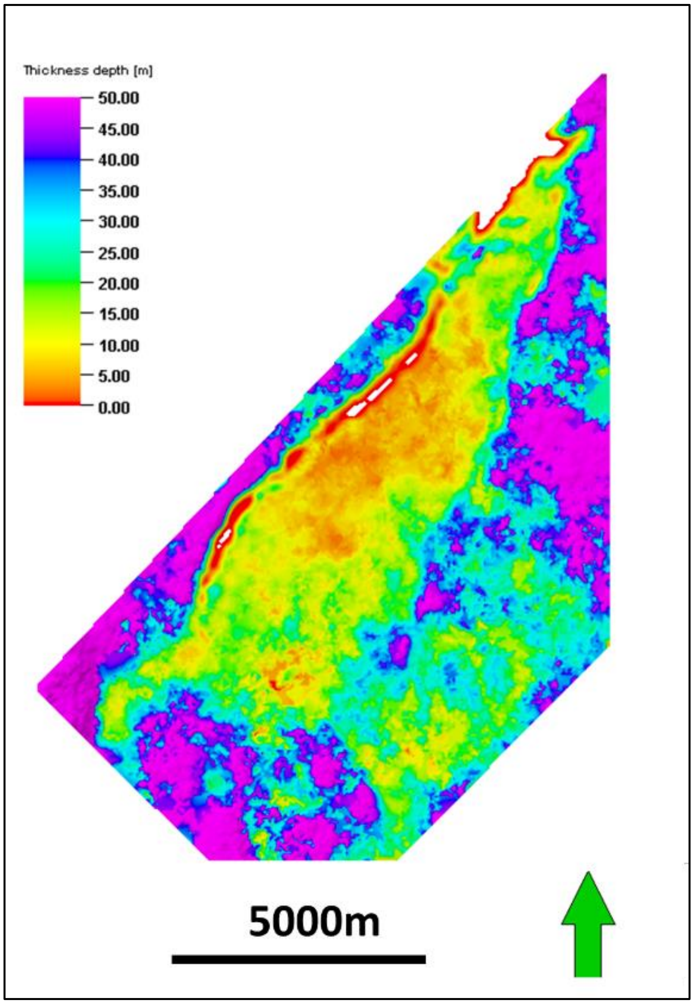

Figure 6.25: Limestone thickness map for the reservoir interval (Brent Gp. – Drake Fm.) from one facies model based only on well data.

Figure 6.26 shows the limestone volume distribution for the reservoir interval from the 200 facies models based on well data. The volumes lie between the ones from stochastic and deterministic inversion with values ranging from 2.8E+9 m^3 for the P10 to 3.12E+9 m^3 for the P90.

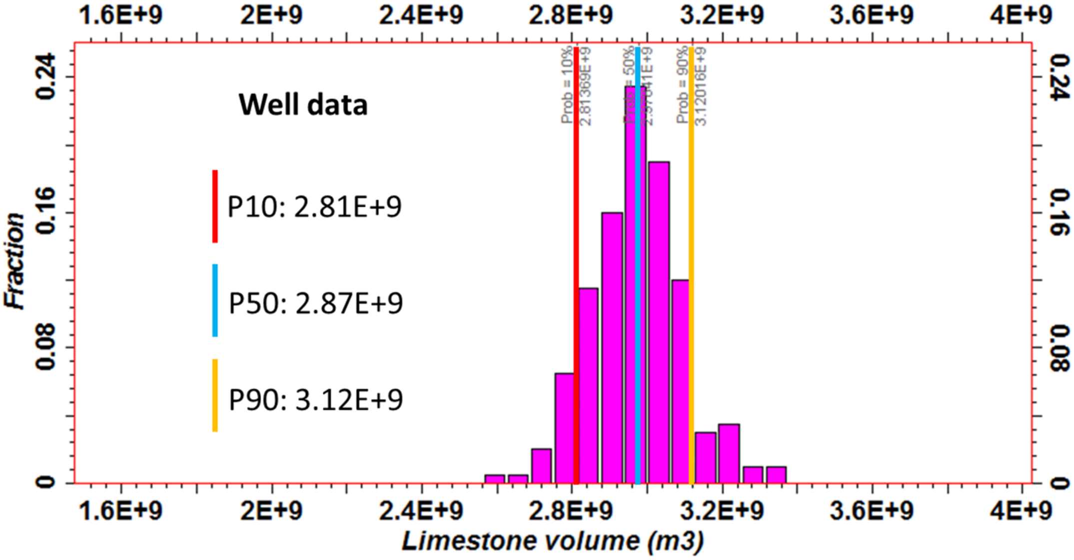

Figure 6.26: Histogram of the limestone volume within the reservoir interval derived from 200 facies realisations based only on well data.

7 Discussion

In this chapter the results of the different methods used for modeling are compared and further discussed together with published studies based on different datasets. The aim is to showcase the advantages and disadvantages of each method and try to determine which one is more useful.

Although the seismic inversion cannot differentiate between sand and shale it is still useful to identify the limestone. This is important because the limestone is tight and has very low porosities, and it can act as baffle zones within the reservoir thus affecting reservoir connectivity. Knowing the distribution of the limestone can provide more realistic volumes and can lead to better decision making when placing future wells.

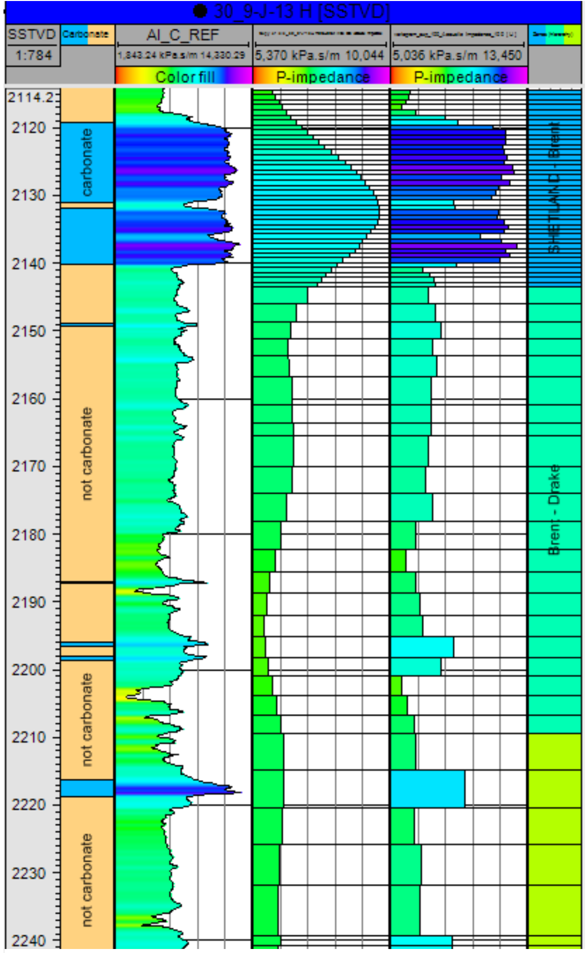

Figure 7.1 Well section for well 30/9-J-13. From left to right: SSTVD axis, facies log, acoustic impedance log (AI), deterministic and stochastic inversion using 13J ISIS frequency wavelet and zone division. See Figure 6.1 for well location.

Figure 7.1 shows a comparison between deterministic and stochastic inversion coming from the 13J ISIS frequency wavelet. As mentioned in section 6.2.4 deterministic inversion is able to detect the thick layers of carbonate but it incorrectly assigns low acoustic impedance values ranging between 2000-4000 kPa.s/m to the thin layers of carbonate. On the other hand, stochastic inversion is able to capture both the thin and thick layers of carbonate at least at the well location as shown in **Figure 7.1**. Note that as discussed in section 6.3.1 stochastic inversion has difficulties in identifying the thin layers of limestone when performing a blind well test. This highlights again the influence of the seismic bandlimits on the stochastic results.

Figure 7.2 shows an acoustic impedance section from the deterministic inversion (top) and the stochastic inversion (bottom) performed using the 13 Isis Frequency wavelet. The impedance values were color coded such as the values below 9000 kPa.s/m are represented by the grey color. It is obvious that deterministic inversion shows higher impedance values, above the cut-off used for the facies log mainly in the upper zone represented by the Shetland Gp.-Brent Gp. In turn, stochastic inversion exhibits greater variability and distribution of the high impedance values. This is also supported by **Figure 6.9** which shows the look up function used to build the probability cube for the deterministic inversion. However, the look-up table shows high limestone probabilities for impedance values below 9000 kPa.s/m which is obviously wrong. This is due to the fact that deterministic inversion has a too low resolution to detect any limestone within the reservoir as shown in **Figure 7.1**. Therefore, the look-up function assigns limestone facies to low (wrong) impedance values and then uses these values to build the CDF.

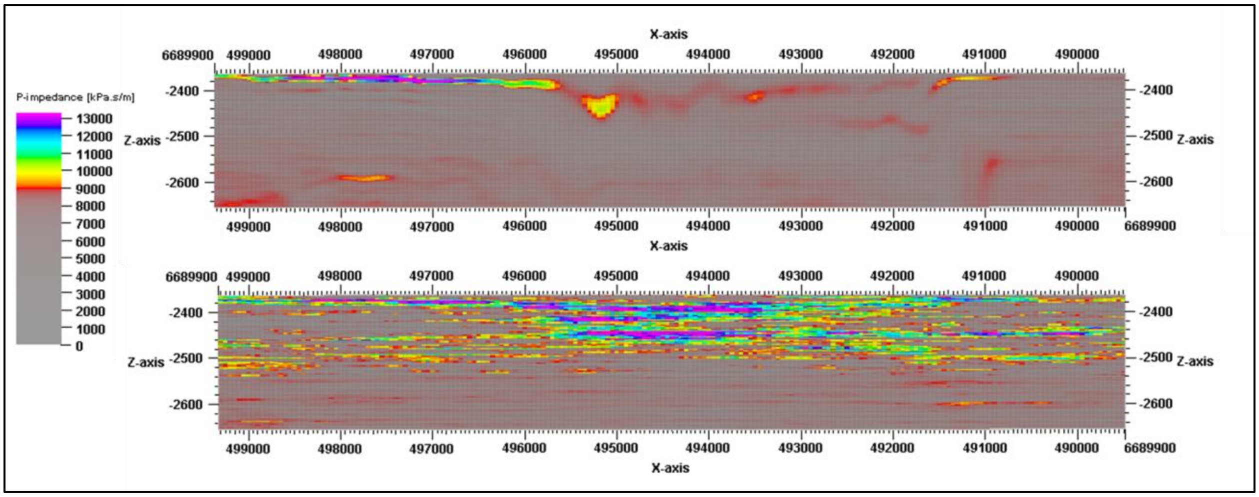

Figure 7.2: Acoustic impedance section coming from deterministic inversion (top) and stochastic inversion (bottom). The impedance values are color coded as grey bellow the 9000 kPa. s/m cut-off used for the facies log. Section location is shown in Figure 6.20.

As a consequence, the probability map derived from the deterministic inversion (**Figure 6.10**) shows significant higher probabilities than the one derived from stochastic inversion (**Figure 6.19**), mainly due to the wrong assignment of limestone facies to impedance values. Because the facies models are guided by the probability cubes, this leads to thicker limestone deposits in the deterministic inversion (**Figure 6.12)** which shows a larger distribution of limestones between 45-300 m thick with a mean value of 36m and a standard deviation of 44m. On the other hand, the thickness map derived from stochastic inversion (**Figure 6.21**) shows greater variability with overall lower thicknesses with a mean value of 21m and a standard deviation of 28 m.

This in turn explains the resulting higher volumes obtained using deterministic inversion. These volumes are 50% larger than the ones obtained from stochastic inversion (**Figure 7.3**). Furthermore, it is important to notice that the volume distributions coming from the four different wavelets for both deterministic (**Figure 6.13**) and stochastic (**Figure 6.22**) inversions deliver similar values for the P10, P50 and P90. This suggests that the inversion process is not as sensitive to the wavelet as previously thought and described by Sim and Bacon, (2014).

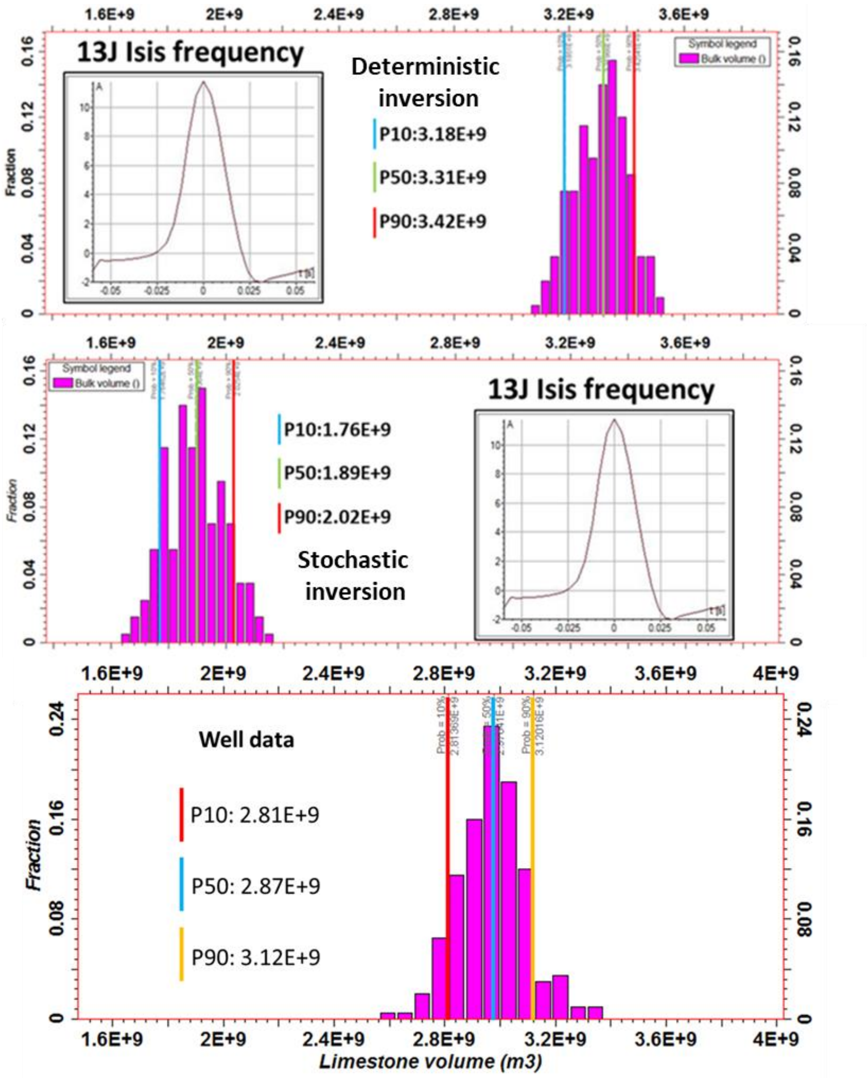

Figure 7.3: Histogram of the limestone volume within the reservoir interval based on 200 facies realisations based on deterministic inversion (top) , stochastic inversion (middle) and well data only (bottom).

The volumetrics from modeling based only on well data are positioned between the results from deterministic and stochastic inversion. Although these models are not constrained by the seismic, their results may be more reliable than those from deterministic inversion as deterministic inversion is misguiding the facies and overestimating the volumes.

One individual simulation from stochastic inversion does not honor the acoustic impedance log and has difficulties in resolving the thin layers of limestone. The mean of 100 stochastic simulations is the deterministic inversion as described in section 6.3.1. So, where is the benefit of using stochastic inversion? When we look at the acoustic impedance results from the deterministic inversion (**Figure 6.5**), we can observe that it delivers smooth results. This is due to the missing high frequencies which sets a limit to the resolution of deterministic inversion. In comparison the impedance results coming from stochastic inversion (**Figure 6.14**) show increased variability and the presence of thin layers. This has also been observed by Soares et. al (2007) and Francis (2006b). These thin layers are below seismic resolution and are introduced by the Gauss simulation of the acoustic impedance logs. Stochastic inversion checks whether the impedance distribution at the individual locations of the model is in conflict with the seismic. The seismic is band-limited and consequently cannot deliver limestone layers below a certain thickness. Therefore, deterministic inversion cannot resolve thin limestone layers indicated by the log data. Stochastic inversion on the other hand, offer several equivalent solutions showing different distributions of thin layers that are beyond seismic resolution. All models have in common that they honor the seismic data. Although stochastic inversion will not provide the perfect facies model it will accurately showcase the probability of encountering limestones. It allows assessing the uncertainty and offers a reliable volume distribution rather than a unique (possibly incorrect) answer (Bratvold and Begg, 2008).

8 Conclusion

Based on the theory, methods and results of this Master thesis, the following conclusions are highlighted:

- Because of the missing high frequencies in the seismic data deterministic inversion delivers a smooth average of the impedance which is unsuitable for addressing thin facies layers in reservoir modeling.
- Stochastic inversion is characterized by a higher vertical resolution and is therefore more favorable for modeling thin reservoirs.
- Stochastic simulation is based on several parameters (variogram ranges, impedance variance, wavelet etc.) that typically are not sufficiently controlled by field data because of the lack of wells. Consequently, they are subject to uncertainty which should be considered when capturing the uncertainty in the modelled facies distribution.
- Facies modeling based on deterministic inversion is superior to well-based stochastic modeling only in case of thick layers that lie within seismic resolution. Overall though, stochastic simulation is a more reasonable and powerful way to deal with the uncertainty in facies distributions.

9 Recommendation for future work

Based on the theory, methods and results of this Master thesis, the following recommendations are suggested:

- In order to get more accurate volumes stochastic AVO inversion should be performed. By using the Vp and Vs data one could be able to differentiate between sand and shale.

- A detailed fault interpretation and a 3D model with fault framework can provide a better understanding of the connectivity between the different compartments of the reservoir.

10 References

Adlakha, K., 2018, Fracture analysis and modelling of the South Arne field: Master Thesis, Petroleum Geosciences Engineering, Faculty of Science and Technology, University of Stavanger, p. 27.

Azevedo, L., Nunes, R., Soares, A., Neto, G. S., and Martins, T. S., 2018, Geostatistical seismic amplitude-versus-angle inversion. Geophysical Prospecting, v. 66, p. 116–131.

Badley, M., Price, J., Dahl, C. R., and Agdestein, T., 1988, The structural evolution of the northern Viking Graben and its bearing upon extensional modes of basin formation: Journal of the Geological Society, v. 145, no. 3, p. 455-472.

Badley, M. E., Egeberg, T., and Nipen, O., 1984, Development of rift basins illustrated by the structural evolution of the Oseberg feature, Block 30/6, offshore Norway: Journal of the Geological Society, v. 141, no. 4, p. 639-649.

Bortoli, L.J., Alabert, F., Haas, A. and Journel, A.G., 1992, Constraining Stochastic Images to Seismic Data, Geostatistics Troia, v. 1,p. 325-338.

Bratvold, R.B. and Begg, S.H. 2008. I would rather be vaguely right than precisely wrong: A new approach to decision making in the petroleum exploration and production industry. AAPG Bull. 92, 1373-1392.

Buland, A., and Omre, H., 2003, Bayesian linearized AVO inversion: Geophysics, v. 68, no. 1, p. 185-198.

Doyen, P.M., 2007, Seismic Reservoir Characterization: An Earth Modelling Perspective. EAGE. Houten, p. 255.

Dubrule, O., 2003, Geostatistics for seismic data integration in earth models, SEG/EAGE distinguished instructor short course no. 6.

Eynon, G., 1981, Basin development and sedimentation in the Middle Jurassic of the northern North Sea, In Illing, L. V. & Hobson, G. D. (eds) Petroleum Geology of the continental Shelf of North West Europe, Heyden, London, 196-204.

Færseth, R., 1996, Interaction of Permo-Triassic and Jurassic extensional fault-blocks during the development of the northern North Sea: Journal of the Geological Society, v. 153, no. 6, p. 931-944.

Færseth, R. B., and Ravnås, R., 1998, Evolution of the Oseberg fault-block in context of the northern north sea structural framework: Marine and Petroleum Geology, v. 15, no. 5, p. 467-490.

Francis, A., 2006a, Understanding stochastic inversion:part 1. First Break, v. 24(11), p. 69–77.

2006b, Understanding stochastic inversion: part 2. First Break, v. 24(12), p. 79–84.

Gabrielsen, R. H., Færseth, R. B., and Jensen, L. N., 1990, Structural Elements of the Norwegian Continental Shelf. Pt. 1. The Barents Sea Region, Norwegian Petroleum Directorate.

Giltner, J.P., 1987, Application of extensional models to the northern Viking Graben, Norsk Geologisk Tidsskriftm v. 67, p. 339-352.

Graue, E., Helland-Hansen, W., Johnsen, J., Lømo, L., Nøttvedt, A., Rønning, K., Steel, R., 1987. Advance and retreat of Brent delta system, Norwegian North Sea. Petroleum geology of north west Europe, p. 915-937.

Gunning, J. and Glinsky, M., 2003. Bayesian seismic inversion delivers integrated sub-surface models, EAGE.Annual Meeting Abstract.

Haas, A., Dubrule, O., 1994, Geostatistical inversion – a sequential method of stochastic reservoir modelling constrained by seismic data. First Break, v. 12, p. 561–569.

Hassan H. H., Khalid M., Wafaa M.H., 2015, Model-Based Inversion In North Sea. F3-Block Dutch Sector: Bachelor degree, Geophysics Department,Faculty of Science, Ain Shams University

Helland-Hansen, W., Ashton, M., Lømo, L., and Steel, R., 1992, Advance and retreat of the Brent delta: recent contributions to the depositional model: Geological Society, London, Special Publications, v. 61, no. 1, p. 109-127.

Hosken, J. W. J., 1988, Ricker wavelets in their various guises. First Break, v. 6(1), p. 24–33.

Jensen, J. L., Lake, L. W., Corbett, P. W. M. & Goggin, D. J. 2000. Statistics for Petroleum Engineers and Geoscientists. 2nd Edn. Elsevier.

Johnsen, J. R., Rutledal, H., & Nilsen, D. E. (1995). Jurassic reservoirs; field examples from the Oseberg and Troll fields: Horda Platform area. Norwegian Petroleum Society Special Publications,v. 4, p. 199-234.

Journel, A.G. and Gomez-Hernandez, J.J, 1989, Stochastic imaging of the Wilmington clastic sequence, SPE 19857.

Lars U.F., 2018, Quantitative seismic interpretation including converted waves: Oseberg South Field: Master Thesis, Petroleum Geosciences Engineering, Faculty of Science and Technology, University of Stavanger, p. 3.

Latimer, R. B., Davidson, R., & Riel, P.V., 2000, An interpreter's guide to understanding and working with seismic-derived acoustic impedance data. The Leading Edge, v. 19(3), p. 242-256. doi:10.1190/1.1438580

Livera, S. E., 1989, Facies associations and sand body geometries in the Ness Formation of the Brent Group, Brent field. Geological Society, London, Special Publication, v. 41, p 86-269.

Løseth, T. M., Ryseth, A. E., and Young, M., 2009, Sedimentology and sequence stratigraphy of the middle Jurassic Tarbert Formation, Oseberg South area (northern North Sea): Basin Research, v. 21, no. 5, p. 597-619.

Matheron, G, 1967, Éléments pour une théorie des milieux poreux, Masson and Cie, Paris.

Moyen, R. and Doyen P.M, 2009, Reservoir connectivity uncertainty from stochastic seismic inversion. SEG Technical Program Expanded Abstracts, v. 28, p. 2378-2382.

NPD, 2018a, Factpages: Oseberg Sør, The Norwegian Petroleum Directorate.

-, 2018b, Factmaps: Oseberg Sør, The Norwegian Petroleum Directorate.

Pedersen, J. H., Karlsen, D. A., Backer-Owe, K., Lie, J. E., and Brunstad, H., 2006, The geochemistry of two unusual oils from the Norwegian North Sea: implications for new source rock and play scenario. Petroleum Geoscience v. 12, p. 85-96.

Pendrel, J., and Van Riel, P., 2000, Effect of well control on constrained sparse spike seismic inversion: CSEG Recorder, v. 25, p. 18-26.

Petrel Quantitative Interpretation, 15th Edition. Schlumberger 2015. VitalBook file.

Petrel Property Modelling, 15th Edition. Schlumberger 2017. VitalBook file.

Ravnås, R., and Bondevik, K., 1997, Architecture and controls on Bathonian–Kimmeridgian shallow-marine synrift wedges of the Oseberg–Brage area, northern North Sea: Basin Research, v. 9, no. 3, p. 197-226.

Ravnås, R., Bondevik, K., Helland-Hansen, W., Lømo, L., Ryseth, A., and Steel, R., 1997, Sedimentation history as an indicator of rift initiation and development: the late Bajocian-

Bathonian evolution of the Oseberg-Brage area, northern North Sea: Norsk Geologisk Tidsskrift, v. 77, no. 4, p. 205-232.

Richards, P. C., 1992, Geology of the Brent Group. Geological Society Special Publication No. 61, p.15-26.

Ricker, N., 1940, The form and nature of seismic waves and the structure of seismograms. Geophysics, v. 5, p. 348–366.

Ringrose, P. and Bentley, M., 2015, Reservoir Model Design, How to build good reservoir models, Springer.

Robinson, G., 2001, Stochastic Seismic Inversion Applied to Reservoir Characterization: Recorder, v.26, no. 1.

Russell, B. H., 1988, Introduction to seismic inversion methods, Society of Exploration Geophysicists, Tulsa.

Sabeti, H., Moradzadeh, A., Ardejani, F., Soares, A., 2017. A new stochastic 3D seismic inversion using direct sequential simulation and co-simulation in a genetic algorithm framework. Journal of Mining and Environment, v. 8, no. 3, p. 321-335.

Sams, M., and Saussus, D., 2013 Practical implications of low frequency model selection on quantitative interpretation results, in Proceedings 2013 SEG Annual Meeting2013, Society of Exploration Geophysicists.

Simm, R. W. and White, R., 2002, Phase, polarity and the interpreter’s wavelet (tutorial). First Break, v. 20, p. 277–281.

Shiv N. D., Ming-Ren H., Pierre La Croix, Louay Al-Mana, and Gary R., 2000, Prediction of reservoir properties by integration of seismic stochastic inversion and coherency attributes in super Giant Ghawar field: SEG Technical Program Expanded Abstracts 2000: p. 1501-1505.

Soares, A., Diet, J.D. and Guerreiro, L., 2007. Stochastic Inversion with a Global Perturbation Method: Proc., Petroleum Geostatistics, EAGE, Cascais, Portugal.,p. 10-14.

Steel, R., 1993, Triassic–Jurassic megasequence stratigraphy in the Northern North Sea: rift to post-rift evolution: Geological Society, London, Petroleum Geology Conference series, v. 4, no. 1, p. 299-315.

Steel, R., and Ryseth, A., 1990, The Triassic—Early Jurassic succession in the northern North Sea: megasequence stratigraphy and intra-Triassic tectonics: Geological Society, London, Special Publications, v. 55, no. 1, p. 139-168.

Tarantola, A., 2005, Inverse problem theory: Elsevier Science Publ. Co., Inc.

Veeken, P., and Da Silva, 2004, Seismic inversion methods and some of their constraints: First break, v. 22, no. 6, p. 47-70.

White, R.E. 1980, Partial Coherence Matchin of Synthetic Seismograms with Seismic Traces, Geophysical Prospecting, v. 28, p. 333-358.

White, R. E. and Simm, R. W., 2003, Tutorial – good practice in well ties. First Break, v.21, p. 75–83.

Yielding, G., Badley, M. E., and Roberts, A. M., 1992, The structural evolution of the Brent Province: Geological Society, London, Special Publications, v. 61, no. 1, p. 27-43.